SCUOLA DOTTORALE DI INGEGNERIA SEZIONE DI INGEGNERIA DELL'ELETTRONICA BIOMEDICA, DELL'ELETTROMAGNETISMO E DELLE TELECOMUNICAZIONI

XXIII CICLO

Progetto di Metamateriali per Applicazioni alle Telecomunicazioni

Luca Scorrano

A.A. 2010/2011

Docente Guida: Prof. Lucio Vegni

Tutor: Prof. Filiberto Bilotti

Coordinatore: Prof. Lucio Vegni

To my family and my dearest friends

INDEX

SOMMARIO

Nel presente lavoro sono descritti i risultati ottenuti nel corso del triennio della scuola dottorale relativamente al progetto di Metamateriali per applicazioni alle telecomunicazioni. Vengono inizialmente approfondite le tematiche relative alla caratterizzazione di tali mezzi complessi e le problematiche relative al progetto di strutture fisicamente realizzabili su di essi basate. Poiché un Metamateriale non è altro che un mezzo realizzato tramite inclusioni dielettriche o metalliche inserite in un mezzo ospite, quando si passa da una rappresentazione in termini di uno strato ideale lineare isotropo ed omogeneo al suo modello reale devono essere tenute in seria considerazione le caratteristiche elettriche dei mezzi conduttori e dielettrici coinvolti nel progetto, l'anisotropia delle inclusioni, la possibilità di poter omogeneizzare la struttura per poterne fornire una descrizione in termini di parametri macroscopici e l'effettiva capacità della struttura reale di supportare fenomeni di interfaccia, caratteristica invece strettamente legata al comportamento microscopico del Metamateriale. Questi ultimi due aspetti sono in realtà quelli che presentano le maggiori criticità essendo generalmente tali inclusioni più piccole della lunghezza d'onda di interesse ma non molto più piccole (tipicamente nell'ordine di un decimo della lunghezza d'onda). Viene poi fornito un equivalente a linee di trasmissione per uno strato lineare isotropo ed omogeneo di un Metamateriale al fine di poter definire, in termini di valori limite della permeabilità magnetica e della permittività elettrica, le caratteristiche di un mezzo ideale che possa emulare il comportamento una parete magnetica perfetta. Se ne suggeriscono due possibili implementazioni alle microonde, tramite l'uso di Split-Ring Resonators (SRR), ed alle frequenze ottiche tramite multistrati metallo-dielettrici realizzati tramite un'alternanza di argento e silice. Sono poi approfondite le problematiche relative al fenomeno della trasmissione straordinaria e vengono proposte una serie di metodologie basate sull'eccitazione di risonanze magnetiche localizzate al fine di incrementare la potenza trasmessa da una apertura elettricamente piccola. Vengono proposti degli approcci alle microonde basati sull'impiego di SRR e di inclusioni Omega, ed alle frequenze ottiche, basati invece sull'uso di nano-particelle realizzate con metalli nobili. L'utilizzo di strutture diverse nei due casi, in termini di

geometrie e materiali, è dettata dalla saturazione della risposta elettromagnetica delle inclusioni metalliche tipicamente usate alle microonde. In particolare, un aspetto significativo dei dispositivi presentati, avente come fine quello di aumentarne gli ambiti applicativi, è l'elevata miniaturizzazione di questi stessi. Viene poi suggerita, alle frequenze ottiche, la possibilità di sintetizzare in campo vicino una distribuzione di campo arbitraria, avente dettagli più piccoli della lunghezza d'onda, come diretta applicazione della teoria dei nano-circuiti ottici, mediante celle dielettriche che realizzano opportuni valori campionati di impedenza superficiale di un apposito schermo focalizzatore. Sono poi esplorate le possibili alternative, in alcuni ambiti applicativi, all'uso di Metamateriali, e vengono individuate a tal fine le superfici selettive in frequenza come validi candidati. Viene suggerita, a titolo di esempio, una possibile applicazione dell'uso di tali superfici al fenomeno della trasmissione straordinaria. I limiti e le effettive potenzialità dei Metamateriali sono infine analizzate.

1. INTRODUCTION

The evolution of technology and the scientific progress have been relying all long on two complementary processes, apparently at odds with each other, but proving that intrinsic strong connection existing between pure and applied research.

On a hand, we recognize the usage of consolidate concepts in unusual fields of application, the rediscovery from a completely new perspective, we would say, of ancient or lost concepts buried long time in the graveyard of inventions that have already proven their utility.

On the other hand, we look, not infrequently with suspicion, at the proposal of completely new theories and intuitions undermining the current understanding of the world around us, although hard to be verified experimentally due to intrinsic technological limitations.

The dualism of the aforementioned processes is, in a way, the same dualism that is found, for instance, in the contrast between quantum theory and determinism, dualism that is solved by the universal necessity of the whole mankind to give actual answers to both intellectual and practical needs.

From this perspective, the theory of metamaterials is exposed in the present work and many electromagnetic devices are presented both as straight applications of the aforementioned concept and as application of the metamaterial-point-of view to the needs and the requirements that such devices try to cope with.

1.1 BRIEF STORY OF METAMATERIALS

Victor Veselago, in a paper dated 1968 [1], was one of the first, at the author's best knowledge, to study the interaction between electromagnetic waves and media characterized by negative values of both the electric permittivity ε and the magnetic permeability μ. One of the main consequences that was found is that the wave-vector **k**, representing the phase velocity of a wave, turned out to be anti-parallel to the Poynting vector **S,** representing instead the power-flow associated to the wave. This was the reason why Veselago called such media "left-handed"; nowadays an interpretation based on the concept of negative index of refraction is preferred. This fact can be immediately derived from Maxwell's equations, written in the case of a monochromatic plane wave for a homogenous isotropic medium, where each term results proportional to $e^{-j(\mathbf{k}\mathbf{r}-\omega t)}$:

$$\begin{cases} \nabla\times\mathbf{E} = -j\omega\mu\,\mathbf{H} \\ \nabla\times\mathbf{H} = j\omega\varepsilon\,\mathbf{E} \end{cases} \Rightarrow \begin{cases} \mathbf{k}\times\mathbf{E} = j\omega\mu\,\mathbf{H} \\ -\mathbf{k}\times\mathbf{H} = j\omega\varepsilon\,\mathbf{E} \end{cases} \qquad (1.1)$$

From (1.1) if ε>0 and μ>0 (a Double PoSitive media or DPS), the electric field **E** and the magnetic field **H** are right-handed, otherwise, if ε<0 and μ<0 (a Double NeGative media or DNG), they form a left-handed triplet.

The other relevant feature of DNG media, as it was previously mentioned, is to show a negative index of refraction. From Maxwell's equations it is straightforwardly derived:

$$\begin{cases} \nabla^2\mathbf{E}(z,t) = \varepsilon\mu\dfrac{\partial^2\mathbf{E}(z,t)}{\partial t^2} \\ \nabla^2\mathbf{H}(z,t) = \varepsilon\mu\dfrac{\partial^2\mathbf{H}(z,t)}{\partial t^2} \end{cases} \qquad (1.2)$$

Each of (1.2) can be decomposed in three scalar equations admitting solutions $\propto \exp[-j(nkd-\omega t)]$. The complex quantities ε and μ appear in the wave equation as product. Apparently it seems it does not exist any difference between DNG and DPS media. Solutions for (1.2) are propagating waves both in case of ε>0 and μ>0 and ε<0 and μ<0. In order to resolve the ambiguity introduced by de definition of index of refraction $n=\sqrt{\varepsilon\mu}$ if ε<0 and μ<0 the notation ε=|ε|exp(iπ) and μ=|μ|exp(iπ) can be introduced.

Moreover, to ensure the passivity, the imaginary part of the square root $\sqrt{\varepsilon\mu}$ must be negative. Veselago postulated that radiation coming from a point source on one side of a DNG slab could be focused on the other side, suggesting this way the possibility to achieve flat lenses.

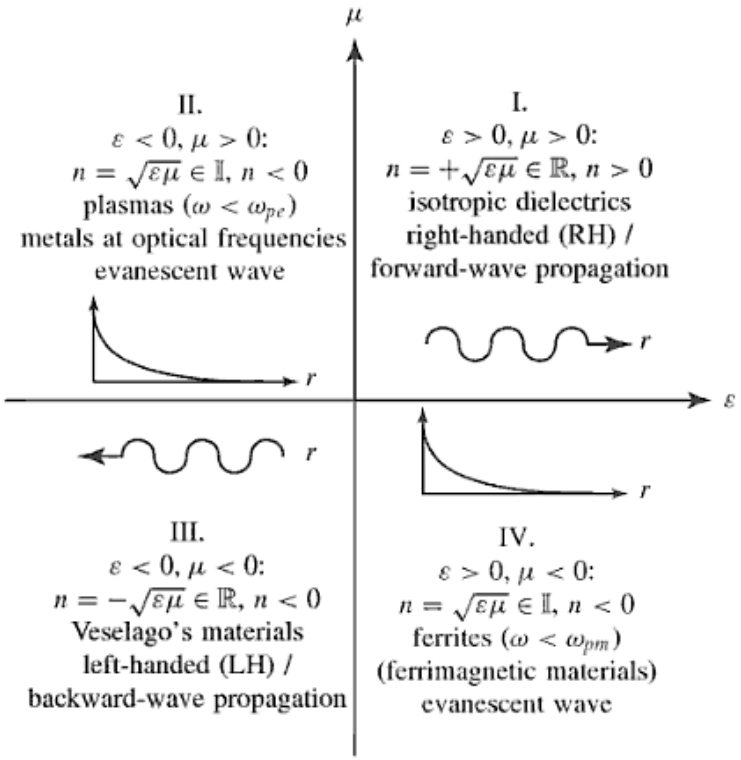

Figure 1 Veselago's materials classification. He was not able to find a natural or artificial structure exhibiting $\varepsilon<0$ and $\mu<0$ at the same time, but he suggested the use of plasmas and ferrites as single-negative metamaterial replacements in proper frequency ranges. (Pictures from ref. 1)

Media exhibiting $\varepsilon<0$ or $\mu<0$ are not easily found in nature, consequently there was no way out of Veselago intuition until 1990s. In 1996, 1998 and 1999 J. B. Pendry published a series of papers were structures exhibiting negative values of electric permittivity and of magnetic permeability were shown [2,3,4]. Such materials were obtained through periodic structures with both base elements and spacing smaller than the working wavelength: from a heuristic point of view, the wave "sees" such a composite medium as an homogeneous medium. This initial process of launching the subject of Metamaterials was then completed

with the seminal papers of Smith [5], Shelby [6] and Pendry [7]. The first demonstrated experimentally that an electromagnetic wave cannot propagate in medium in which only ε or μ is negative (i.e. a Single NeGative medium, SNG) but propagation is restored when they are both, the second verified a negative index of refraction designing a DNG prism at 10.5 GHz, the latter provided the first practical application, postulating not the possibility of beating the classic diffraction limit but the possibility of perfect imaging, that means the possibility of reproducing both the travelling waves and all the evanescent waves associated with the object. The initial stage of this process could then be considered as completed.

In accordance with the commonly used definition, *metamaterials are artificial materials made of dielectric or metallic inclusion embedded in a host medium, whose spacing and size are smaller than the working wavelength, exhibiting properties which are not commonly available in nature. The electromagnetic behavior of these engineered materials relies both on chemical and structural properties of their composition, using properly designed inhomogeneities to synthesize a required macroscopic behavior.*

2. BASIS OF METAMATERIAL THEORY

In this chapter the basis of the theory of metamaterial are briefly illustrated. In the first section, Drude and Drude-Lorenz models are recalled. Assuming that the concept of DNG or SNG material is always related to specific frequency bands and that real-life structures usually exhibit a much more complex behavior, a usual practice in order to describe real materials and electromagnetic mixtures is to linearly combine those models, providing proper values of the characteristic parameters for each tem of the sum, in order to fit experimental data. Transmission Line (TL) equivalent models of DPS, DNG and SNG media are then given. Finally the problems related to the homogenization of complex materials and the concept of Metamaterial Inspired Device (MID) are exposed, and a classification of Metamaterials in 2D Metamaterials and 3D Metamaterials is presented.

2.1 NEGATIVE PERMITTIVITY AND PERMEABILITY

Let us recall the differential equation describing the effect of an electric field **E** applied to those electrons that, in a metal, are free to move and collide each other [8]:

$$\frac{d\mathbf{v}}{dt}+\frac{\mathbf{v}}{\tau}=\frac{e}{m^*}\mathbf{E} \qquad (2.1)$$

where **v** is the electron velocity, m* the effective mass and τ is the average time between two collisions, also known as relaxation time, the term $1/\tau$ is instead known as damping factor. The current density can be then be written as follows:

$$\mathbf{J}=Ne\mathbf{v} \qquad (2.2)$$

where N is the conduction electrons density, giving:

$$\frac{d\mathbf{J}}{dt}+\frac{\mathbf{J}}{\tau}=\frac{Ne^2}{m^*}\mathbf{E}=\varepsilon_0\,\omega_p^2\,\mathbf{E} \qquad (2.3)$$

Where the term ω_p^2

$$\omega_p = \frac{N e^2}{\varepsilon_0 m^*} \qquad (2.4)$$

is known as plasma frequency, i.e. the characteristic frequency of the electronic cloud oscillation as response to a mechanical or electric stimulus, also known as plasmon. For rapidly oscillating fields:

$$\begin{cases} \mathbf{E} = \mathbf{E_0}\, e^{+j\omega t} \\ \mathbf{J} = \mathbf{J_0}\, e^{+j\omega t} \ , \ \mathbf{J} = \sigma(\omega)\mathbf{E} \\ \dfrac{d\mathbf{J}}{dt} = j\omega \mathbf{J} \end{cases} \qquad (2.5)$$

where σ is the conductivity, solving for $\sigma(\omega)$ we have:

$$\sigma(\omega) = \frac{\varepsilon_0\, \omega_p^2\, \tau}{1 + j\omega\tau} \qquad (2.6)$$

From (2.6) it can be noted that at low frequencies $\sigma(\omega)$ is proportional to τ, consequently, the less are the collisions the highest is the velocity, resulting almost real and independent of frequency. The lattice dielectric constant can be found from Maxwell's equations:

$$\nabla \times \mathbf{H} = j\omega\varepsilon_0 \left[1 + \frac{\sigma(\omega)}{j\varepsilon_0\, \omega} \right] \mathbf{E} \qquad (2.7)$$

The term in square brackets is the definition of relative permittivity, finally:

$$\varepsilon(\omega) = \varepsilon_0 \left[1 + \frac{\dfrac{\varepsilon_0\, \omega_p^2\, \tau}{1 + j\omega\tau}}{j\varepsilon_0\, \omega} \right] = \varepsilon_0 \left[1 + \frac{\omega_p^2}{\dfrac{j\omega}{\tau} - \omega^2} \right] = \varepsilon_0 \left[1 - \frac{\omega_p^2}{\omega\left(\omega - \dfrac{j}{\tau}\right)} \right] \qquad (2.8)$$

A metamaterial whose behavior is consistent with the Drude model can be then obtained by using, for instance, the conductive thin wires array of Figure 2.

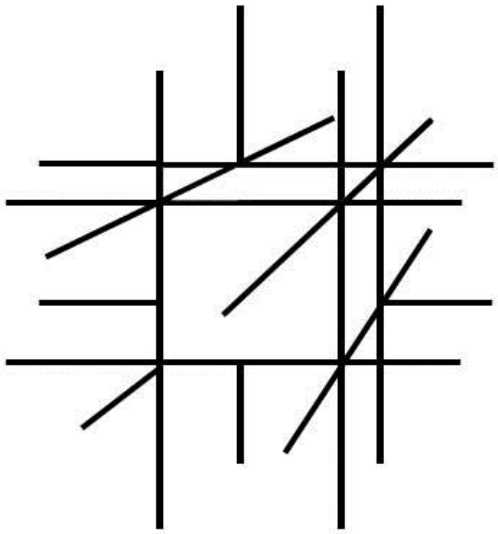

Figure 2 Basic cell of a wire medium exhibiting a Drude-like dispersion of the electric permittivity.

In case wires are not continuous but are cut-wires the Drude model is replaced with the Drude-Lorenz model:

$$\varepsilon(\omega) = \varepsilon_0 \left[1 - \frac{\omega_p^2 - \omega_0^2}{(\omega^2 - \omega_0^2 + \omega \frac{j}{\tau})} \right] \qquad (2.9)$$

where ω_0 is the resonance frequency; and $\varepsilon<0$ in the band $\omega_0<\omega<\omega_p$.

The wire medium has been historically studied in the field of radar technology applications, particularly in the design of high permittivity low loss materials by Brown [9] (see also the comprehensive survey by Collin in [10]), and in simulation of plasmas by Rotman [11]. The same phenomena and applications were rediscovered fifty years later by Pendry, Smith and Shelby, all of them inspired by [9,11].

The way to obtain negative values of the magnetic permeability is similar and relies on arrangements of inclusions of different shape, exhibiting a magnetic behavior, as, for instance, Split Ring Resonators (SRRs). Veselago suggested instead the use of anisotropic gyroscopic substances in which the effective permeability can be negative for one of the two circular polarizations. Moreover, the possibility to achieve negative permeability was

already demonstrated ten years earlier by Thompson [12,13], and again, different experiments led to the same results in the work of Marques [14].

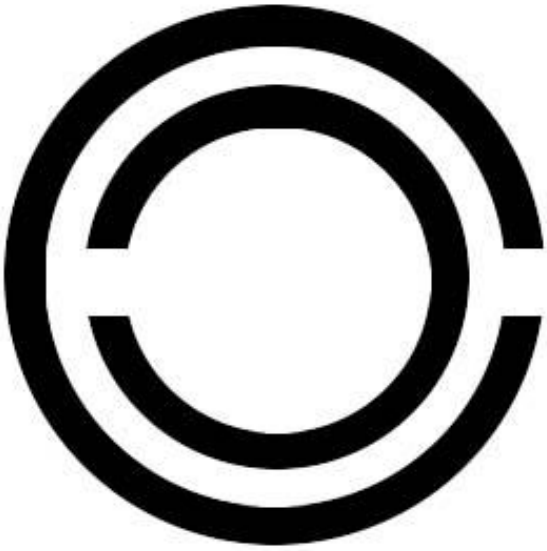

Figure 3 Basic cell of a SRR medium exhibiting a Lorenz dispersion of the magnetic permeability.

In such case Drude-Lorenz model describing this structure is the following:

$$\mu(\omega) = \mu_0 \left[1 - \frac{F}{(\omega^2 - \omega_0^2 + \omega \frac{j}{\tau})} \right] \qquad (2.10)$$

where F is a parameter related to the shape of the structure. A more detailed analysis of this kind of structures is given in [15].

2.2 TRANSMISSION LINE MODEL OF METAMATERIALS

In this section the transmission line model for linear homogenous isotropic media is recalled and specialized in case of metamaterial slabs, deriving a circuital equivalence between DPS,DNG,SNG and distributed constants transmission lines.

Let us recall the expressions of the curl of **E** and **H**, for a linear homogenous isotropic media in the frequency domain, given a monochromatic excitation in the form $e^{j\omega t}$:

$$\begin{cases} \nabla \times \mathbf{E} = -j\omega\mu\,\mathbf{H} \\ \nabla \times \mathbf{H} = j\omega\varepsilon\,\mathbf{E} \end{cases} \tag{2.11}$$

2.2.1 TEM(z) case

Through an arbitrary orientation of the coordinate axis, in the TEM case, it can be always verified $E_z=H_z=0$ and $E_y=H_x=0$:

$$\begin{cases} \dfrac{\partial E_x}{\partial z} = -j\omega\mu\,H_y & (A) \\ \dfrac{\partial E_x}{\partial y} = 0 & (B) \\ \dfrac{\partial H_y}{\partial z} = -j\omega\varepsilon\,E_x & (C) \\ \dfrac{\partial H_y}{\partial x} = 0 & (D) \end{cases} \tag{2.12}$$

From (2.12) it is straightforwardly obtained:

$$\begin{cases} \dfrac{\partial^2 H_y}{\partial z^2} + \omega^2\mu\varepsilon\,H_y = 0 \\ \dfrac{\partial^2 E_x}{\partial z^2} + \omega^2\mu\varepsilon\,E_x = 0 \end{cases} \tag{2.13}$$

From the positions $V(z)=E_x(z)$, $I(z)=H_y(z)$, $\tilde{Z}_{TEM} = j\omega\mu$ and $\tilde{Y}_{TEM} = j\omega\varepsilon$ (2.13) can be written in the characteristic form:

$$\begin{cases} \dfrac{\partial H_x}{\partial z} = -\tilde{Y}_{TEM}\,E_y \\ \dfrac{\partial E_y}{\partial z} = -\tilde{Z}_{TEM}\,H_x \end{cases} \tag{2.14}$$

Called the Telegraphers' Equations, $\tilde{Y}_{TEM}$ and $\tilde{Z}_{TEM}$ are the admittance and the impedance per unit length, functions of the spatial variable *z*, whose dimensions are respectively

[Siemens/m] and [Ohm/m]. If the medium is lossless:

$$\begin{cases} E_x(z) = E_0^+ e^{-j\beta z} + E_0^- e^{j\beta z} \\ H_y(z) = H_0^+ e^{-j\beta z} + H_0^- e^{j\beta z} \end{cases} \qquad (2.15)$$

That can be rewritten as follows:

$$\begin{cases} E_x(z) = E_0^+ e^{-j\beta z} + E_0^- e^{j\beta z} \\ H_y(z) = \frac{1}{Z_0}\left(E_0^+ e^{-j\beta z} - E_0^- e^{j\beta z}\right) \\ Z_0 = \tilde{Z}_{TEM} / (j\beta) = \tilde{Z}_{TEM} / \sqrt{\tilde{Z}_{TEM}\,\tilde{Y}_{TEM}} \end{cases} \qquad (2.16)$$

where Z_0 is the characteristic impedance of the medium (or of the line according to the formalism used):

$$Z_0 = \sqrt{\frac{R + j\omega L}{G + j\omega C}} = \sqrt{\frac{\tilde{Z}_{TEM}}{\tilde{Y}_{TEM}}} = \sqrt{\frac{j\omega\mu}{j\omega\varepsilon}} = \sqrt{\frac{\mu}{\varepsilon}} \qquad (2.17)$$

Moreover, given $E(z)^+ = E_0^+ e^{-j\beta z}$, $H(z)^+ = H_0^+ e^{-j\beta z}$, $E(z)^- = E_0^- e^{j\beta z}$ and $H(z)^- = H_0^- e^{j\beta z}$ (2.16) may be rewritten as follows:

$$\begin{cases} E_x(z) = E^+(z) + E^-(z) \\ H_y(z) = \frac{1}{Z_0}\left(E^+(z) - E^-(z)\right) \end{cases} \qquad (2.18)$$

We now define two functions, the line impedance Z(z) and the reflection coefficient R(z):

$$Z(z) = \frac{E_x(z)}{H_y(z)} = Z_0 \frac{E_0^+ e^{-jz\beta} + E_0^- e^{jz\beta}}{\left(E_0^+ e^{-jz\beta} - E_0^- e^{jz\beta}\right)} \qquad (2.19)$$

$$R(z) = \frac{E^-(z)}{E^+(z)} = \frac{E_0^-}{E_0^+} e^{2jz\beta} \qquad (2.20)$$

Those quantities are found to be mutually dependent:

$$Z(z) = Z_0 \frac{1 + R(z)}{1 - R(z)} \qquad (2.21)$$

$$R(z)=\frac{Z(z)-Z_0}{Z(z)+Z_0} \qquad (2.22)$$

2.2.2 Reflection coefficient for two homogeneous isotropic indefinite dielectric slab in free space

Before analyzing the TE(z) and the TM(z) a useful result is derived in case of two paired homogeneous dielectric slabs, such result will be recalled in Chapter 3 when studying the properties of a conjugate matched pair of SNG slabs. Let us consider four transmission lines connected in series with characteristic impedance Z_0, Z_{01}, Z_{02} and Z_0 respectively, the first extending in the region $z<-d_1-d_2$, the second in $-d_1-d_2 <z<-d_2$, the third in $-d_2<z<0$ and the fourth in $z>0$.

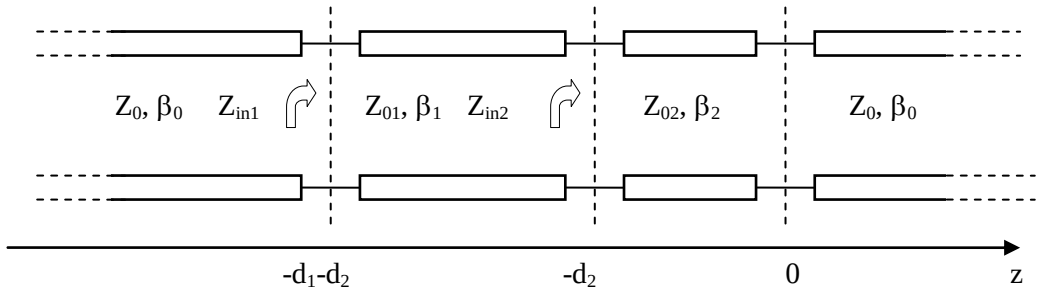

Figure 4 Transmission line representation of a two indefinite homogeneous isotropic dielectric slabs in free space.

To evaluate the reflection coefficient at the interface $z=-d_1-d_2$ is enough to apply the definition introduced in the previous section:

$$Z_{in2}=Z_{02}\frac{Z_0+jZ_{02}\tan(\beta_2 d_2)}{Z_{02}+jZ_0\tan(\beta_2 d_2)} \qquad (2.23)$$

$$
\begin{aligned}
Z_{in1} &= Z_{01}\frac{Z_{in2}+jZ_{01}\tan(\beta_1 d_1)}{Z_{01}+jZ_{in2}\tan(\beta_1 d_1)} = \\
&= Z_{01}\frac{Z_{02}\dfrac{Z_0+jZ_{02}\tan(\beta_2 d_2)}{Z_{02}+jZ_0\tan(\beta_2 d_2)}+jZ_{01}\tan(\beta_1 d_1)}{Z_{01}+jZ_{02}\dfrac{Z_0+jZ_{02}\tan(\beta_2 d_2)}{Z_{02}+jZ_0\tan(\beta_2 d_2)}\tan(\beta_1 d_1)} = \\
&= Z_{01}\frac{Z_{02}\left[Z_0+jZ_{02}\tan(\beta_2 d_2)\right]+jZ_{01}\tan(\beta_1 d_1)\left[Z_{02}+jZ_0\tan(\beta_2 d_2)\right]}{Z_{01}Z_{02}+j\left\{Z_0Z_{01}\tan(\beta_2 d_2)+Z_{02}\tan(\beta_1 d_1)\left[Z_0+jZ_{02}\tan(\beta_2 d_2)\right]\right\}}
\end{aligned}
\tag{2.24}
$$

$$
\begin{aligned}
R(-L) &= \frac{Z_{in1}-Z_0}{Z_{in1}+Z_0} = \\
&= \frac{Z_{01}\dfrac{Z_{02}\left[Z_0+jZ_{02}\tan(\beta_2 d_2)\right]+jZ_{01}\tan(\beta_1 d_1)\left[Z_{02}+jZ_0\tan(\beta_2 d_2)\right]}{Z_{01}Z_{02}+j\left\{Z_0Z_{01}\tan(\beta_2 d_2)+Z_{02}\tan(\beta_1 d_1)\left[Z_0+jZ_{02}\tan(\beta_2 d_2)\right]\right\}}-Z_0}{Z_{01}\dfrac{Z_{02}\left[Z_0+jZ_{02}\tan(\beta_2 d_2)\right]+jZ_{01}\tan(\beta_1 d_1)\left[Z_{02}+jZ_0\tan(\beta_2 d_2)\right]}{Z_{01}Z_{02}+j\left\{Z_0Z_{01}\tan(\beta_2 d_2)+Z_{02}\tan(\beta_1 d_1)\left[Z_0+jZ_{02}\tan(\beta_2 d_2)\right]\right\}}+Z_0} = \\
&= \frac{Z_0\left(Z_{02}^{\,2}-Z_{01}^{\,2}\right)+j\left[\dfrac{Z_{01}\left(Z_{02}^{\,2}-Z_0^{\,2}\right)}{\tan(\beta_1 d_1)}+\dfrac{Z_{02}\left(Z_{01}^{\,2}-Z_0^{\,2}\right)}{\tan(\beta_2 d_2)}\right]}{\dfrac{2Z_0Z_{01}Z_{02}}{\tan(\beta_1 d_1)\tan(\beta_2 d_2)}-Z_0\left(Z_{02}^{\,2}+Z_{01}^{\,2}\right)+j\left[\dfrac{Z_{01}\left(Z_{02}^{\,2}+Z_0^{\,2}\right)}{\tan(\beta_1 d_1)}+\dfrac{Z_{02}\left(Z_{01}^{\,2}+Z_0^{\,2}\right)}{\tan(\beta_2 d_2)}\right]}
\end{aligned}
\tag{2.25}
$$

2.2.3 TM(z) case

Assuming $H_z=0$ and, through an arbitrary orientation of the coordinate system, $E_y=H_x=0$, the following result is achieved:

$$\begin{cases} \dfrac{\partial E_x}{\partial z} = -j\omega\mu H_y + \dfrac{\partial E_z}{\partial x} \\ \dfrac{\partial E_z}{\partial y} = 0 \\ \dfrac{\partial E_x}{\partial y} = 0 \\ \dfrac{\partial H_y}{\partial z} = -j\omega\varepsilon E_x \\ \dfrac{\partial H_y}{\partial x} = j\omega\varepsilon E_z \end{cases} \Rightarrow \begin{cases} \dfrac{\partial E_x}{\partial z} = -j\omega\mu H_y + \dfrac{1}{j\omega\varepsilon}\dfrac{\partial^2 H_y}{\partial x^2} \\ \dfrac{\partial H_y}{\partial z} = -j\omega\varepsilon E_x \end{cases} \qquad (2.26)$$

For a linear isotropic source-free and homogeneous medium **H** satisfies,

$$\begin{cases} \nabla^2 \mathbf{H} + k^2 \mathbf{H} = 0 \\ H_z = 0 \\ H_x = 0 \end{cases} \Rightarrow \begin{cases} \dfrac{\partial^2 H_y}{\partial x^2} = -k_x^2 H_y \\ \dfrac{\partial^2 H_y}{\partial y^2} = -k_y^2 H_y \\ \dfrac{\partial^2 H_y}{\partial z^2} = -k_z^2 H_y \end{cases} \qquad (2.27)$$

leading to:

$$\begin{cases} \dfrac{\partial E_x}{\partial z} = -j\omega\mu H_y - \dfrac{1}{j\cdot\omega\cdot\varepsilon} k_x^2 H_y \\ \dfrac{\partial H_y}{\partial z} = -j\omega\varepsilon E_x \end{cases} \Rightarrow \begin{cases} \dfrac{\partial E_x}{\partial z} = -j\omega\mu_{eq} H_y \\ \mu_{eq} = \mu\left(1 - \dfrac{k_x^2}{\omega^2\varepsilon\mu}\right) \\ \dfrac{\partial H_y}{\partial z} = -j\omega\varepsilon E_x \end{cases} \qquad (2.28)$$

By the positions $\tilde{Z}_{TM} = j\omega\mu_{eq}$ and $\tilde{Y}_{TM} = j\omega\varepsilon$:

$$\begin{cases} \dfrac{\partial H_y}{\partial z} = -\tilde{Y}_{TM} E_y \\ \dfrac{\partial E_x}{\partial z} = -\tilde{Z}_{TM} H_x \end{cases} \qquad (2.29)$$

The characteristic impedance is now defined as:

$$Z_0^{TM} = \sqrt{\frac{\tilde{Z}_{TM}}{\tilde{Y}_{TM}}} = \sqrt{\frac{\mu_{eq}}{\varepsilon}} = \sqrt{\frac{\mu\left(1-\frac{k_x^2}{\omega^2\varepsilon\mu}\right)}{\varepsilon}} \qquad (2.30)$$

2.2.4 TE(z) case

Assuming E_z=0 and, through an arbitrary orientation of the coordinate system, H_y=E_x=0, in analogy with the previous section:

$$\begin{cases} \frac{\partial E_y}{\partial x} = -j\omega\mu H_z \\ \frac{\partial E_y}{\partial z} = j\omega\mu H_x \\ \frac{\partial H_x}{\partial z} = j\omega\varepsilon E_y + \frac{\partial H_z}{\partial x} \\ \frac{\partial H_z}{\partial y} = 0 \\ \frac{\partial H_x}{\partial y} = 0 \end{cases} \Rightarrow \begin{cases} \frac{\partial E_y}{\partial z} = j\omega\mu H_x \\ \frac{\partial H_x}{\partial z} = j\omega\varepsilon E_y - \frac{1}{j\omega\mu}\frac{\partial^2 E_y}{\partial x^2} \end{cases} \qquad (2.31)$$

Again,

$$\begin{cases} \nabla^2\mathbf{E} + k^2\mathbf{E} = 0 \\ E_z = 0 \\ E_x = 0 \end{cases} \Rightarrow \begin{cases} \frac{\partial^2 E_y}{\partial x^2} = -k_x^2 E_y \\ \frac{\partial^2 E_y}{\partial y^2} = -k_y^2 E_y \\ \frac{\partial^2 E_y}{\partial z^2} = -k_z^2 E_y \end{cases} \qquad (2.32)$$

By applying (2.32) to (2.31):

$$\begin{cases} \dfrac{\partial E_y}{\partial z} = j\omega\mu H_x \\ \dfrac{\partial H_x}{\partial z} = j\omega\varepsilon E_y + \dfrac{1}{j\omega\mu} k_x^2 E_y \end{cases} \Rightarrow \begin{cases} \dfrac{\partial H_x}{\partial z} = j\omega\varepsilon_{eq} E_y \\ \varepsilon_{eq} = \varepsilon\left(1 - \dfrac{k_x^2}{\omega^2\varepsilon\mu}\right) \\ \dfrac{\partial E_y}{\partial z} = j\omega\mu H_x \end{cases} \qquad (2.33)$$

Through the positions $\tilde{Z}_{TE} = j\omega\mu$ and $\tilde{Y}_{TE} = j\omega\varepsilon_{eq}$ (2.33) are rewritten in the form:

$$\begin{cases} \dfrac{\partial H_x}{\partial z} = \tilde{Y}_{TE} E_y \\ \dfrac{\partial E_y}{\partial z} = \tilde{Z}_{TE} H_x \end{cases} \qquad (2.34)$$

The characteristic impedance is then defined as:

$$Z_0^{TE} = \sqrt{\frac{\tilde{Z}_{TE}}{\tilde{Y}_{TE}}} = \sqrt{\frac{\mu}{\varepsilon_{eq}}} = \sqrt{\frac{\mu}{\varepsilon\left(1 - \dfrac{k_x^2}{\omega^2\varepsilon\mu}\right)}} \qquad (2.35)$$

2.2.5 Equivalent TL model for DNG and SNG media

From(2.35) and (2.30) the equivalent inductance per length unit L_{eq} and the equivalent capacitance equivalent per length unit C_{eq} may be written:

$$L_{eq}^{TM} \equiv A_1\mu_{eq} = A_1\mu\left(1 - \frac{k_x^2}{\omega^2\varepsilon\mu}\right) \qquad (2.36)$$

$$C_{eq}^{TM} \equiv A_2\varepsilon_{eq} = A_2\varepsilon \qquad (2.37)$$

in the TM case, while in the TE(z) case:

$$L_{eq}^{TE} \equiv A_1\mu_{eq} = A_1\mu \qquad (2.38)$$

$$C_{eq}^{TE} \equiv A_2\varepsilon_{eq} = A_2\varepsilon\left(1 - \frac{k_x^2}{\omega^2\varepsilon\mu}\right) \qquad (2.39)$$

where A_1 and A_2 are two positive terms depending on the geometry of the transmission line. Through the introduction of the terms L_{eq} and C_{eq} the definition of a TL equivalent model, both for evanescent and propagating waves in DPS, DNG and SNG media, is now possible. If μ_{eq} is real negative, L_{eq} results real and negative. It can be assumed that such a negative reactance is due to an effective positive capacitance $-j/\omega C_{eff} = -j\omega|L_{eq}|=$ in a certain frequency range. Consequently, in the transmission line equivalent model, a negative series L_{eq} results in a positive series C_{eff}. By applying the duality principle the case $\varepsilon_{eq}<0$ is straightforwardly obtained.

The quantity k_x is assumed always positive both for a wave propagating in a lossless medium (where $k_x^2 \le \omega^2\mu\varepsilon$) both for an evanescent wave (where instead $k_x^2 > \omega^2\mu\varepsilon$).

In Table I, symbols L-C, C-C, L-L and C-L are used to identify which reactive elements are used as series elements (first letter) and which as shunt element (second letter).

TABLE I

	DPS **($\mu>0, \varepsilon>0$)**	**DNG** **($\mu<0, \varepsilon<0$)**	**ENG** **($\mu>0, \varepsilon<0$)**	**MNG** **($\mu<0, \varepsilon>0$)**
Propagating TM wave **($k_x^2 \le \omega^2\mu\varepsilon$)**	$L_{eq}^{TM}>0 \quad \beta \in \Re$ $C_{eq}^{TM}>0 \quad Z \in \Re$ L-C TL	$L_{eq}^{TM}<0 \quad \beta \in \Re$ $C_{eq}^{TM}<0 \quad Z \in \Re$ C-L TL	Not applicable because $k_x^2 \le \omega^2\mu\varepsilon$ in the case $k_x \in \Re$ for lossless ENG	Not applicable because $k_x^2 \le \omega^2\mu\varepsilon$ in the case $k_x \in \Re$ for lossless MNG
Evanescent TM wave **($k_x^2 > \omega^2\mu\varepsilon$)**	$L_{eq}^{TM}<0 \quad \beta \in \Im$ $C_{eq}^{TM}>0 \quad Z \in \Im$ C-C TL	$L_{eq}^{TM}>0 \quad \beta \in \Im$ $C_{eq}^{TM}<0 \quad Z \in \Im$ L-L TL	$L_{eq}^{TM}>0 \quad \beta \in \Im$ $C_{eq}^{TM}<0 \quad Z \in \Im$ L-L TL	$L_{eq}^{TM}<0 \quad \beta \in \Im$ $C_{eq}^{TM}>0 \quad Z \in \Im$ C-C TL

Propagating TE wave ($k_x^2 \le \omega^2\mu\varepsilon$)	$L_{eq}^{TE}>0 \quad \beta \in \Re$ $C_{eq}^{TE}>0 \quad Z \in \Re$ L-C TL	$L_{eq}^{TE}<0 \quad \beta \in \Re$ $C_{eq}^{TE}<0 \quad Z \in \Re$ C-L TL	Not applicable because $k_x^2 \le \omega^2\mu\varepsilon$ in the case $k_x \in \Re$ for lossless ENG	Not applicable because $k_x^2 \le \omega^2\mu\varepsilon$ in the case $k_x \in \Re$ for lossless MNG
Propagating TE wave ($k_x^2 > \omega^2\mu\varepsilon$)	$L_{eq}^{TE}<0 \quad \beta \in \Im$ $C_{eq}^{TE}>0 \quad Z \in \Im$ C-C TL	$L_{eq}^{TE}>0 \quad \beta \in \Im$ $C_{eq}^{TE}<0 \quad Z \in \Im$ L-L TL	$L_{eq}^{TE}>0 \quad \beta \in \Im$ $C_{eq}^{TE}<0 \quad Z \in \Im$ L-L TL	$L_{eq}^{TE}<0 \quad \beta \in \Im$ $C_{eq}^{TE}>0 \quad Z \in \Im$ C-C TL

TL equivalent model for propagating and evanescent TM and TE waves in DPS, DNG, MNG and ENG media.

2.3 ANALYSIS AND HOMOGENIZATION OF COMPOSITE MEDIA

In accordance with the definition given in Section 1.1, the electromagnetic behavior of metamaterials is usually described in terms of effective parameters, i.e. an effective permittivity and an effective permeability. In the long wavelength limit, in fact, the propagation of electromagnetic fields in complex media can be macroscopically described in terms of average fields. When analytically analyzing a complex media, the calculation of the polarizability of the single inclusion is required as starting point; the small scatterers forming the mixture can be replaced by dipole moments which average into the electric polarization.

$$\begin{cases} <\mathbf{D}>=\varepsilon_{eff}<\mathbf{E}>=\varepsilon_e<\mathbf{E}>+<\mathbf{P}> \\ <\mathbf{f}>=\dfrac{1}{V_{mix}}\displaystyle\int_{V_{mix}}\mathbf{f}(\mathbf{r})dV \end{cases} \qquad (2.40)$$

being ε_e the environment permittivity, and V_{mix} a representative volume of the sample, and

$$\begin{cases} <\mathbf{P}>=n\,\mathbf{p}_{mix} \\ \mathbf{p}_{mix}=\alpha\left(<\mathbf{E}>+d_f<\mathbf{P}>\right) \end{cases} \qquad (2.41)$$

being $< \mathbf{P} >$ the average electric polarization density, $\mathbf{p}_{mix}$ the dipole moment of a single inclusion, n the number density of the inclusion in V_{mix} , α the scalar electric polarizability, d_f the depolarization factor depending on the inclusion shape. Analogous consideration may be done about the effective magnetic permeability μ_{eff}.

The Clausius-Mossotti formula gives the effective electrical parameters of the mixture as function of the polarizabilities and, through the Maxwell-Garnett relation, these polarizabilities are replaced with physical material parameters of the inclusions [10,16]:

The discussion by Belov and Simovski in the field of metamaterials [17] is based on similar ideas, generalizing the Clausius-Mossotti relation with the inclusion of a radiation term.

However, in practical cases, this analytical approach turns out to be unsuccessful due to the initial assumptions of this method: the expression of the polarizability of a single inclusion has to be evaluated, which is a challenging task for complex shapes; secondly, inclusions are required both to be much smaller than the operating wavelength, and weakly interacting with scatterers placed at close distance, meaning that the inter-spacing between particles has to be much greater than the particle size. In the most of the cases inclusions are small but no such small (typically $\lambda/10$) and closely packed to obtain a material with a strong engineered response, taking advantage from the same unwanted coupling. This results can be obviously generalized through the introduction of a coupling term but, in this case, a closed expression for this term is, once again, required.

What is done in practice is to retrieve the characteristic parameters of a complex material from the reflection and transmission coefficients of a sufficiently large sample, so that the retrieved parameters can be assumed as those of a bulk material. This approach can be generalized also for samples of small thickness and for moderate low frequencies at the cost of introducing two transition layers at the sides of the slab [18]. In the most of many practical cases, it is also to be taken into account the effect of the thickness of the sample, the electromagnetic response of a thin sample varies with the thickness until it is large enough that the retrieved parameters can be assumed as those of a bulk material [19].

It is also worth noticing early examples by Lewin [20] concerning the calculation of the

effective permittivity and permeability of a medium loaded with spherical particles (this method have then been successfully applied in the metamaterial context by many authors, see for instance [21,22]) and the work of Brillouin in the field of wave propagation in periodic structures. Part of this work, has been applied for describing wave propagation in periodically loaded transmission lines also known as Transmission Line Metamaterials (TL-MTM) [23-27].

2.4 VOLUME METAMATERIALS VS PLANAR METAMATERIALS

That kind of metamaterials based on magnetic resonators, wires, parallel plates, and in general on arrangements of 3D structures are commonly classified as volume metamaterials. What was found by more than one research group at the same time [23-27] was that a much more cost-effective approach to the design of metamaterials would have relied on periodically loaded standard transmission line structures. Given a classical TL representation of a differential section of a lossless guiding structure, as already seen in Section 2.2:

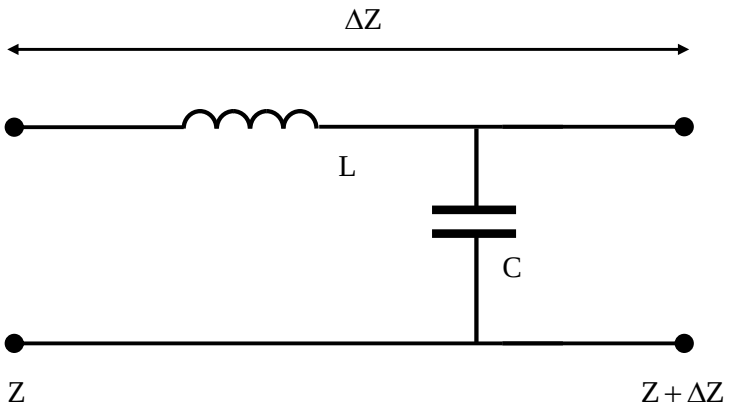

Figure 5 TL equivalent of a standard lossless guiding structure.

When loading such a structure with series capacitors and shunt inductors of proper value, provided a unit cell is smaller than the guided wavelength, in particular $< \lambda_g/4$ [28], so that the line is seen by the electromagnetic waves as effectively homogeneous, a composite left-handed right handed behavior is then expected:

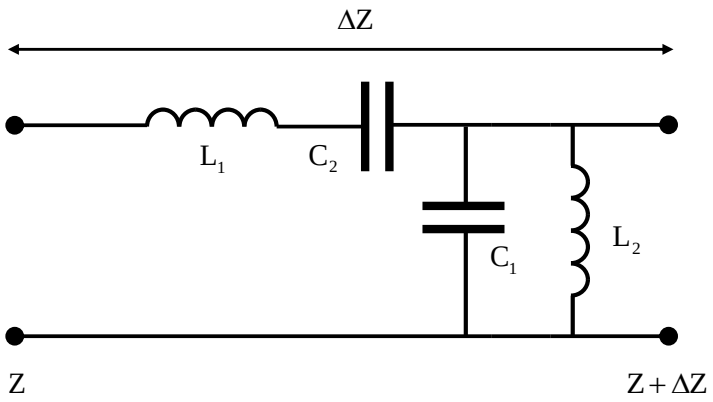

Figure 6 TL equivalent of a composite left-handed right-handed waveguide.

In such a case, the propagation constant, that is defined as the square root of the product between the impedance per-unit length and the admittance per-unit length, is:

$$k = a + jb = \sqrt{Z(\omega)Y(\omega)} = \sqrt{j\left(\omega L_1 - \frac{1}{\omega C_2}\right) j\left(\omega C_1 - \frac{1}{\omega L_2}\right)} = \\ = s(\omega)\sqrt{\omega^2 L_1 C_1 + \frac{1}{\omega^2 L_2 C_2} - \left(\frac{C_1}{C_2} + \frac{L_1}{L_2}\right)} \qquad (2.42)$$

where

$$s(\omega) = \begin{cases} -1 \text{ if } \omega < \min\left(\frac{1}{\sqrt{L_1 C_2}}, \frac{1}{\sqrt{L_2 C_1}}\right) \\ 1 \text{ if } \omega > \max\left(\frac{1}{\sqrt{L_1 C_2}}, \frac{1}{\sqrt{L_2 C_1}}\right) \end{cases} \qquad (2.43)$$

A particular case is found when:

$$L_1 C_2 = L_2 C_1 \qquad (2.44)$$

known as *balance condition*. In such case it can be demonstrated that the propagation constant reduces to:

$$b = \omega\sqrt{L_1 C_1} - \frac{1}{\omega\sqrt{L_2 C_2}} \qquad (2.45)$$

It is clear how the left-hand term is dominant al lower frequencies while, the right-hand term is dominant at higher frequencies. It is also worth noticing that in general, accordingly to (2.42) and to (2.43), the phase constant can be purely imaginary in certain frequency bands resulting in a stop-band behavior that is not found in purely left-handed or purely right handed transmission lines [28].

The technological advantages introduced by the use of such 2D structures have allowed the production of a large literature concerning applications of transmission line metamaterials in the fields of planar filters, antennas and other electromagnetic devices [29-35] due to their easiest and cheapest fabrication process if compared to those of standard volumetric metamaterials. Other applications of this class of metamaterials are illustrated in Chapter 3.

3. METAMATERIAL-BASED AND METAMATERIAL INSPIRED DEVICES

The majority of metamaterial-based devices presented in literature, though exhibiting surprising and exceptional properties, are often found to be extremely challenging in terms of real-life implementation. In fact, when dealing with practical implementations of volumetric metamaterials, the ideal homogeneous equivalent medium, used for the theoretical analysis of such structures and described in terms of an analytical dispersion model, is replaced with an inclusions-based medium. The effects of the inclusion non-idealities often prevail on the advantages that the use of this kind of non-conventional structures should, in principle, imply. This issue is mainly related to the difficulties often found when dealing with the homogenization of inclusion-based metamaterials, fact that becomes more and more important when such devices rely on the interface effects between a conventional medium and an artificial one or between two artificial media. The key point, in these cases, is then the possibility to consider such structures as homogeneous from both a macroscopic and a local point of view and consequently clearly define the electromagnetic properties of their interfaces. The inclusions used in practical case are generally smaller than the operating frequency, thus resulting homogeneous from the macroscopic point of view, but when dealing with boundary problems, from a local point of view, in the most cases, they must be still taken into account as alignments of closely spaced scatterers not able to support the desired interface phenomena. In other applications single miniaturized inclusions are used to achieve the desired results and performance. In this Chapter applications of Metamaterial based 3-D structures are shown in Sections 3.1-3.4 in the field of artificial magnetic conductors, near field plates and power transmission enhancement from sub-wavelength apertures, while in Sections 3.5-3.7, Metamaterial inspired devices are proposed through the use of single magnetic inclusions (Sections 3.5 and 3.7) and complex surfaces characterized by an engineered electromagnetic response (Section 3.6).

3.1 METAMATERIAL SLABS WITH EXTREME VALUES OF THE CONSTITUTIVE PARAMETERS

In this Section, results obtained in Section 2.4 are applied to the case of an homogenous slab made of a metamaterial with special values of both permittivity and permeability. The thickness of the slab is d and the constitutive parameters are defined as: $\varepsilon = \varepsilon_0\varepsilon_r$, $\mu = \mu_0\mu_r$. Considering a plane wave excitation, in the case of a TEM(z), TE(z), TM(z) linear polarizations and angle of incidence θ_{inc} a TL- equivalent representation is given:

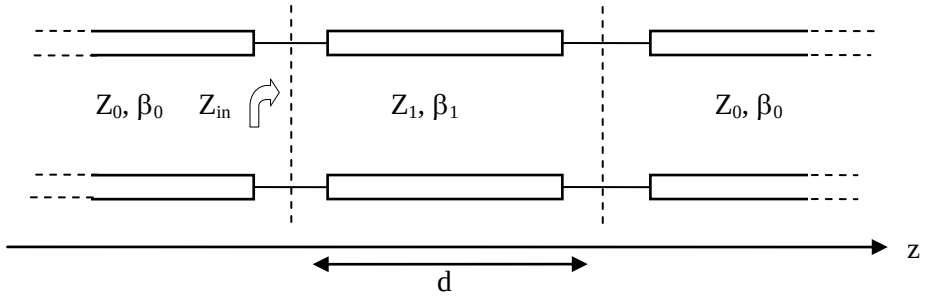

Figure 7 TL-equivalent representation of a plane wave impinging on a metamaterial dielectric slab in free space.

The reflection coefficient *R* at the first interface is evaluated:

$$R = \frac{\left(Z_1^2 - Z_0^2\right)\tan\left(\beta_1 d\right)}{\left(Z_1^2 + Z_0^2\right)\tan\left(\beta_1 d\right) - 2jZ_0Z_1} \qquad (3.1)$$

where Z_0 is the intrinsic impedance of the vacuum, Z_1 the intrinsic impedance of the metamaterial, β_0 the vacuum wave-number, β_1 the wave-number in the metamaterial slab.

In the following, we will consider two special cases, assuming ε_r and μ_r to be real values for simplicity (this assumption is in general incorrect, and an imaginary part is always required in the case of dispersive materials to satisfy Kramers-Kronig relations [8], however it becomes acceptable in case of a point analysis):

$$\lim_{\varepsilon_r \to 0} R, \quad \lim_{\mu_r \to \infty} R \qquad (3.2)$$

3.1.1 TEM(z) polarization

In the case of a TEM polarized wave travelling along the transmission line, the characteristic impedances and the wave-numbers are given by:

$$\begin{cases} Z_0 = \sqrt{\dfrac{\mu_0}{\varepsilon_0}} \\ Z_1 = \sqrt{\dfrac{\mu_0\,\mu_r}{\varepsilon_0\varepsilon_r}} = Z_0\sqrt{\dfrac{\mu_r}{\varepsilon_r}} \\ \beta_0 = \omega\sqrt{\mu_0\varepsilon_0} \\ \beta_1 = \omega\sqrt{\mu_0\,\mu_r\,\varepsilon_0\,\varepsilon_r} = \beta_0\sqrt{\mu_r\varepsilon_r} \end{cases} \qquad (3.3)$$

The reflection coefficient (3.1) is then evaluated:

$$R^{TEM} = \frac{(\epsilon_r - \mu_r)}{-(\epsilon_r + \mu_r) + j2\epsilon_r\sqrt{\dfrac{\mu_r}{\epsilon_r}}\mathrm{Cot}[d\sqrt{\epsilon_0\epsilon_r\mu_0\mu_r}\,\omega]} \qquad (3.4)$$

Through the explicit calculation of limits (3.2) the following results are achieved:

$$\lim_{\varepsilon_r\to 0} R^{TEM} \to \frac{d\epsilon_0\mu_0{\mu_r}^{3/2}\omega}{-2j\sqrt{\epsilon_0\mu_0\mu_r} + d\epsilon_0\mu_0{\mu_r}^{3/2}\omega} \qquad (3.5)$$

$$\lim_{\mu_r\to\infty} R^{TEM} \to 1 \qquad (3.6)$$

Interestingly, both (3.5) and (3.6) lead to the same fundamental results, however, with significant differences. Under proper assumptions, in fact, it is possible to achieve an Artificial Magnetic Conductor (AMC) condition in both cases, but, in order to allow a physical implementation of such materials the magnitude of the slab thickness, electric permittivity and magnetic permeability play an important role.

In the case of (3.5) the AMC condition is achieved, provided moderately high values of permeability (μ_r >25 to have Abs[R]>0.95 and Arg[R]~0.1) or moderately high values of the screen thickness.

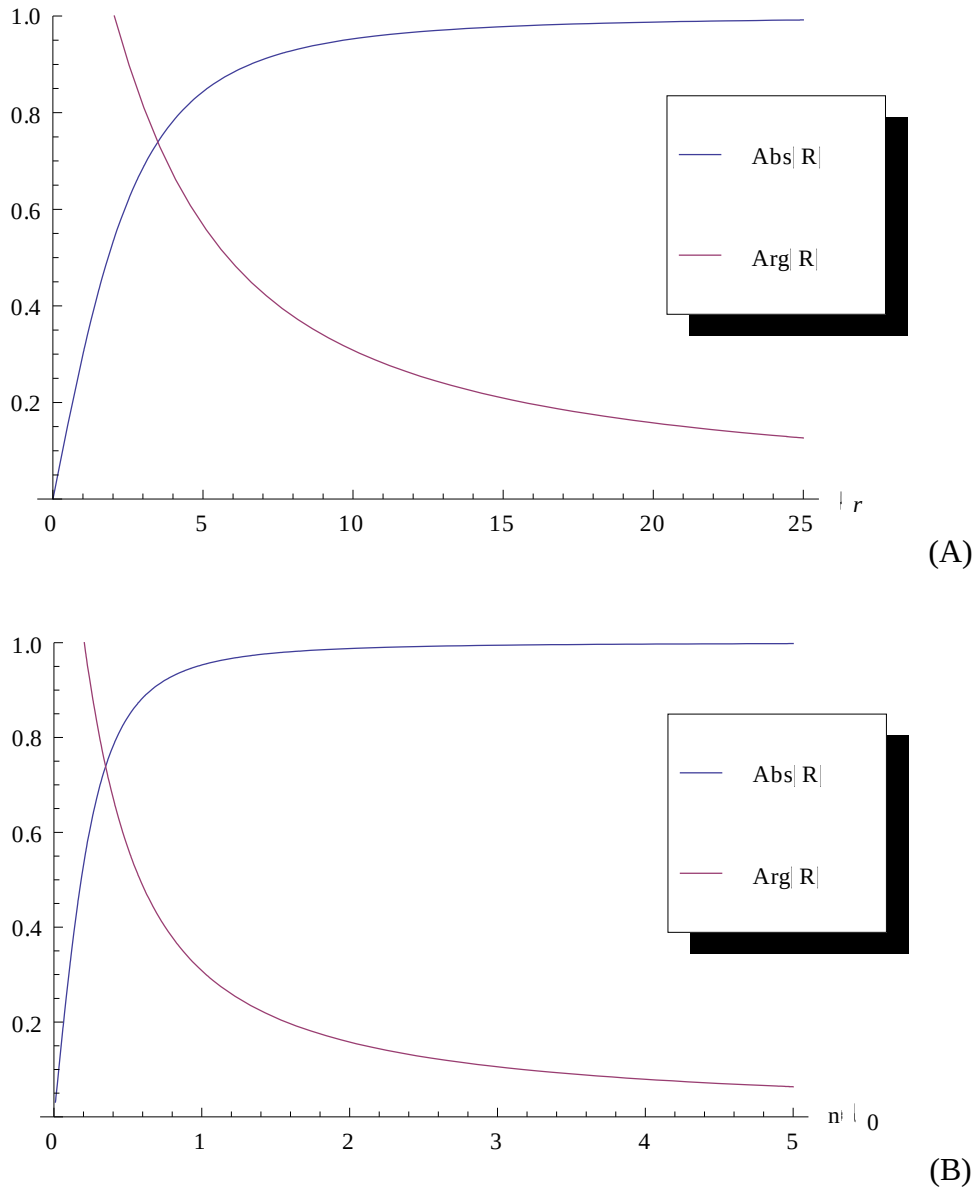

Figure 8 Variation of the reflection coefficient amplitude and phase when $\varepsilon_r \to 0$ with (A) the relative permeability and an electrically thin slab (d = $\lambda_0/10$), with (B) the slab relative thickness (as fractions of λ_0) and μ_r = 1 at a frequency of 3GHz.

In the case of (3.6) the AMC condition is achieved, provided only very high values of magnetic permeability, but the convergence of the limit is achieved through an highly oscillating trend depending on all the significant parameters of the slab.

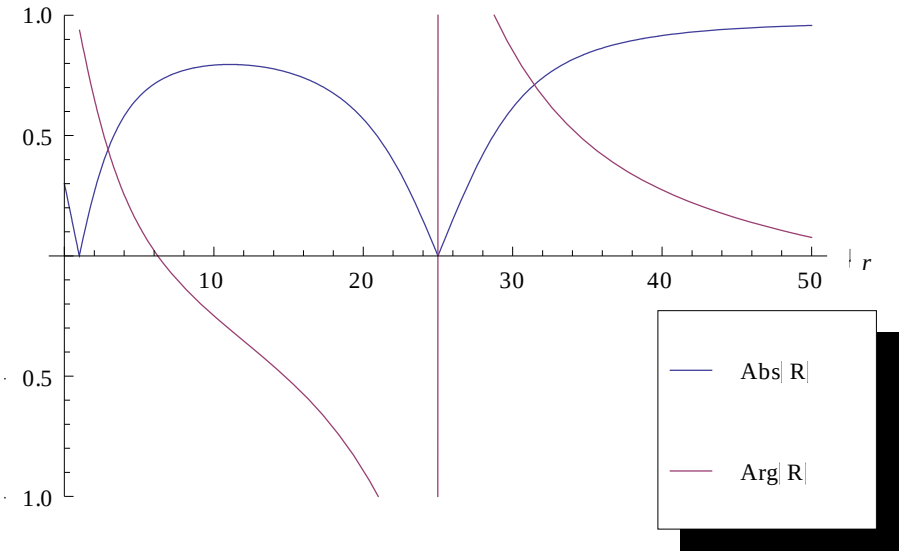

Figure 9 Variation of the reflection coefficient amplitude and phase when $\mu_r \to \infty$ with an electrically thin slab (d = $\lambda_0/10$) and ε_r =1 at a frequency of 3GHz.

3.1.2 TE(z) polarization

Let us assume the case of a TE(z) polarization. The expressions of the intrinsic impedances and wave-numbers are now:

$$\begin{cases} Z_0^{TE} = \omega\mu_0 / \beta_0^{TE} \\ Z_1^{TE} = \omega\mu_0\mu_r / \beta_1^{TE} \\ \beta_0^{TE} = \sqrt{\beta_0^2 - k_x^2} \\ \beta_1^{TE} = \sqrt{\beta_1^2 - k_x^2} \\ k_x = \beta_0 \sin\theta_{inc} \end{cases} \qquad (3.7)$$

being k_x the transverse wave-number and θ_{inc} the angle of incidence on the *xz* plane. In this case, the condition required to have an AMC behavior, regardless of the thickness of the slab, is again the following:

$$\lim_{\mu_r \to \infty} R^{TE} \to 1 \qquad (3.8)$$

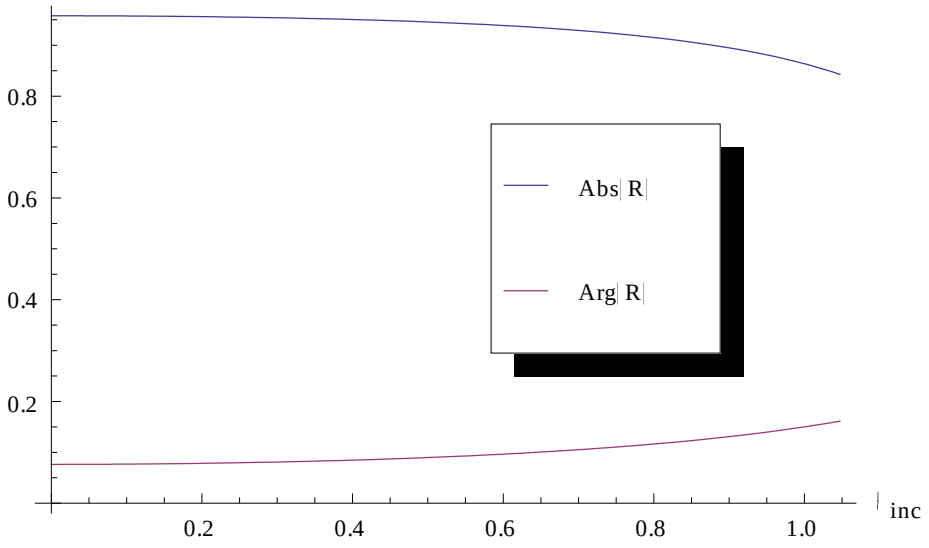

Figure 10 Variation of the reflection coefficient amplitude and phase when $0 < \theta_{inc} < \pi/3$, for an electrically thin slab ($d = \lambda_0/10$), $\mu_r = 50$ and $\varepsilon_r = 1$, at a frequency of 3GHz.

The metamaterial slab should then exhibit a large relative permeability, growing as the maximum allowed incident angle grows.

In case of a vanishing electric permittivity instead:

$$\begin{cases} \lim_{\varepsilon_r \to 0} R^{TE} \to \dfrac{-\mu_r{}^2 + (-1 + \mu_r{}^2)\mathrm{Sin}(\theta_0)^2}{A_1 + A_2} \\ A_1 = -\mu r^2 \mathrm{Cos}(\theta_0)^2 \\ A_2 = 2j\mu_r \sqrt{\mathrm{Cos}(\theta_0)^2}\,\mathrm{Coth}[d\sqrt{\epsilon_0\mu_0}\,\omega \mathrm{Sin}(\theta_0)]\mathrm{Sin}(\theta_0) + \mathrm{Sin}(\theta_0)^2 \end{cases} \qquad (3.9)$$

The AMC-like behavior is still found, similarly to the TEM(z) case, provided, again, a sufficiently high thickness of the metamaterial slab, but only for small incidence angles ($\theta_{inc} < \pi/6$).

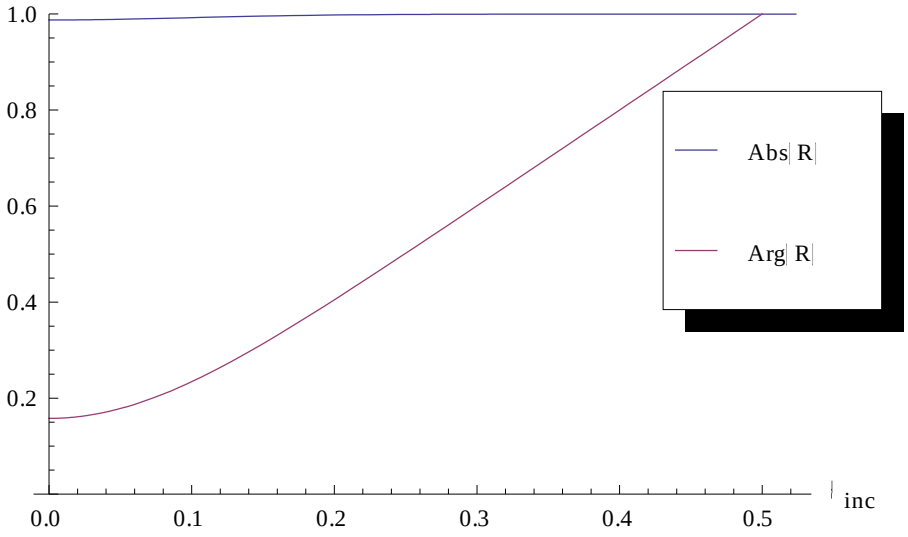

Figure 11 Variation of the reflection coefficient amplitude and phase when $0 < \theta_{inc} < \pi/6$, for an electrically thick slab ($d = 2\,\lambda_0$), $\mu r = 1$ and $\varepsilon_r \to 0$, at a frequency of 3GHz.

The AMC-like behavior of the material slab, in case of a vanishing electric permittivity, improves as the thickness *d* grows, similarly to what has been found for the TEM(z).

3.1.3 TM(z) polarization

In the case of a TM polarized impinging wave, the parameters of the lines are:

$$\begin{cases} Z_0^{TM} = \beta_0^{TM} / (\omega \varepsilon_0) \\ Z_1^{TM} = \beta_1^{TM} / (\omega \varepsilon_0 \varepsilon_r) \\ \beta_0^{TM} = \sqrt{\beta_0^2 - k_x^2} \\ \beta_1^{TM} = \sqrt{\beta_1^2 - k_x^2} \\ k_x = \beta_0 \sin\theta_{inc} \end{cases} \qquad (3.10)$$

Interestingly, for this particular polarization, it is always found:

$$\lim_{\varepsilon_r \to 0} R^{TM} \to 1 \qquad (3.11)$$

$$\lim_{\mu_r \to \infty} R^{TM} \to 1 \qquad (3.12)$$

regardless of the actual value of both the angle of incidence and the thickness of the slab. However, in real-life structures the tolerance of the structures to a mismatching of the electrical parameters plays an important role, in Figure 12 the effect of small variations of the electric permittivity is shown.

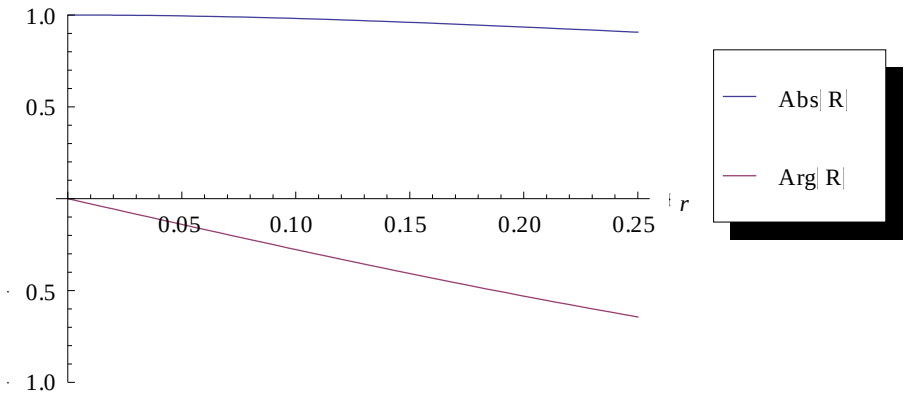

Figure 12 Variation of the reflection coefficient amplitude and phase with electric permittivity, for an electrically thin slab ($d = \lambda_0/10$), $\mu_r = 1$ and $\theta_{inc} = \pi/4$, at a frequency of 3GHz.

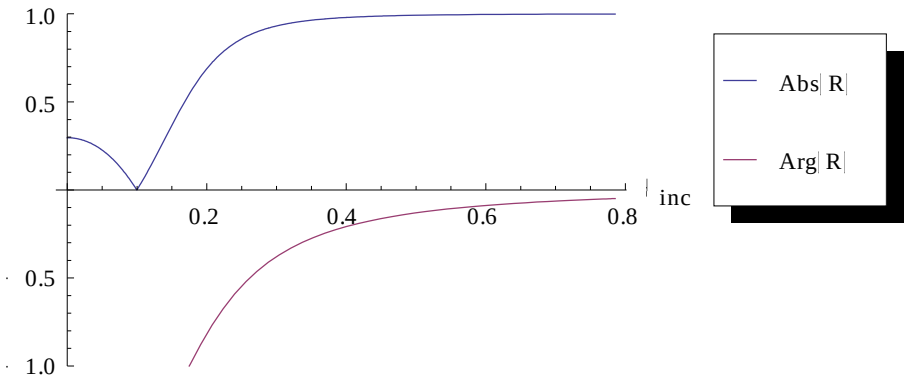

Figure 13 Variation of the reflection coefficient amplitude and phase when $0 < \theta_{inc} < \pi/6$, for an electrically thin slab ($d = \lambda_0/10$), $\mu_r = 1$ and $\varepsilon_r = 1/100$, at a frequency of 3GHz.

Figure 13 also suggests the use of a epsilon near zero slab as a spatial filter. In case of electrically thin screens and small values of the electric permittivity the screen reflects all

the components of an impinging radiation characterized by $|\theta_{inc}| < \Delta\theta$ letting the others pass through. The angle $\Delta\theta$ decreases as the electric permittivity vanishes:

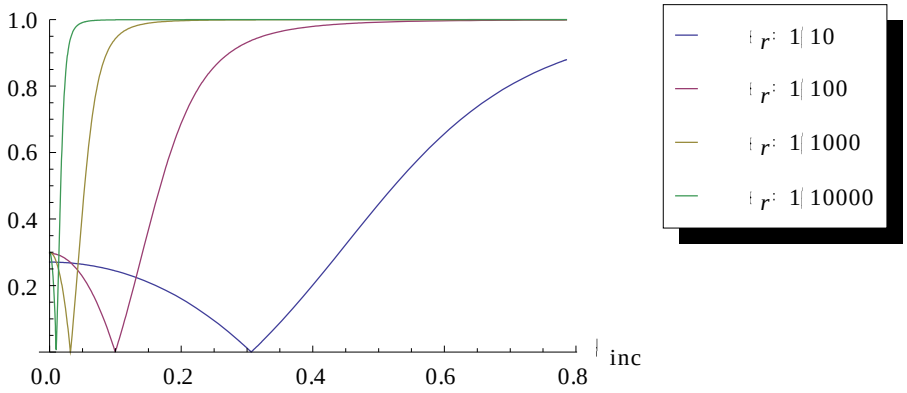

Figure 14 Variation of the reflection coefficient amplitude and phase when $0 < \theta_{inc} < \pi/4$, for an electrically thick slab ($d = \lambda_0/10$), $\mu_r = 1$ and $\theta_{inc} = \pi/4$, at a frequency of 3GHz.

An approximated analytical solution for $\Delta\theta$ is found:

$$\begin{cases} \Delta\theta / 2 = \mathrm{ArcSin}\left(\dfrac{\sqrt{\epsilon_r}}{\sqrt{1+\epsilon_r}} \right) + 2\pi C \\ C \in \mathbb{N} \end{cases} \qquad (3.13)$$

assuming $d \ll \lambda$, $\theta_{inc} \ll \pi/4$ and $1 \gg \varepsilon_r > 0$

3.2 EPSILON NEAR ZERO REFLECTORS AT THZ

From the result achieved in Section 3.1, the design details of AMCs at THz scale is illustrated through the employment of volumetric metamaterials. At the microwave frequencies, it is known from literature [37] that AMCs can be obtained through the use of high-impedance surfaces (HISs), which are complex profile metallic surfaces exhibiting noticeably high values of the surface impedance in a given frequency range.

The idea of using volumetric metamaterials at microwaves to design HISs has been already presented in [38]. However the characteristic dispersion and losses affecting real-life materials suggest the use of those structures more in the field of absorbers [39] (even if characterized by a narrow bandwidth yet small size in comparison to a Salisbury screen absorber [40]) than in that of reflectors. In addition, in the frequency ranges where natural magnetism is achieved, such magnetic materials like ferrites may be applied to get the desired AMC-like behavior; anyway, natural magnetism is no longer available as the frequency increases, and artificial magnetic materials have to be designed.

In [41] the possibility to synthesize AMCs in the visible regime is described and an application to nano-antennas is proposed: the idea is to get directive optical nano-radiators. In [42,43], in fact, plasmonic nano-dipoles and Hertzian nano-dimers have been studied to reproduce at higher frequencies the radiation properties of typical radio-frequency antennas. In order to get directive optical radiators, an ENZ material is a suitable candidate to design reflectors working in the visible. The antenna can be then placed in close proximity to the reflector, resulting thus in a very compact setup. Even if at visible frequencies it is hard to find natural materials with low values of permittivity, it is possible to synthesize an artificial ENZ media through properly designed multi layered structures made of plasmonic and non-plasmonic slabs, as already presented in [44,45] for different applications. If the thicknesses of the layers are electrically small, the resulting medium may be described through effective constitutive parameters depending on the thickness ratio and the relative permittivity of the two materials (the thickness is assumed along the z axis, while x and y subscripts refer to the transverse directions):

$$\begin{cases} \varepsilon_x = \varepsilon_y = \dfrac{\varepsilon_1 + \eta\varepsilon_2}{1+\eta} \\ \varepsilon_z = \dfrac{1}{1+\eta}\left(\dfrac{1}{\varepsilon_1} + \dfrac{\eta}{\varepsilon_2}\right) \\ \eta = \dfrac{d_2}{d_1} \end{cases} \qquad (3.14)$$

In Figure 15 and Figure 16, the directivity of a silver plasmonic nano-dipole with an ENZ reflector is shown.

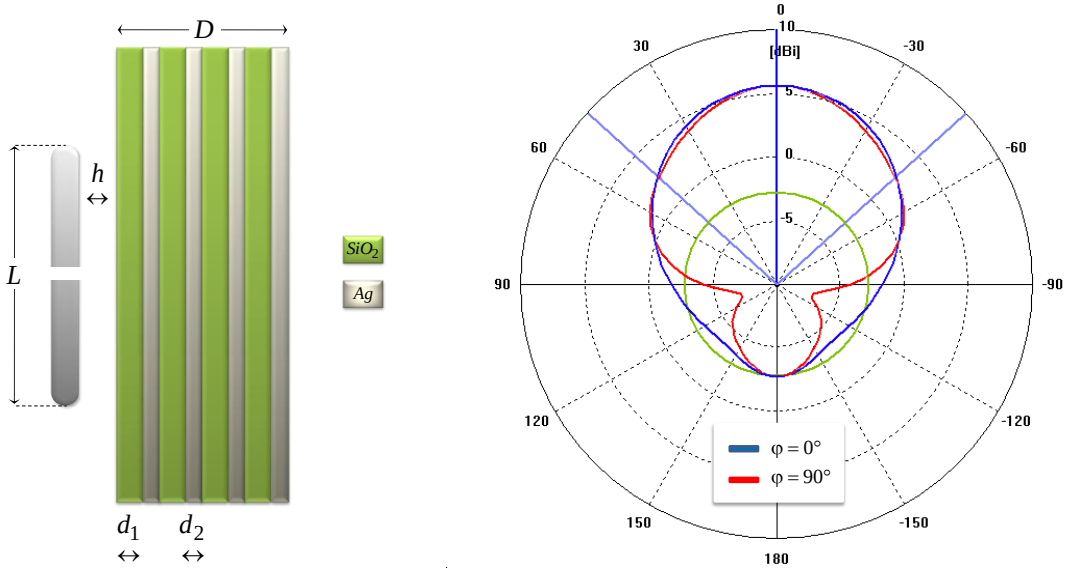

(a) (b)

Figure 15 a) Layout of a nano-dipole of length *L=160 nm* backed by a layered medium of thickness *D* = 125 nm at a distance *h = 3 nm*. The transverse size of the layered screen is $\lambda_0 x \lambda_0$, and it is made of 10 pairs of slabs of silica (d_1*=10 nm*) and silver (d_2*= 2.5 nm*). b) Radiation patterns of the antenna at the operating frequency of *600 THz* on the two principle planes. (Pictures from ref. 41)

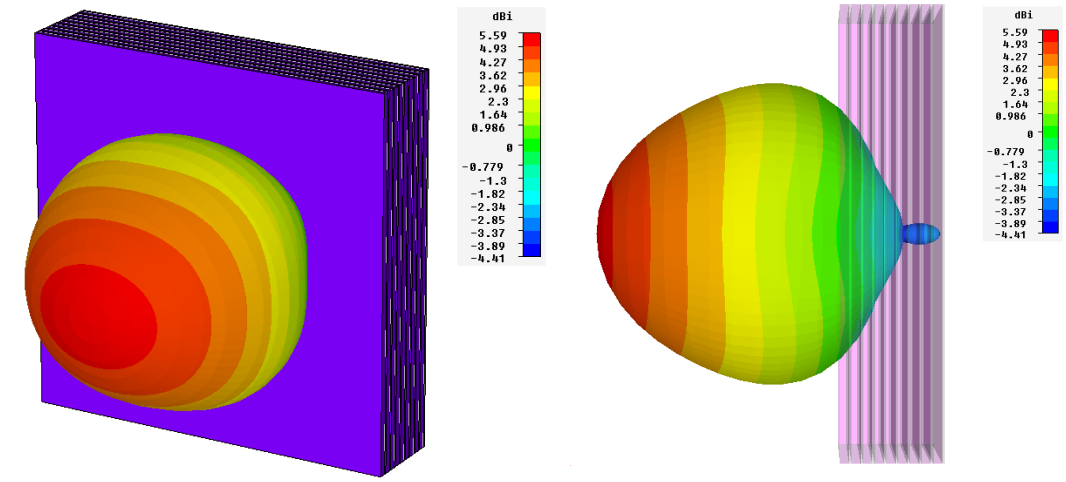

Figure 16 3D radiation pattern of the silver nano-dipole backed by an ENZ reflector synthesized through stacked alternating layers of plasmonic and non plasmonic materials. The geometric parameters are the same as in Figure 15. (Pictures from ref. 41)

3.3 NEAR FIELD PATTERN SYNTHESIS TROUGH NANO-CIRCUIT SURFACES

In this Section, the design of a reactive artificial screen is studied to synthesize a prescribed field patter at optical frequencies as shown in [46,47]. The screen, designed according to the recently proposed new concept of *nanocircuit*, consists in a discrete set of dielectric cells,. The spatial distribution of the cells is tuned to allow the focalization of a sub-wavelength spot beyond the diffraction limit at a prescribed focal distance.

The use of complex engineered artificial surfaces has been experimentally demonstrated at microwaves by Merlin [48,49]. This kind of surfaces are able to modify the phase front of an incident wave (of prescribed polarization), reconstructing a target sub-wavelength pattern at a given distance in the near field.

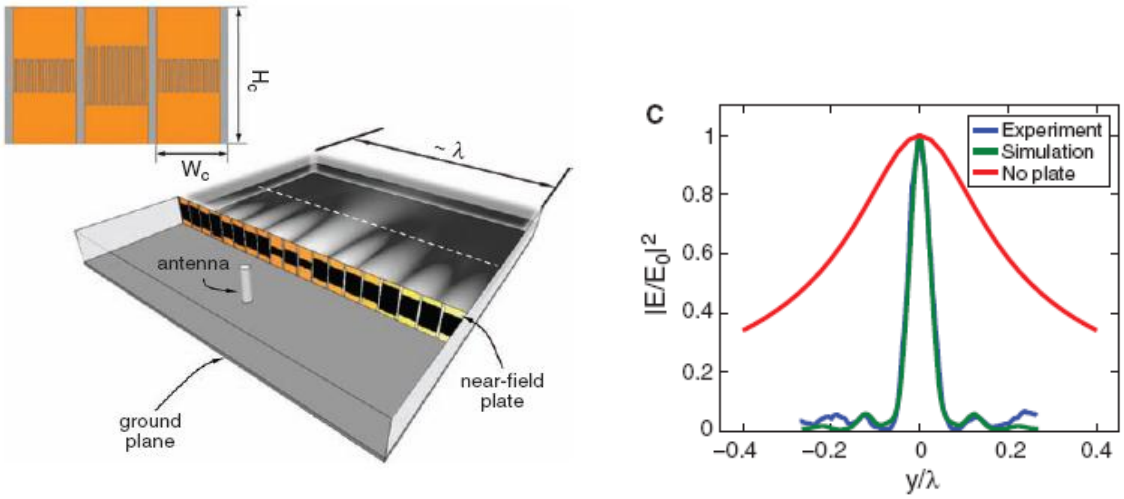

Figure 17 Experimental setup proposed by Merlin, consisting in the juxtaposition of interdigital capacitors of proper value. (Pictures from ref. 49)

At optical frequencies, the synthesis of patterns with sub-wavelength features has been demonstrated through the use of Fresnel Zone plates with metallic coatings [50], in [46,47] instead, an inhomogeneous spatial distribution of the electric permittivity $\eta(x,y)$ is used. Moreover, the possibility to achieve a sub-wavelength desired pattern at arbitrary distances is suggested in [46,47] by using active media. The extreme values of the required distribution of permittivity can be obtained in principle through the recent advancements in metamaterial technology, allowing the fabrication of extremely miniaturized cells exhibiting both high values of reactance and a tunable active behavior.

The unit cells forming the screen are made of a dielectric materials with certain electric parameters and they are characterized by sub-wavelength dimensions. According to the theory developed in [27], for a given polarization of the field impinging on such an elements, it is possible to derive the corresponding element impedance, by replacing the conductive current by the displacement current and defining, this way, a voltage drop across the nano-element. The current flowing though the cross-section of the element in Fig. 2 can be written as:

$$I_{diel} = j\omega\Phi_E = j\omega\int_A \mathbf{D}\cdot d\mathbf{s} = j\omega DA_T = j\omega\varepsilon EA_T \quad (3.15)$$

while the voltage drop along the nano-element is given by:

$$V = \int_A \mathbf{E} \cdot d\mathbf{l} = E\,\ell \qquad (3.16)$$

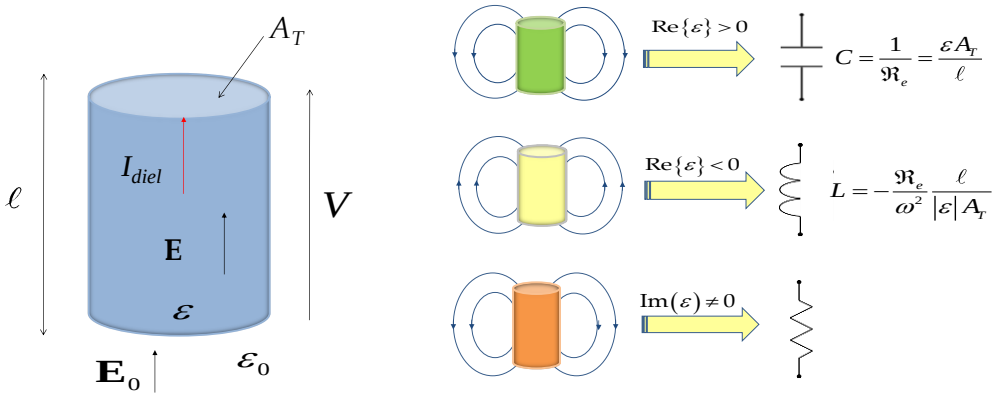

Figure 18 The dielectric cell realizing a reactive element at optical frequencies. Its circuit behavior is mainly determined by the sign of the real part of the electric permittivity and by its imaginary part. (Pictures from ref. 47)

The corresponding impedance is then given by:

$$\dot{Z} \equiv \frac{V}{I_{diel}} = \frac{1}{-i\omega}\frac{V}{\phi_e} = \frac{1}{-i\omega}\Re_e, \quad \Re_e = \frac{\ell}{\varepsilon A_T} \qquad (3.17)$$

where ε is the permittivity of the material, A_T the cross-section of the nano-element and ℓ its height. In [27] it is shown that if $\varepsilon > 0$ this nano-element behaves like a capacitor, while if $\varepsilon < 0$ it behaves as an inductor, and if $\varepsilon = 0$ like an insulator being **D**=0.

The expressions (3.15) and (3.16) are valid under the assumption that the leakage flux through the nano-element can be neglected, having assumed the current along the nano-element axis as uniform; moreover, any coupling among the elements must be avoided.

It is known from [48,49] that once $\eta(x,y)$ is obtained, the impedance spatial distribution must be sampled, assuming each element, whose effective impedance value samples $\eta(x,y)$, to be electrically close to the others and the focal plane distance to be small compared to the wavelength. This way, the negative real part of $\eta(x,y)$ can be neglected,

fact that implies the passivity of the proposed device (otherwise, in order to get a sub-wavelength pattern synthesis in far-zone some form of amplification is needed), and $\eta(x_i, y_i)$ at the sample points turns to be purely capacitive. The proper value of the capacitance for each cell of the screen is then found from (3.17) as:

$$C = \varepsilon \frac{A_T}{\ell} \qquad (3.18)$$

In addition, the electric flux Φ_E couples elements electrically close to the others, establishing unwanted series and parallel connections [27]. In order to reduce both the coupling among the cells and the electric flux leakage, an epsilon-near-zero cover must be used [51]. Therefore, the final layout of the unit cell is as follows: an inner dielectric element with an electric permittivity $\varepsilon > 0$, which realizes the sampled value of the screen capacitance at a certain point, surrounded by an outer cover with an electric permittivity $\varepsilon \simeq 0$, realizing the insulator as depicted in Figure 19.

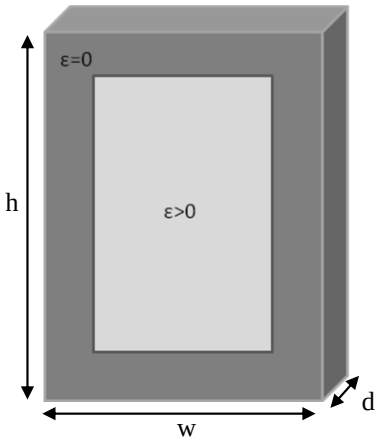

Figure 19 The final layout of the cell realizing a capacitance sampled value on the screen. The outer cover implements the insulator. The inner dielectric box represents the capacitive element. The unit cell size is 12.5 nm×25 nm×5 nm (w×h×d). (Pictures from ref. 47).

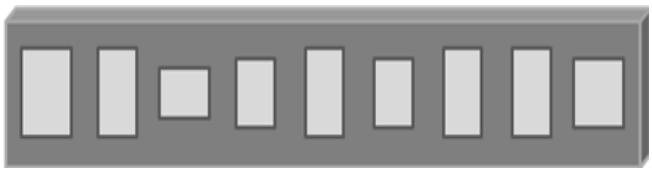

Figure 20 Actual implementation of a 1D reactive screen working at optical frequency. (Pictures from ref. 47).

Assuming we want to synthesize the following 1-D field pattern at the plane $z = z_0$:

$$\mathbf{E}_{\text{synt}}(x)\Big|_{z=z_0} = A_0\,\hat{\mathbf{y}}\,\frac{\sin(k_{\text{res}}x)}{x} \qquad (3.19)$$

where $k_{res} = 2\pi / \lambda_d$ and λ_d is the sub-wavelength resolution of the surface. In order to keep the design of the screen as simple as possible, all the elements are required to be made of the same dielectric material (silicon carbide). The design frequency has been set to f_0*=600 THz*, where the silicon carbide exhibits a relative permittivity of ε_r*=7.1*. This high value of ε_r results in a significant reduction of the screen thickness. The reactive values, required to synthesize the pattern described by (3.19), are obtained by tuning the dimensions of each element. Accordingly to [46,47,48,49] the following values of dielectric cell reactance are found:

TABLE II

Element	Cell Size	Reactance V/A
0	8.9 × 6 × 5	11.08×10^{-6}
1 & -1	10.5 × 4 × 5	19.61×10^{-6}
2 & -2	5.9 × 6 × 5	7.34×10^{-6}
3 & -3	7.0 × 6 × 5	8.71×10^{-6}
4 & -4	5.9 × 6 × 5	7.34×10^{-6}
5 & -5	7.2 × 6 × 5	8.96×10^{-6}
6 & -6	4.6 × 6 × 5	5.72×10^{-6}
7 & -7	6.2 × 6 × 5	7.72×10^{-6}
8 & -8	5.3 × 6 × 5	6.60×10^{-6}
9 & -9	6.2 × 6 × 5	7.72×10^{-6}
10 & -	4.5 × 6 × 5	5.60×10^{-6}
11 & -	6.0 × 6 × 5	7.47×10^{-6}
12 & -	4.8 × 6 × 5	5.97×10^{-6}
13 & -	6.0 × 6 × 5	7.47×10^{-6}
14 & -	4.8 × 6 × 5	5.97×10^{-6}
15 & -	6.2 × 6 × 5	7.72×10^{-6}
16 & -	3.8 × 6 × 5	4.73×10^{-6}
17 & -	5.8 × 6 × 5	7.22×10^{-6}
18 & -	8.4 × 6 × 5	10.46×10^{-6}
19 & -	9.0 × 6 × 5	11.20×10^{-6}

Impedance values of the meta-screen cells

The structure shown in Figure 21 is excited by an electrically small horizontal slit (*25 nm* × *5 nm*) on an opaque screen illuminated by a plane TEM wave, placed *35 nm* apart from the reactive screen (see Fig. 5). The focusing plane is set at a distance z_0*=35 nm* from the screen along the positive propagation axis, and the corresponding amplitude of the *y* component of the electric field at *600 THz* is reported in Figure 22

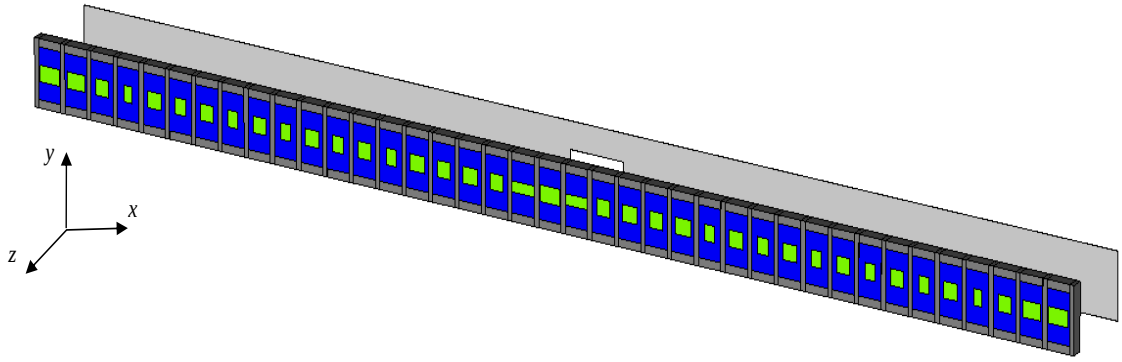

Figure 21 1-D implementation of an optical near-field artificial screen made of 39 reactive elements, designed in order to produce a sinc pattern at the focal plane. The screen dimensions are 487 nm × 25 nm × 5 nm, the green color corresponds to the silicon carbide cells, the blue color to the epsilon-near-zero material and the grey color to the opaque screen. (Pictures from ref. 1).

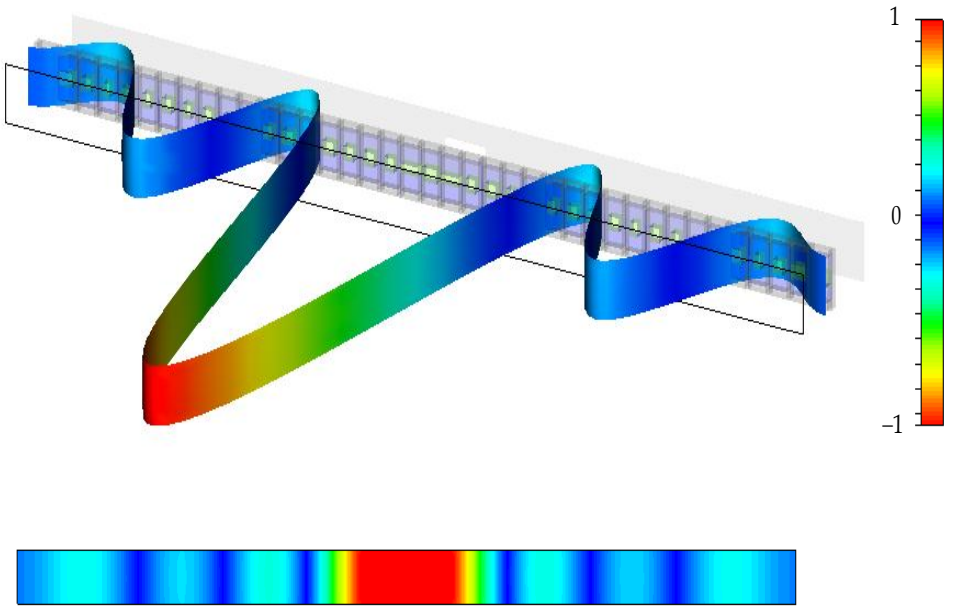

Figure 22 Normalized electric field amplitude at the design frequency (*600 THz*) on the focal plane (*35 nm* apart from the screen). (Pictures from ref. 47).

The main lobe of the *sinc* pattern decays to a half of the peak amplitude at a distance $x \approx 31$ *nm* resulting, thus, in a surface sub-wavelength feature $\lambda_d \approx 103$ *nm*, which is beyond the diffraction limit.

In Figure 23, instead, the pattern distribution at different distances from the screen is shown: diffraction starts occurring at the focal distance.

In Figure 24 the results in case of small changes of the operating frequency is shown to evaluate the bandwidth performances of the proposed screen,. The intrinsic dispersive behavior of the materials used in the design of such a complex patterned surface leads to very narrow-band performances.

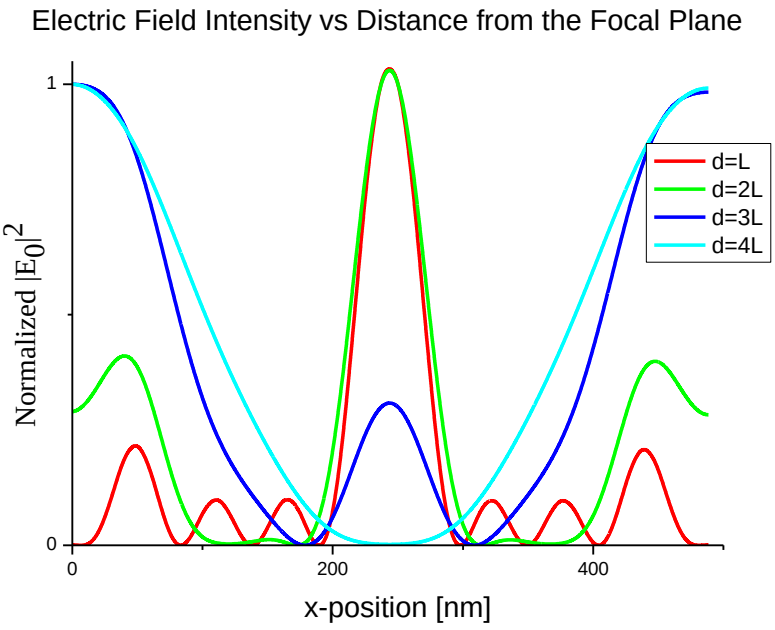

Figure 23 Normalized electric field amplitude at the design frequency (*600 THz*) as a function of the distance from the screen (*L=35 nm*). (Pictures from ref. 47).

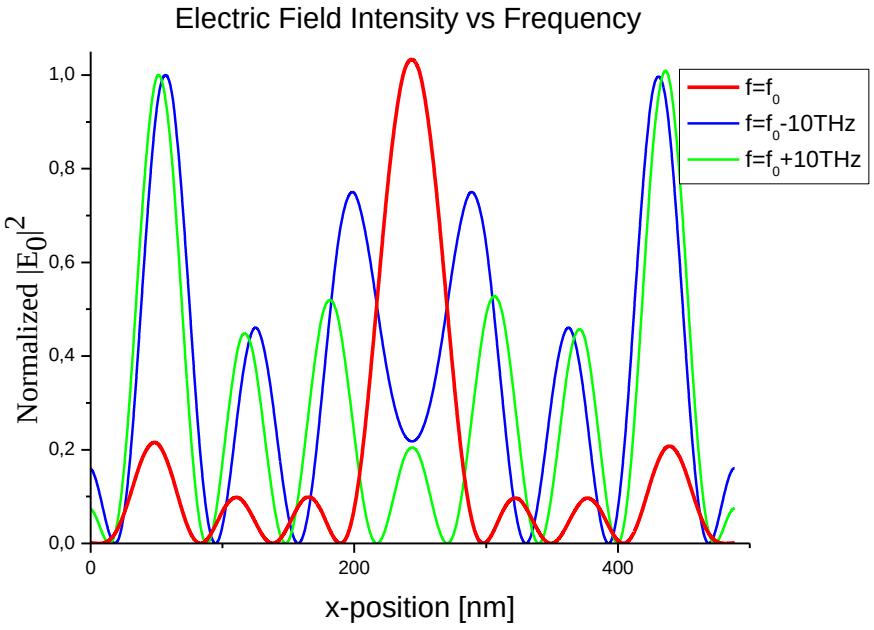

Figure 24 Normalized electric field amplitude at different frequencies. (Pictures from ref. 47).

The aforementioned design procedure can be easily applied to a 2-D case, in Figure 25 a meta-screen made 17x17 cells is presented (results of an analytical calculation are obtained by imposing a 2-D distribution equivalent to the one in (3.19) and by using the same electrical and geometrical reference parameters used for the structure in Figure 21).

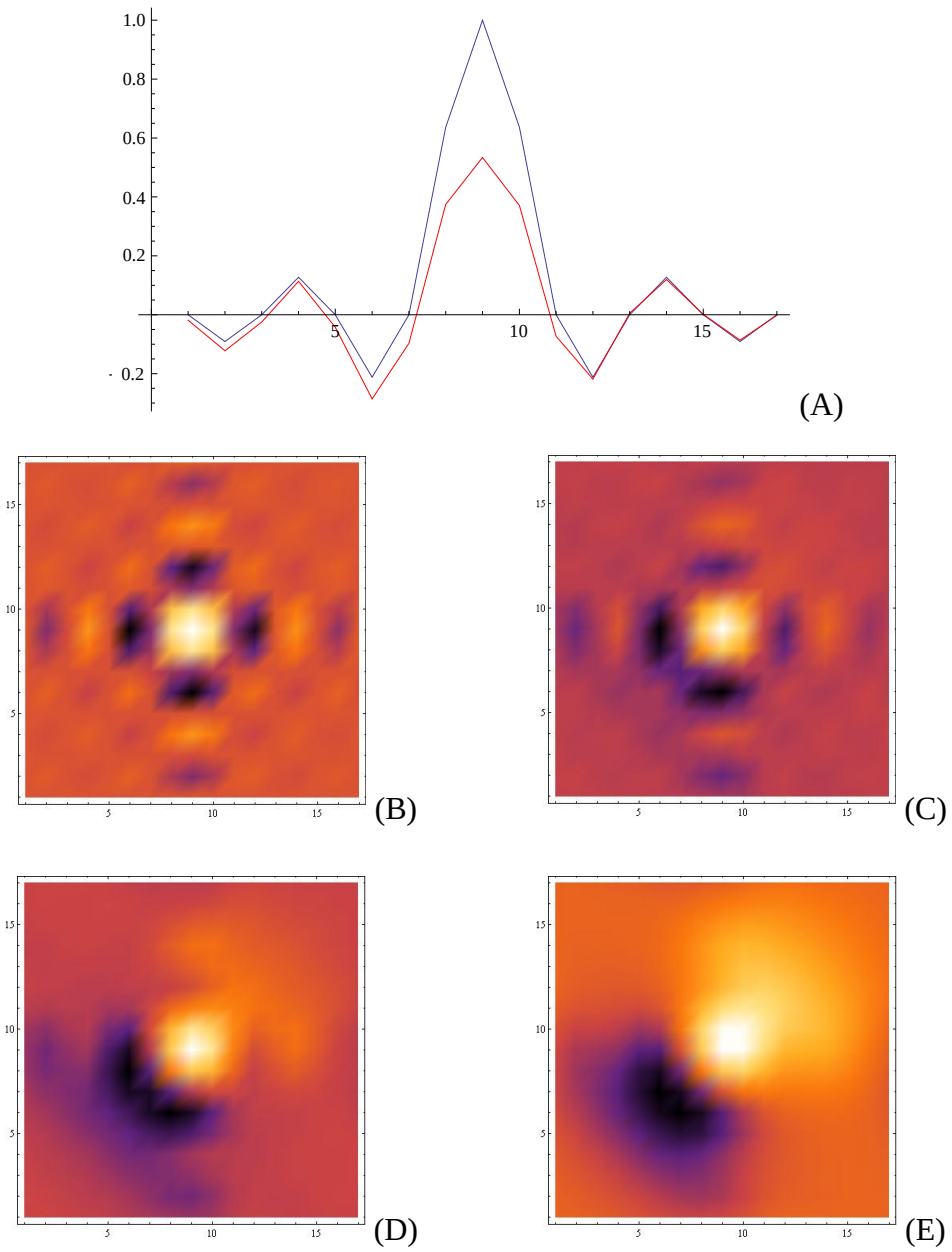

Figure 25 (A) Prescribed (blue) and reconstructed (red) pattern for a linearly polarized plane wave excitation at 300 THz. The red pattern has been obtained by neglecting the real part of η. The screen is made of 17x17 cells, and the surface impedance is sampled at a rate $q=32/\lambda_0$. The 2D pattern amplitude distribution at a distance (B) d=L ,(C) d=2L, (D) d=3L, (E) d=4L (d) where $L=\lambda_0/24$ is the distance of the screen from the focal plane.

3.4 ENHANCED TRANSMISSION THROUGH SPLIT RING RESONATORS AND OTHER KINDS OF SMALL RESONATORS

At the beginning of this Section SNG conjugate media are employed in the design of electrically small covers to enhance the power transmission of a sub-wavelength aperture placed in a perfect electric screen. The important result that only a single SNG cover is needed in order to increase the power transmission is then achieved. Finally, the use of single resonating structures placed in close proximity to the aperture is then investigated.

3.4.1 Power transmission through electrically small apertures

According to Bethe's theory [52], the power transmission through a sub-wavelength aperture is small and it goes as the fourth power of the linear electrical dimension of the aperture:

$$T_0 \sim \left(\frac{a}{\lambda}\right)^4 \qquad (3.20)$$

being T_0 the transmitted power, a the linear geometrical dimension of the aperture (e.g. the radius in the case of a circular aperture) and λ the wavelength of the radiation impinging on the screen. As a first approximation, the transmission through the aperture can be modeled as due to both an equivalent magnetic dipole moment parallel to the screen and an equivalent electric dipole moment normal to the screen.

The enhancement of the power transmission through a single sub-wavelength aperture is useful in several fields of application, such as: high-resolution spatial filters, high-capacity switches, microwave ultra-diffractive imaging systems, high-precision laser lithography, etc.

Following Bethe's theory, in order to increase the power transmission through a sub-wavelength aperture, the amplitudes of either or both the magnetic and the electric equivalent dipole moments need to be significantly increased. To the author's best knowledge, one of the most commonly used approaches in literature is based on the excitation of proper leaky-modes on the metallic screen [53,54]. In order to excite the

required leaky-modes, different setups have been proposed at optical and microwave frequencies, such as: periodic corrugations on the metallic screen [55], metamaterial covers with near-zero electrical parameters [56], conjugate metamaterial bi-layers as covers on both sides of the aperture [57,58].

Since all these setups are based on the excitation of highly-directive leaky-modes (i.e. leaky modes with a small value of the imaginary part of the propagation constant), the typical needed transverse size of the covers around the sub-wavelength aperture is electrically large, limiting the employment of these setups in many practical applications. In addition, the excitation of the leaky-modes is rather challenging in setups based on real-life metallic inclusions and it is highly sensitive to slight variations of both the geometrical and the electrical parameters and to the angle of the incidence radiation [57,58].

In this Section many different setups both based on a different physical mechanism rather than the leaky-wave excitation are illustrated. The proposed setups employ SNG metamaterial covers or single resonant inclusions, characterized by dramatically smaller dimensions with respect to the ones previously proposed and based on the excitation of leaky-wave modes. Furthermore, the design details of the proposed layouts are consistent with the commonly used fabrication techniques and their electromagnetic response is verified through full-wave simulations.

3.4.2 The double SNG cover

The first proposed setup is reported in Figure 26. An infinite perfect conducting (PEC) thin screen with a sub-wavelength aperture is sandwiched between an MNG slab placed on the right side of the screen and an ENG slab placed on the left side. The structure is surrounded by vacuum and the excitation consists of a normally incident monochromatic plane wave coming from the right side of the structure ($\theta_{inc} = 0$).

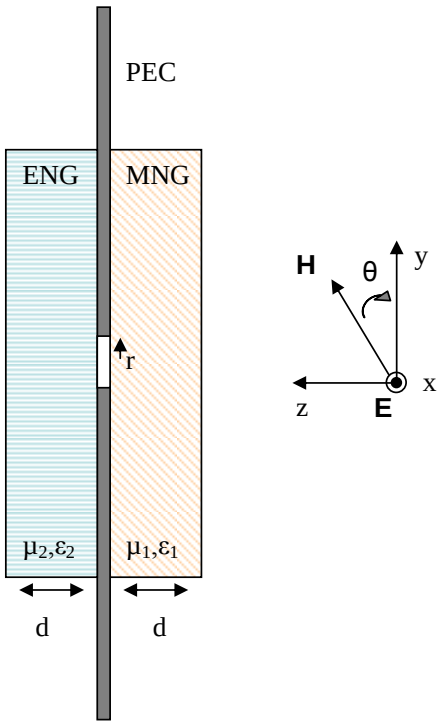

Figure 26 Geometry of the problem: a sub-wavelength aperture in a PEC thin screen covered by a pair of isotropic and homogeneous SNG slabs.

As already mentioned in [59], under certain conditions, the ENG-MNG pair has several interesting properties, such as: transparency, complete tunneling and resonance. These features are enabled by the conjugate matching condition (e.g. the slabs do have the same thickness and same but oppositely signed values of permittivity and permeability), results that can be easily achieved from (2.25):

$$\begin{cases} \varepsilon_2 = -\varepsilon_1 = -\varepsilon < 0 \\ \mu_1 = -\mu_2 = -\mu < 0 \\ d_2 = d_1 \end{cases} \qquad (3.21)$$

If the conjugate matching condition (3.21) is met, a resonance is expected at the interface between the two slabs. This phenomenon has been already used to design several compact components [60], such as: resonators [61], patch and dipole antennas [62,63], etc. Here, the same physical phenomenon is used to design small covers to enhance the transmission through sub-wavelength apertures on flat metallic screens. It is worth noticing, anyway,

that the structure of Figure 26 significantly differs from the ENG-MNG pair presented in [59], due to the presence of the PEC screen.

Referring to Figure 26, the impinging wave experiences a non-standard transmission phenomenon. Here, within the aperture, despite the electrically small size, a resonance effect arises at the interface between the SNG covers and, thus, the amplitudes of Bethe's equivalent dipole moments [52], responsible for the transmission through the aperture, are much higher than without the SNG covers. The transmission, thus, is expected to be highly enhanced.

The numerical results presented in Figure 27 confirm this expectation, obtaining a *44 dB* enhancement. The simulation is performed through a time-domain numerical solver based on the finite integration technique. In this first example the cover has the same transverse extension of the screen and the structure is illuminated by a normally directed TEM wave, with the electric field directed along *x* (see Figure 26 for the reference system).

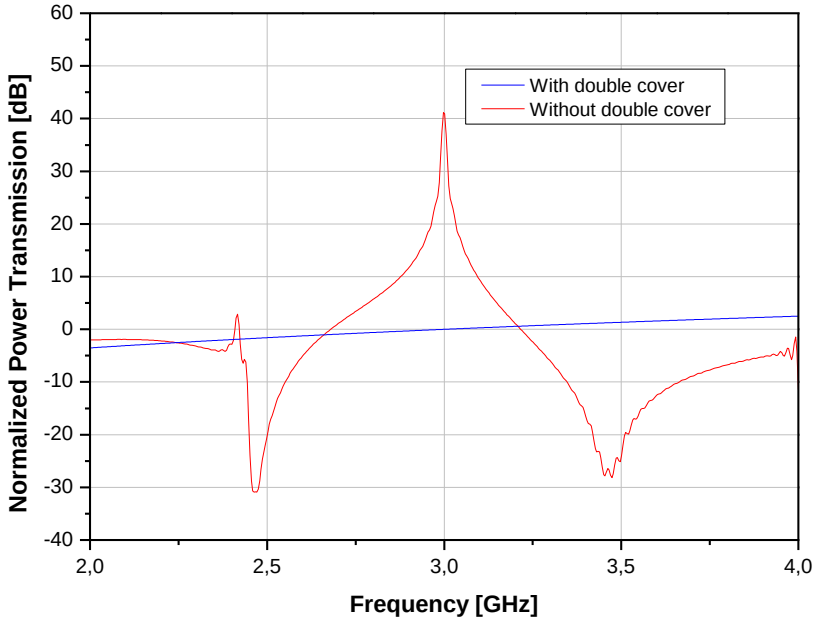

Figure 27 Comparison of the power transmission through a circular aperture with and without the double SNG cover. The impinging wave is TEM with respect to the normal of the screen. Each cover is *4 mm* thick and the transverse extension is the same as for the metallic screen (*100 x 100 mm*). The design frequency is *3 GHz* and the radius of the circular aperture is $r = 1$ *mm*. The power transmission has been normalized to the transmission value obtained without the cover at the design frequency of *3 GHz*.

The SNG covers have been assumed to be made of ideal isotropic and homogeneous materials following Lorentz's dispersion models so that, at the design frequency (fixed at *3 GHz*), the permittivities and permeabilities are: $\varepsilon_1 = \varepsilon_0$, $\mu_1 = -\mu_0$, $\varepsilon_2 = -\varepsilon_0$, $\mu_2 = \mu_0$. The thicknesses of the covers do not play a significant role, provided that they are the same for the two covers.

In Figure 28 the amplitudes of the transverse components of the electric and magnetic fields along the propagation axis at the resonant frequency are shown. The strong resonance at the interface, which is responsible for the enhanced transmission from the sub-wavelength aperture, is here clearly highlighted.

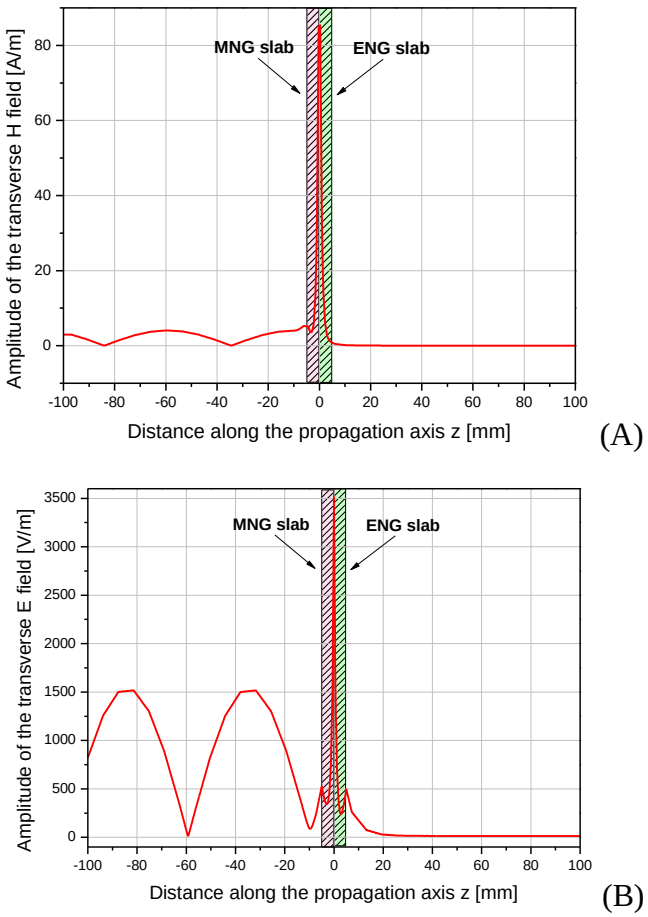

Figure 28 Amplitude of the transverse electric (a) and magnetic (b) fields along the propagation axis *z* at the resonant frequency *f = 3 GHz*. The conducting screen is placed at *z=0*. (Pictures from ref. 65)

In order to investigate the physics behind the enhanced transmission through the sub-wavelength aperture presented in Figure 26, the differences between the structure depicted in Figure 26 and the ENG-MNG pair presented in [59] are analyzed. The first difference is that the metallic screen forces the tangential electric field to vanish on the screen itself, while the tangential magnetic field has its maximum. Since the tangential electric (magnetic) field is related to the derivative of the tangential magnetic (electric) field, we have:

$$\begin{cases} \left.\dfrac{\partial H_y}{\partial z}\right|_{screen} \simeq 0 \\ \left.\dfrac{\partial E_x}{\partial z}\right|_{screen} \neq 0 \end{cases} \qquad (3.22)$$

Heuristically, even if these conditions should be met only on the metallic screen, due to the electrically small dimensions of the aperture, they are almost met in proximity of the aperture at the interface between the two SNG metamaterials. On the other hand, due to the continuity of the tangential components of the electric and magnetic fields at the interface between the two SNG materials at the aperture, the following relations must hold:

$$\begin{aligned} \left.\frac{1}{\mu_1}\frac{\partial E_x^{[1]}}{\partial z}\right|_{aperture} &= \left.\frac{1}{\mu_2}\frac{\partial E_x^{[2]}}{\partial z}\right|_{aperture} \\ \left.\frac{1}{\varepsilon_1}\frac{\partial H_y^{[1]}}{\partial z}\right|_{aperture} &= \left.\frac{1}{\varepsilon_2}\frac{\partial H_y^{[2]}}{\partial z}\right|_{aperture} \end{aligned} \qquad (3.23)$$

where the superscript 1, 2 refers to the two different materials. Considering the conditions (3.22) imposed by the presence of the metallic screen, the second equality in (3.23) is almost satisfied for any value of the permittivities of the two slabs, with the consequence that the permittivities do not play a significant role at the interface. On the other hand, the first equality in (3.23) says that the slope change of the tangential electric field (i.e. a resonance of the tangential magnetic field) can take place only if the two permeabilities of the two covers have opposite signs. Therefore, in this case, only the permeabilities play an important role in the enhancement of the transmission.

The conclusion here derived results in a dramatic simplification of the layout. The ENG slab on the exit face of the screen, in fact, can be even removed, provided that the permeability of the MNG slab at the design frequency is the opposite of the one of the vacuum.

Before investigating the properties of a single SNG cover, it is first shown that the double SNG cover does not need to be of the same transverse size of the metallic screen. Since the enhanced transmission is due to the resonance arising at the interface between the two SNG metamaterials at the aperture, we expect that even double covers with electrically small transverse dimensions would, in principle, produce a significant transmission enhancement.

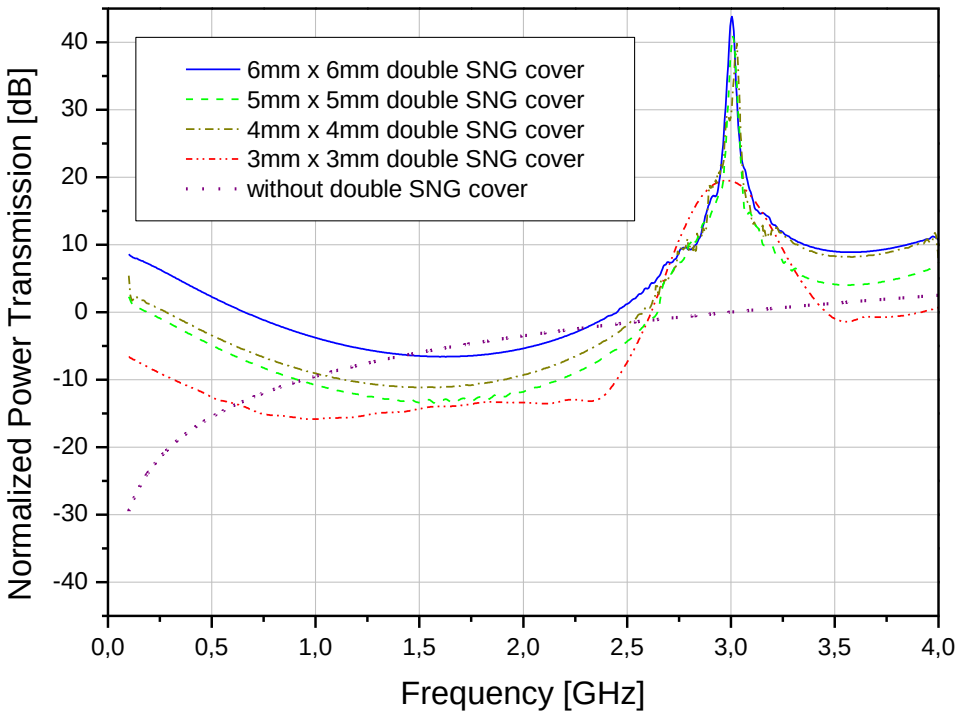

Figure 29 Normalized power transmission for different transverse extensions of the double SNG cover. The thickness of the covers is kept unchanged and equal to 4 mm. The radius of the circular aperture is r = 1 mm. The power transmission is normalized to the case without the covers at 3 GHz.

The power transmission performances deteriorate when the transverse size of the cover

approaches the aperture size. In such a case, in fact, the model here suggested is no more accurate. Anyway, still in the case of a *3 x 3 mm* screen, the resonance occurs at the design frequency, even if the performance in the power transmission is reduced compared to the case of larger covers.

3.4.3 The single MNG cover

Accordingly to the previously derived results, the design of a single MNG cover is here presented. In this case, the structure under analysis is the same as the one in Figure 26 without the ENG cover on the exit side of the aperture. The MNG slab at the entrance face has the opposite of the vacuum permeability $\mu_1 = -\mu_0$ at the design frequency.

According to the theory developed in [59], the pair ENG-MNG resonates exactly when the two materials are conjugate matched: the permeabilities and permittivities of the two slabs are oppositely signed. In the present case, instead, the conjugate matching condition is loosed. Particularly, the thicker is the MNG slab, the larger is the reflection. The single MNG cover works if the permeability of the slab at the design frequency is the same of the free space permeability with a reduced enhancement in comparison with the MNG-ENG setup due to reflection. In Figure 30, the power transmission with and without the single MNG cover, designed at *3 GHz*, is reported.

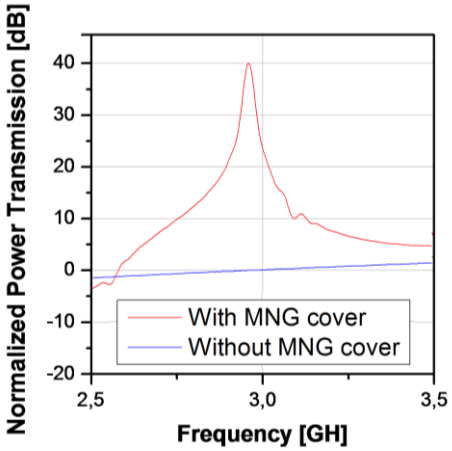

Figure 30 Power transmission comparison with and without the single MNG cover. The thickness of the cover is 4 mm and it has the same transverse extension of the metallic screen (100 x 100 mm). The hole

radius is r = 1 mm. The design frequency is f = 3 GHz. The power transmission is normalized to the case of absence of the cover at 3 GHz.

In this first example, the MNG cover has the same transverse size as the metallic screen. The transmission peak is obtained around the design frequency, while the enhancement is reduced (around *3 dB*) with respect to the previous setup. Further enhancements are obtained by reducing the thickness of the cover. Anyway, the thickness of the setup is limited by the size of the inclusions used to implement the MNG metamaterials, as it will be discussed later.

Even if the transmission enhancement of the single MNG cover is always lower than the one obtained using the double SNG cover, the former layout is easier to implement in real-life applications as only one kind of inclusion is needed.

3.4.4 Design of an inclusion-based single MNG cover layout

The main goal is now to design a metamaterial sample with the required value of the negative permeability, in accordance with the theoretical investigation previously presented. Since the inclusions are packed together in an electrically small volume, the coupling effect arising among these resonating elements cannot be neglected. In addition, the metamaterial volume itself is electrically small and, thus, homogenization may fail. For these reasons, standard models to retrieve the effective parameters of small metamaterial samples may result inaccurate [17]. Techniques based on the inversion of scattering parameters [18] have been used as a starting point to obtain the initial geometrical parameters of the inclusions, then, in order to achieve the needed value of the negative permeability, a fine tuning of the geometrical parameters through a numerical optimization has been performed.

The results here presented have been obtained by using an array of squared Split-Ring Resonators (SRRs) placed in front of the metallic screen where the sub-wavelength hole is drilled (Figure 31). The structure has been placed in a parallel plate waveguide, in such a way that the magnetic field of the TEM fundamental mode is aligned along the axis of the SRRs. The simulated results of the power transmission are reported in Figure 32.

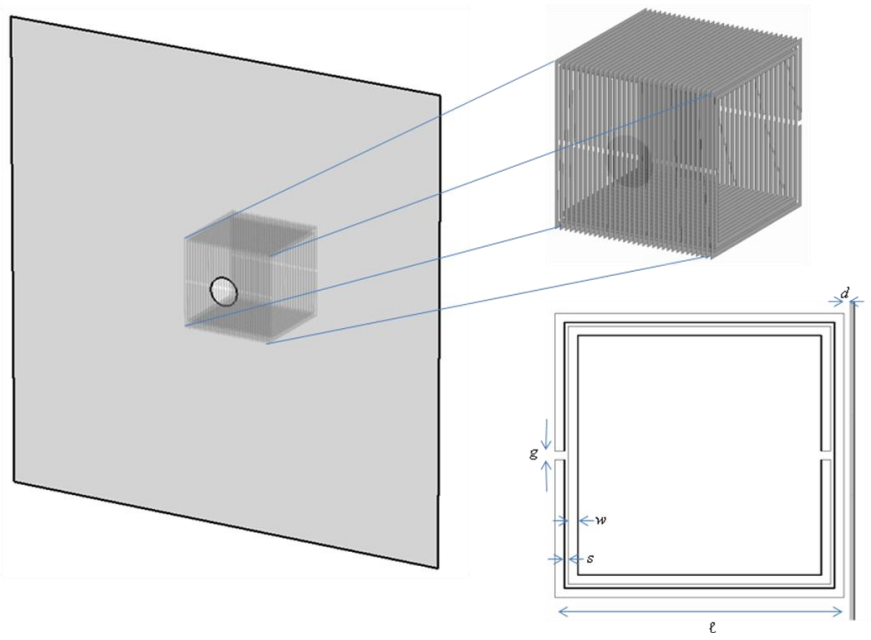

Figure 31 Single MNG cover made of a linear array of 19 squared SRRs. The SRR dimensions are the following: $\ell = 6.475$ *mm*, $w = 0.185$ *mm*, $g = 0.37$ *mm*, $s = 0.185$ *mm*, $d = 0.46$ *mm*. The separation between two adjacent SRRs is *0.37 mm*. (Pictures from ref. 65)

In Figure 33, the variation of the power transmission with the cover dimensions is shown. In addition, the increase of the power transmission when decreasing the transverse dimensions of the cover is also an expected result. The magnetic energy stored in the cover and the related losses are, in fact, reduced when the volume of the SRR cover gets smaller and smaller. Interestingly two transmission peaks arise: the one at lower frequency is due to the intrinsic resonance of the SRR inclusions, the one at higher frequency is due instead to the satisfaction of the condition $\mu_1 = -\mu_0$. Those results are in perfect agreement with the experimental result presented in [64].

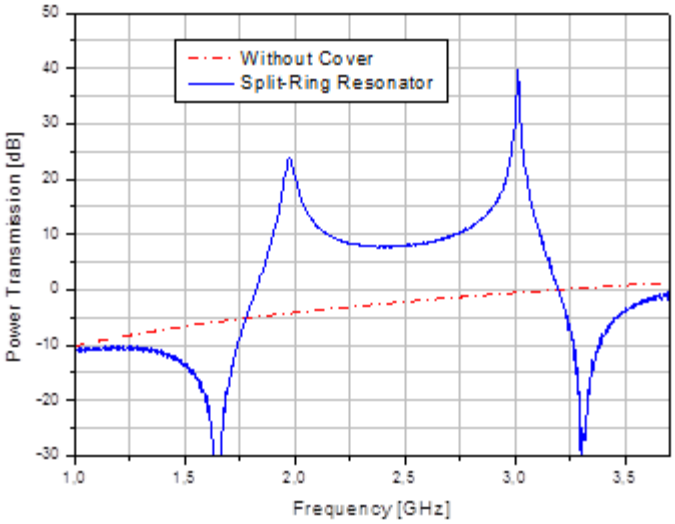

Figure 32 Power transmission comparison with and without the single MNG cover implemented through the SRR inclusions of Fig. 11. The metamaterial sample has the same extension of the metallic screen. The impinging field is a TEM wave with respect to the normal of the screen, having the magnetic field aligned along the axis of the SRRs. The hole radius is $r = 1\ mm$ and the design frequency is $f = 3\ GHz$. The power transmission is normalized to the value obtained at the design frequency without the cover.

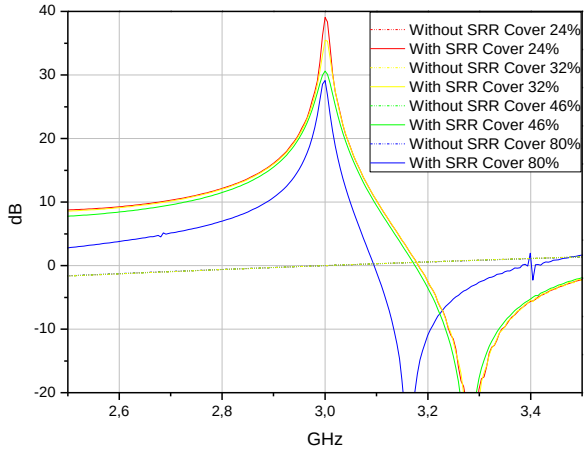

Figure 33 Power transmission comparison for different transverse dimensions of the SRR cover; the cover extension is expressed in % respect to the transverse dimension of the screen (50x50 mm). The impinging wave is TEM with respect to the normal of the screen. The hole radius is $r = 2.2\ mm$. The design frequency is $f = 3\ GHz$.

Of course, in order to design a completely functional device working for both polarizations, a tridimensional arrangement of the magnetic resonators has to be considered, in such a way that a high degree of isotropy would be, in principle, granted. The solution of this problem is beyond the scope of the present work, and will be subject of future investigations. The effect of the losses of the dielectric substrate has been also neglected and should be considered when going towards the actual fabrication of the proposed setup. Finally, the use of different magnetic inclusions is investigated. The use of more complex geometries may lead to lower resonance frequencies allowing the design of reduced size structures.

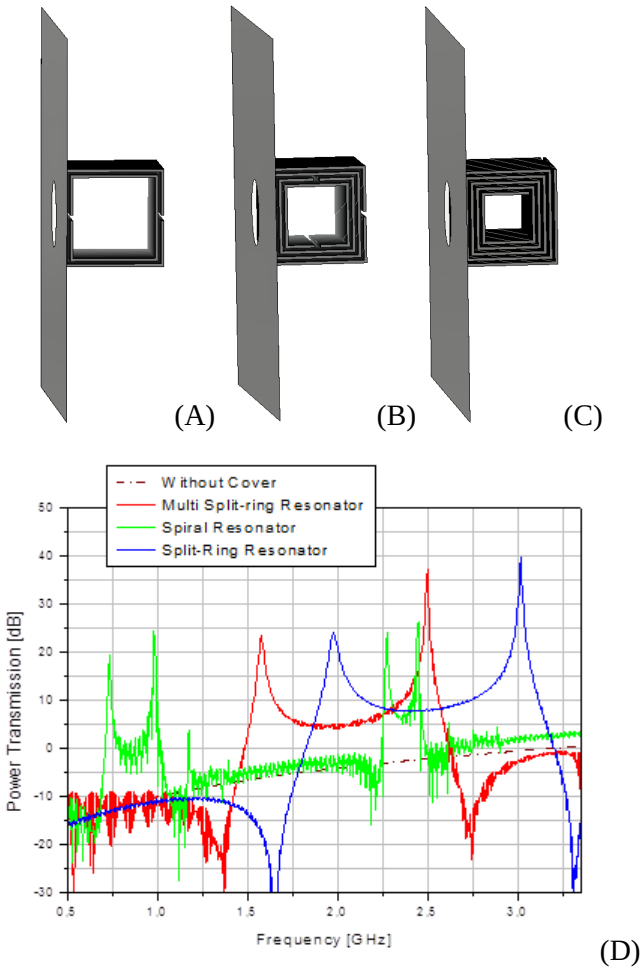

Figure 34 Single MNG cover made of Split ring resonators (A), Spiral Resonators (B) and Multi-Split-ring Resonators (B) having the same outer side size of Figure 31 and the corresponding transmission performances (D).

3.5 TRANSMISSION ENHANCEMENT, IMPEDANCE MATCHING AND MODAL CONVERSION THROUGH SINGLE RESONATING OMEGA PARTICLES,

Recently, the behavior of several layouts based on the use of small single sub-wavelength resonating inclusions have been investigated to enhance the power transmission through electrically small apertures at microwaves [64,66]. The highly localized magnetic resonance allows extremely compact designs, with an effective size of the resonator close to that of the aperture sizes. Moreover, an important advantage in terms of performances is achieved, especially if compared to other setups based on bulky structures [56-58].

Differently from [64,66] omega inclusion pairs [67,68] are used here to increase the power transmission trough a sub-wavelength aperture, taking advantage of both a strong electric and magnetic resonance excited in close proximity to the hole, enhancing thus the amplitude of the equivalent aperture dipole moments.

The experimental setup consist of a double omega inclusion inside a small hole drilled in a perfectly conducting metallic screen placed inside a rectangular waveguide (see Figure 35).

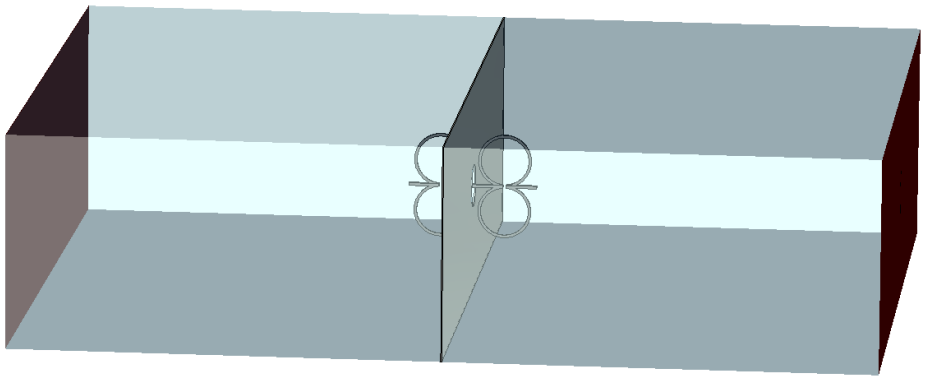

Figure 35 A double pair of coupled omega inclusion placed inside an electrically small aperture drilled in a metallic screen. The omega particles are suspended trough dielectric spacers, the rectangular. waveguide transverse size =40 mm x 120 mm, hole radius = 4 mm, omega radius = 5 mm, omega length = 12 mm.

The results achieved by exciting the fundamental TE_{10} mode, obtained through full-wave

simulations with a finite integration technique commercial solver, are depicted in Figure 36.

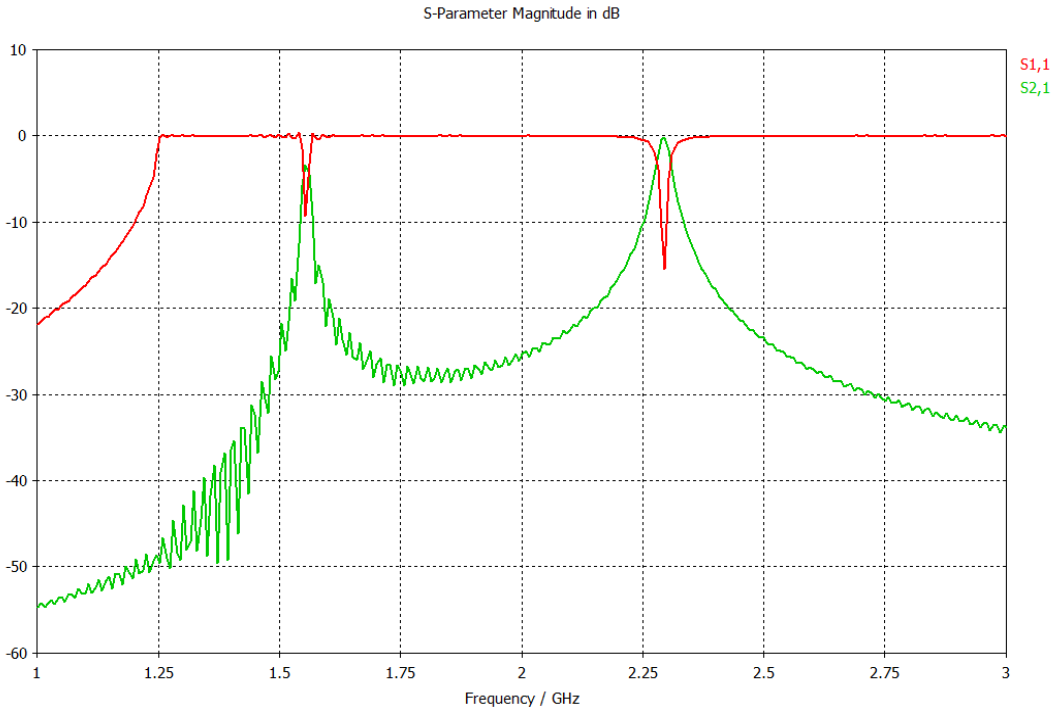

Figure 36 A Transmission and Reflection coefficient for the structure depicted in Figure 35.

Looking to the current density distribution at the transmission peak frequencies, two different resonances are found, one symmetric and one anti-symmetric, one related only to the magnetic field and the other one involving also the electric field. In the second case the field strength is significantly enhanced, leading then to a higher transmitted power level.

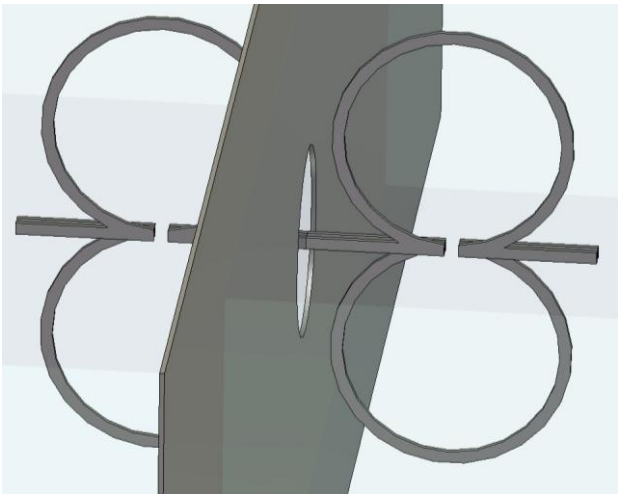

(A)

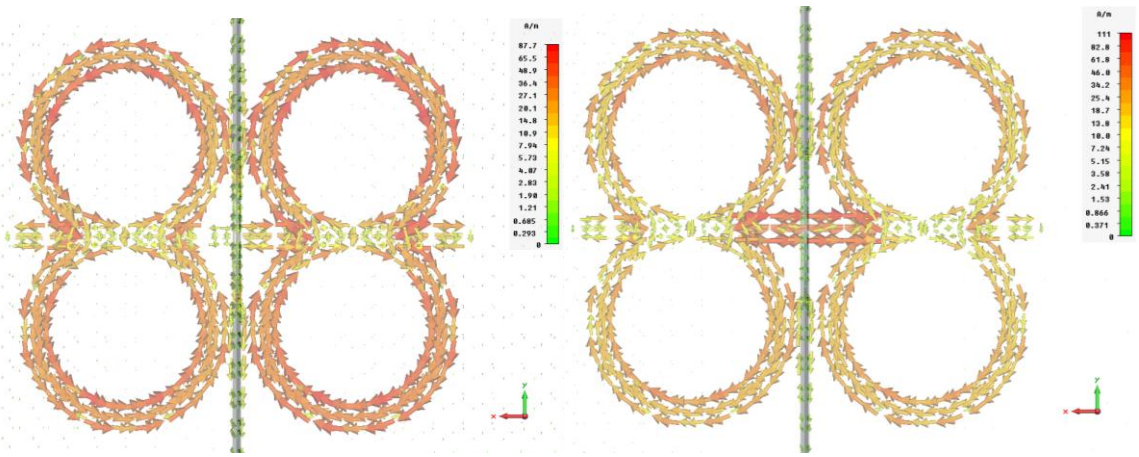

(B) (C)

Figure 37 Current density for the structure (A) at the symmetric resonance frequency involving the magnetic field only (B) and at the anti -symmetric resonance frequency involving both the magnetic and the electric fields (B) thus achieving an enhanced field strength and a higher transmitted power level.

In addition, since the behavior of omega inclusions is not affected by the impedance mismatch between the input and the output waveguide, a perfect matching can be achieved without introducing any transition device. As an immediate consequence, this resonance may be exploited to connect waveguides of different size, characteristic impedance and cross-section, leading also to the design of very compact and efficient mode converters.

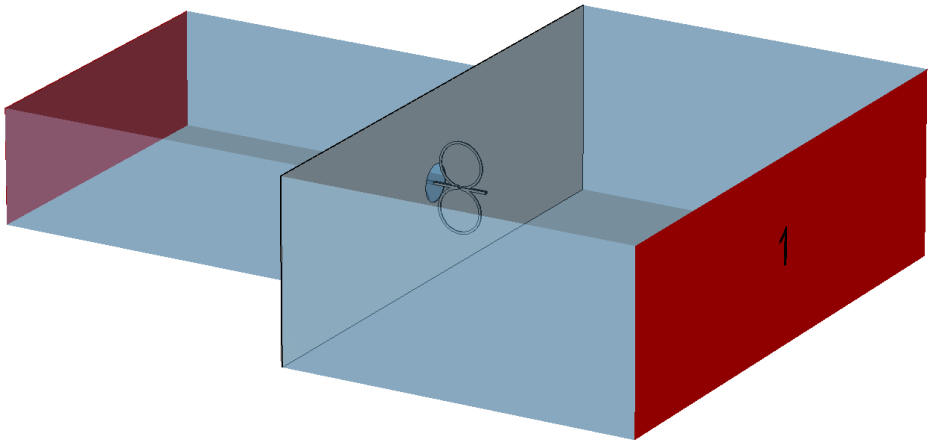

Figure 38 A double pair of coupled omega inclusion placed inside an electrically small aperture drilled in a metallic screen. The omega particles are suspended trough dielectric spacers, the rectangular. waveguide 1 transverse size = 40 mm x 120 mm, Rect. the rectangular. waveguide 2 transverse size = 25 mm x 70 mm, hole radius = 4 mm, omega radius = 5 mm, omega length = 12 mm.

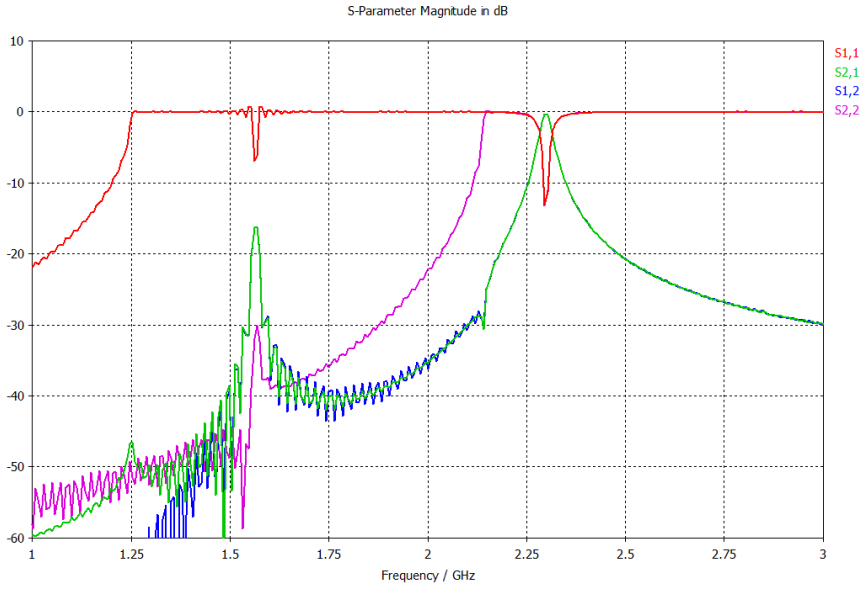

Figure 39 A Transmission and Reflection coefficient for the structure depicted in Figure 38.

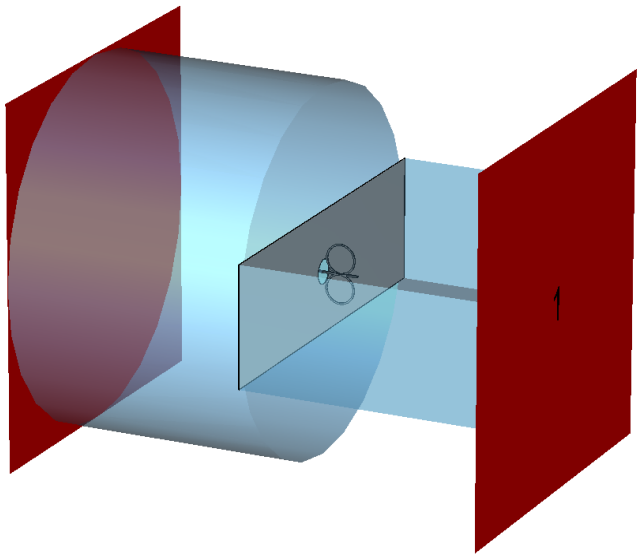

Figure 40 A double pair of coupled omega inclusion placed inside an electrically small aperture drilled in a metallic screen. The omega particles are suspended trough dielectric spacers, the rectangular. waveguide transverse size = 40 mm x 120 mm, circular waveguide 2 radius = 60 mm, hole radius = 4 mm, omega radius = 5 mm, omega length = 12 mm.

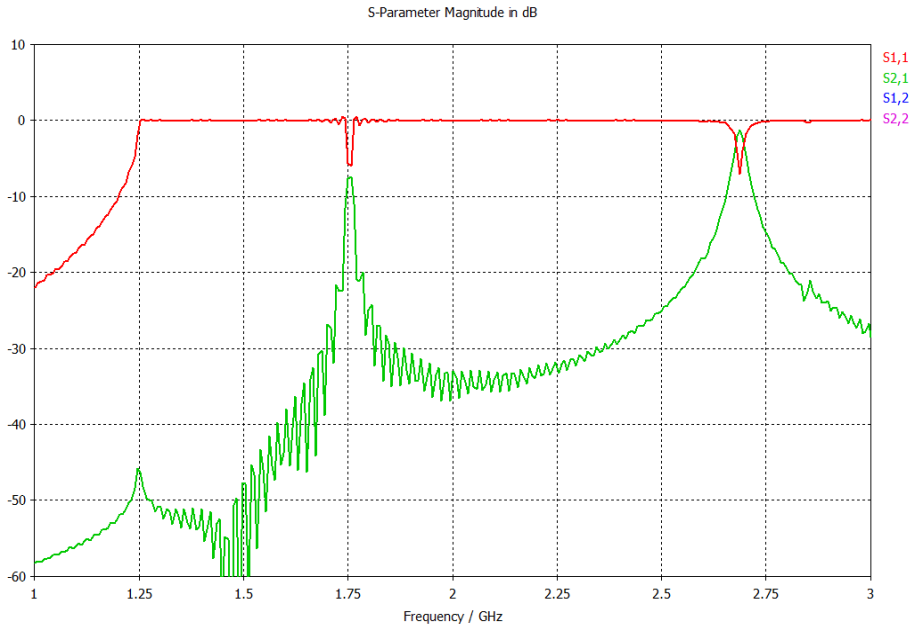

Figure 41 A Transmission and Reflection coefficient for the structure depicted in Figure 40.

In accordance with the previous analysis, the omega particles can be successfully applied to obtain an optimal transition from a guided mode to a travelling one (and vice versa). If we remove one of the waveguide, in fact, we may use as an electrically small efficient antenna radiating in free space (see Figure 42).

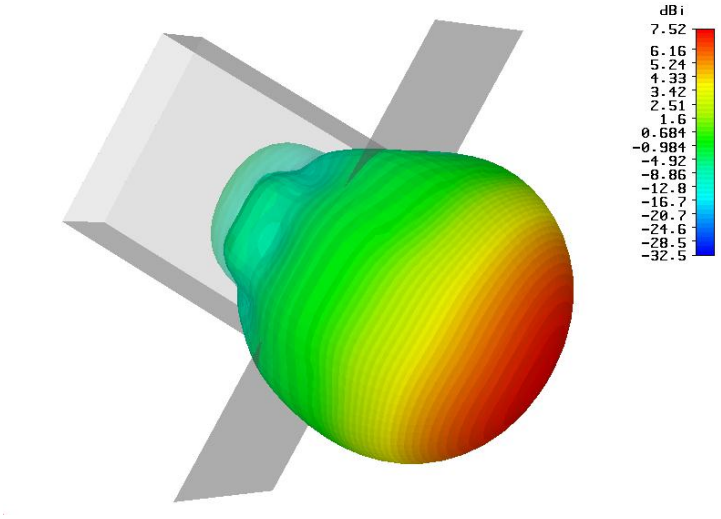

Figure 42 Radiation pattern of a pair of omega particles fed by a rectangular waveguide coupled through a small aperture.

3.6 FREQUENCY SELECTIVE SURFACES AS METAMATERIALS REPLACEMENT

According to Section 3.4 a power transmission enhancement can be achieved by exciting a resonance through properly paired SNG slabs, placed across a sub-wavelength aperture, provided that their electrical and geometrical parameters satisfy the following conditions:

$$\begin{cases} X_{ENG} = -X_{MNG} \\ \beta_{ENG} d_2 = \beta_{MNG} d_1 \end{cases} \Rightarrow \begin{cases} d_1 = d_2 \\ \varepsilon_1 = -\varepsilon_2 \\ \mu_2 = -\mu_1 \end{cases} \qquad (3.24)$$

where $X_{ENG,MNG}$ is the characteristic reactance of an SNG slab (MNG or ENG), $\beta_{ENG,MNG}$ is the corresponding propagation constant, $d_{ENG,MNG}$ is the thickness of each slab and $\varepsilon_{1,2}$ and $\mu_{1,2}$ are the electric permittivity and magnetic permeability of the slab material. In [70] it has been shown that pairing a stack of purely capacitive FSS (i.e. a planar disk medium) with a purely inductive stack of FSSs (i.e. a circular perforated metallic plate) [69] results in the same transparency, tunneling and resonance phenomena shown in [59] in the case of bulk metamaterials. By deriving the Block impedance for both the capacitive and the inductive stacks of FSSs and requiring the structure to be transparent, the following conditions, formally equivalent to (3.24), are derived:

$$\begin{cases} Z_{FSS1} = -Z_{FSS2} \\ \gamma_{FSS1}\, d_1 = \gamma_{FSS2}\, d_2 \end{cases} \text{ or } \begin{cases} Z_{FSS1} = Z_{FSS2} \\ \gamma_{FSS1}\, d_1 = -\gamma_{FSS2}\, d_2 \end{cases} \qquad (3.25)$$

where γ is the Bloch wave-number and Z is the Bloch impedance of each plate. Heuristically, it is possible to excite a "compact resonance" at the hole plane, just pairing together dually shaped FSS screens. In Figure 42 the proposed layout and the corresponding results in terms of power transmission are presented.

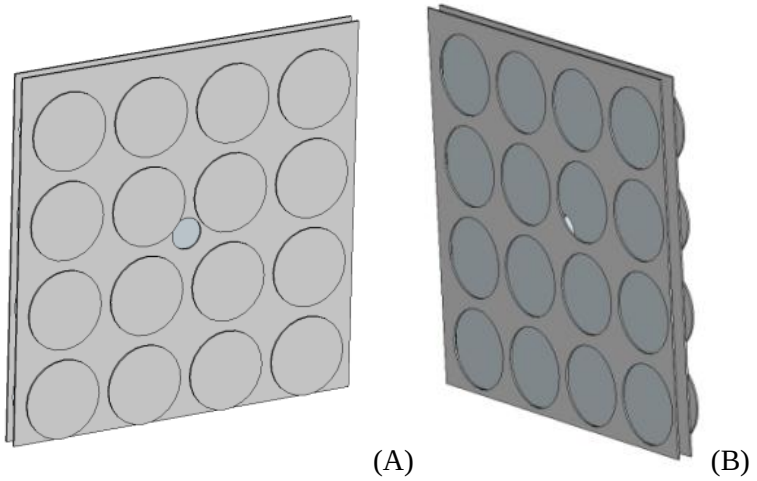

Figure 43 Layout involving FSSs: one FSS exhibits a capacitive behavior (A), the other one exhibits an inductive behavior (B).

However, as it has been previously pointed out in the case of the MNG metamaterial based setup [71], it can be easily shown that also in this case a single kind of FSS is needed. The structure presented in Figure 42, in fact, can be easily modeled through the transmission line equivalent circuit representation depicted in Figure 44.

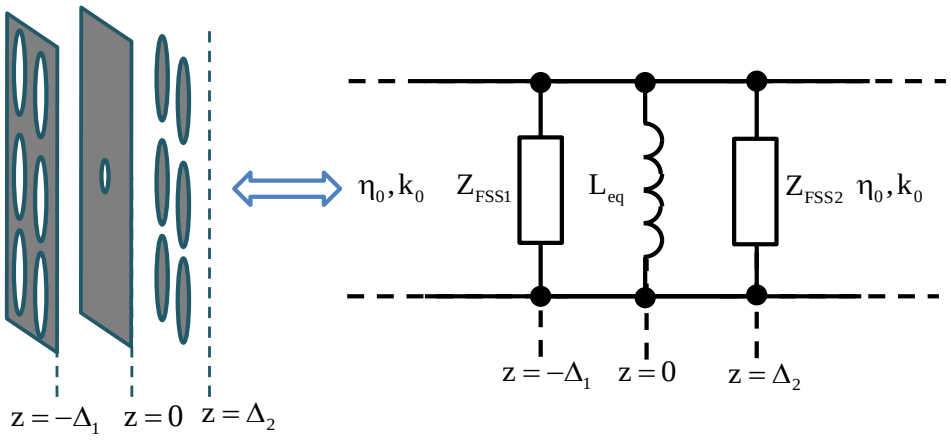

Figure 44 Equivalent circuit representation of the proposed setup.

The hole is represented through its equivalent shunt inductance. The evaluation of this

quantity is not a straightforward task: apart from the hole shape, it depends on both the polarization of the impinging field and the transverse size of the screen (the calculations are generally done for bounded structures, i.e. waveguides see [72]). However, assuming the metallic screen transverse size much larger than the aperture surface and the hole diameter much smaller than the wavelength of the impinging field, the inductive term L_{eq} becomes negligible and the equivalent circuit in Figure 42 collapses into the one presented in Figure 45.

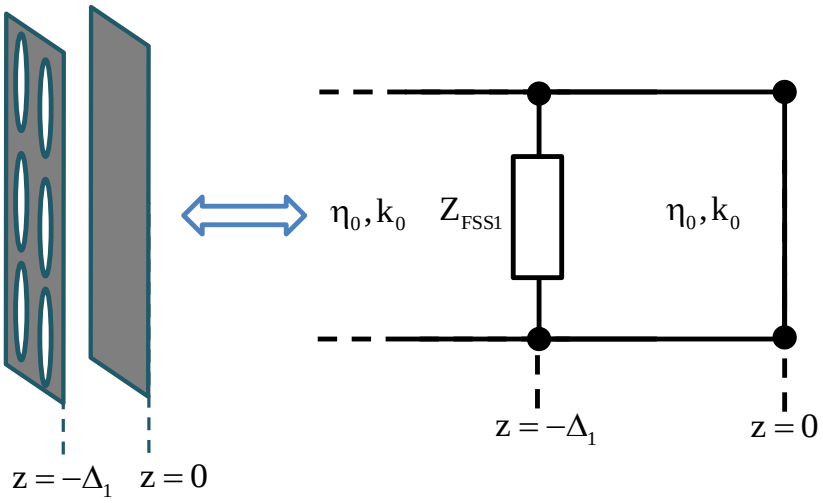

Figure 45 Equivalent circuit representation of the proposed setup.

Considering a monochromatic TE(z) plane wave excitation (the TM case can be easily obtained by duality) in the form:

$$\begin{cases} \mathbf{E}^{TE} = \hat{x} A_0 \left(e^{-jk_{z0}(z+\Delta_1)} + R e^{jk_{z0}(z+\Delta_1)} \right) e^{-jk_y y} \\ \mathbf{H}^{TE} = \dfrac{j}{\omega \mu_0} \nabla \times \mathbf{E}^{TE} \end{cases} \tag{3.26}$$

where μ_0 and ε_0 are the magnetic permeability and the electric permittivity in free space, respectively, $k_y = \sin(\theta)\omega\sqrt{\varepsilon_0\mu_0}$ and $k_{z0} = \sqrt{\omega^2\varepsilon_0\mu_0 - k_y^2}$. The transverse magnetic field on the PEC screen is, then:

$$\mathbf{H}_y^{TE}\Big|_{z=0} = \hat{y} \frac{2A_0 e^{-jk_y y} k_{z0}^2 Z_{FSS}}{\mu_0\omega\left[k_{z0} Z_{FSS}\cos(\Delta_1 k_{z0}) + j(k_{z0} Z_{FSS} - \mu_0\omega)\sin(\Delta_1 k_{z0})\right]} \tag{3.27}$$

Requiring the denominator of the tangential magnetic field amplitude to vanish on the PEC screen, under the assumption that the spacing between the FSS and the hole plane is small compared to the impinging wavelength ($\Delta_1 k_{z0} \ll 1$), a simple design formula for the equivalent shunt impedance of the FSS screen is derived:

$$Z_{FSS}^{TE} = \frac{\Delta_1 \left(j + \Delta_1 k_{z0} \right) \mu_0 \omega}{1 + \Delta_1^2 k_{z0}^2} \qquad (3.28)$$

Following a similar approach, in the case of an incident TM(z) plane wave, imposing that the denominator of both the tangential magnetic and normal electric field components vanish on the PEC screen, it is straightforward to obtain the following formula:

$$Z_{FSS}^{TM} = \frac{\Delta_1 \left(j + \Delta_1 k_{z0} \right) k_{z0}^2}{\varepsilon_0 \omega} \qquad (3.29)$$

By simple inspection of (3.28) and (3.29), the immediate consequence of the assumptions $\Delta_1 k_{z0} \ll 1$ and $L_{eq} \to 0$ are $\mathrm{Re}\{ Z_{FSS}^{TX} \} > 0$ and $\mathrm{Im}\{ Z_{FSS}^{TX} \} > 0 \ \forall \omega > 0$ assuming $k_{z0} > 0$. The aforementioned result implies two important consequences: on one hand, the structure needed to enhance the equivalent dipole moments of the aperture is a purely passive structure, as $Re\{ Z_{FSS}^{TX} \} > 0$; on the other hand, the same structure is also required to exhibit an inductive behavior as $Im\{ Z_{FSS}^{TX} \} > 0$. Moreover, due to the intrinsic symmetry of the network representation shown in Fig. 5, it is also expected that, pairing a second identical FSS on the exit face, the transmission enhancement would result squared.

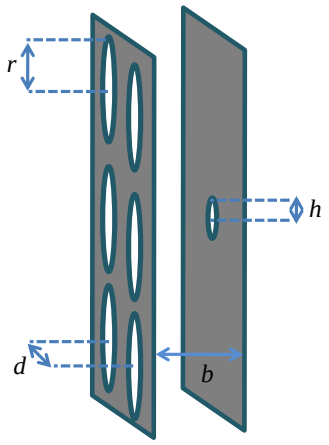

Figure 46 FSS based layout. Each circular aperture has radius r = 1.64 mm, the distance center-to-center between two consecutive elements in both transverse directions is d = 3.68 mm, the screen is placed at a distance b = 1 mm from the metallic plane of the hole. The hole radius is h = 0.3 mm = $\lambda_0/54$.

The choice of the proper FSS shape is, then, related to the analytical form of Z_{FSS}. In the present case, a screen with an almost inductive behavior at the design frequency is required. Unlike the metamaterial-based setup, the FSS based setup is not polarization independent and, consequently, inclusions with a rotational symmetry have to be preferred. In the case of a TEM(z) plane wave impinging on the screen, in order to make the layout as much robust as possible to small variations of the angle of incidence, a circular hole perforated metallic screen is chosen as the reference design. In Figure 47 the transmission performance of the inductive FSS is shown, in comparison with the case of absence of the cover.

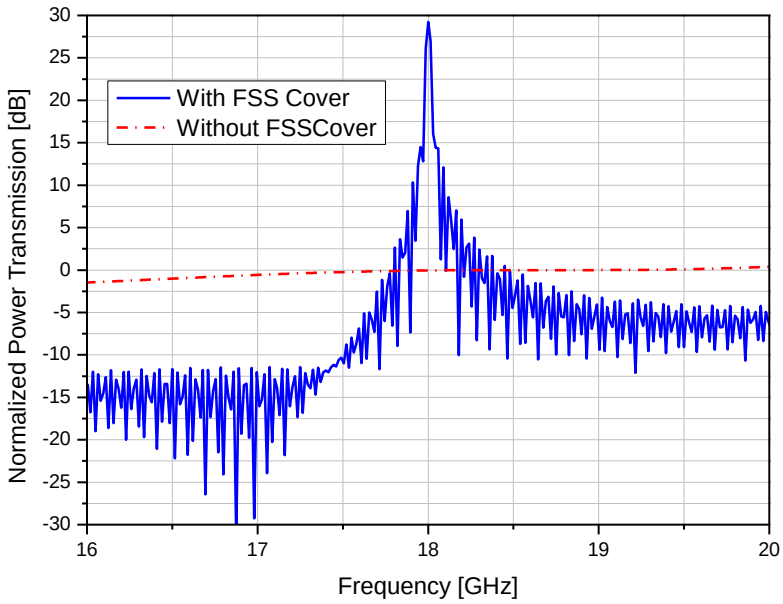

Figure 47 Power transmission with and without the FSS inductive cover. The geometrical parameters of the reference layout are the same of Fig.6. A gain of 28 dB is obtained at a frequency f=18 GHz.

The value of the equivalent shunt susceptance of the disk medium and its dual counterpart, the circular hole medium, may be evaluated through a transmission line approach. In order to properly describe the reflection and transmission properties of the structures shown from Figure 43 to Figure 46, the classic Lorentz theory, usually applied to the study of artificial media, cannot be used in this case. Lorentz theory, in fact, takes into account only the dipole term in the induced field, under the assumption that the inclusion size is small compared to their spacing and to the wavelength of the impinging field. In the proposed setup, the inclusions are, instead, comparable to the wavelength and placed very close to each other, so that the polarizing field may not be considered locally constant and the contribution of the radiated field from the disk may not be neglected in the evaluation of the interaction field. An accurate evaluation of the shunt susceptance may be given through an higher order approximation of the dipole moments for a circular disk, leading to the following accurate expressions for the electric and magnetic polarizabilities [73]:

$$\begin{cases} \alpha_m = \dfrac{8}{3} r^3 \left[1 - \dfrac{(k_0 r)^2}{10} \left(2 + \sin^2 \theta_i \right) \right] \\ \alpha_e = \dfrac{16}{3} r^3 \left[1 + \dfrac{(k_0 r)^2}{15} \left(8 - \dfrac{3}{2} \sin^2 \theta_i \right) \right] \end{cases} \qquad (3.30)$$

together with the evaluation of the dynamic interaction fields [74], which takes into account the mutual coupling among the elements. The final result for the equivalent shunt capacitance of a single layer of circular disks is, then, obtained equating the reflection coefficient due to a shunt susceptance placed in an uniform and lossless transmission line with characteristic impedance Z_0 (R_A) to the ratio between the incident and the reflected field by a planar array of thin disks (R_B, see [75]):

$$\begin{cases} R_A = \dfrac{\dfrac{1}{\dfrac{1}{Z_0} + jB(\omega)} - Z_0}{\dfrac{1}{\dfrac{1}{Z_0} + jB(\omega)} - Z_0} \\ R_B = \dfrac{-\omega \mu_0}{\beta_0 a b} \left(j\,\omega P + j\,\omega h M \right) \end{cases} \qquad (3.31)$$

where *a*, *b* are the x and y spacing between the centers of two consecutive disks, $h = k_0 \sin(\theta_i)$, $\beta_0 = \sqrt{k_0^2 - h^2}$, $B(\omega)$ is the shunt susceptance of the array of disks, Z_0 is the free space characteristic impedance, P_y and M_z are the electric and magnetic dipole moments of a circular disk along the y and z axes, respectively, evaluated through the use of the dynamic interaction constants in the forms:

$$\begin{cases} P_y = \dfrac{\alpha_e \varepsilon_0 A_0}{1 - \alpha_e C_{ee}} \\ M_z = -\dfrac{\alpha_m \dfrac{h}{\omega \mu_0} A_0}{1 - \alpha_e C_{ee}} \end{cases} \qquad (3.32)$$

C_{ee} and C_{mm} are the electric and magnetic interaction constant (see [73], in this case the coupled term C_{me} and C_{em} have not been considered, since they are negligible in practice).

The equivalent shunt susceptance of a circular perforated metallic plate can be obtained by duality.

However, this approach leads to a closed analytical expression for the equivalent shunt susceptance of a planar array of PEC inclusions (or apertures in a metallic plate) only for extremely simple geometries. In order to take into account the effect of a finite conductivity and an arbitrary shape of the inclusions, the following numerical approach can be used: a coarse reference layout designed according to the formulas in [75], is initially simulated in a parallel plate waveguide; the scattering parameters of the structure are, then, retrieved and inverted in order to obtain $Z_{FSS}(\omega)$; a genetic-algorithm optimization leading to the geometrical parameters needed to achieve the desired superficial impedance value at the design frequency is, finally, implemented. A different setup, using a squared complex geometry is provided as an example:

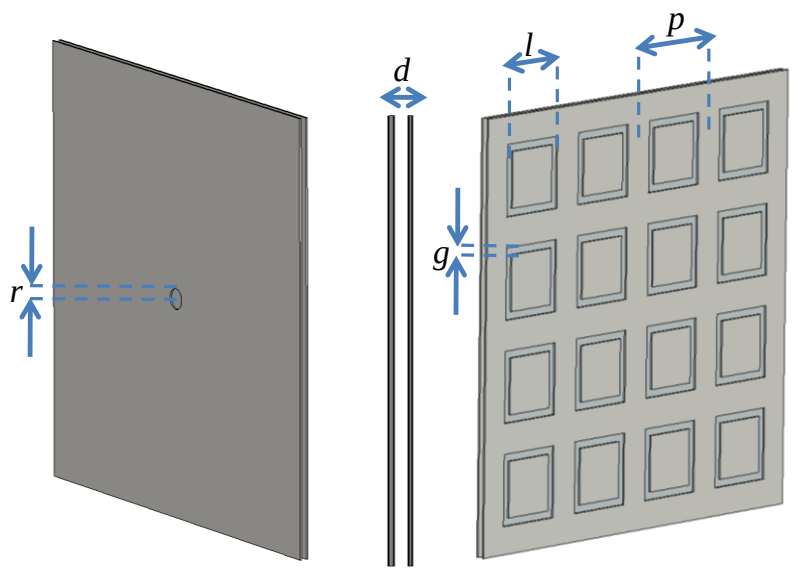

(A)

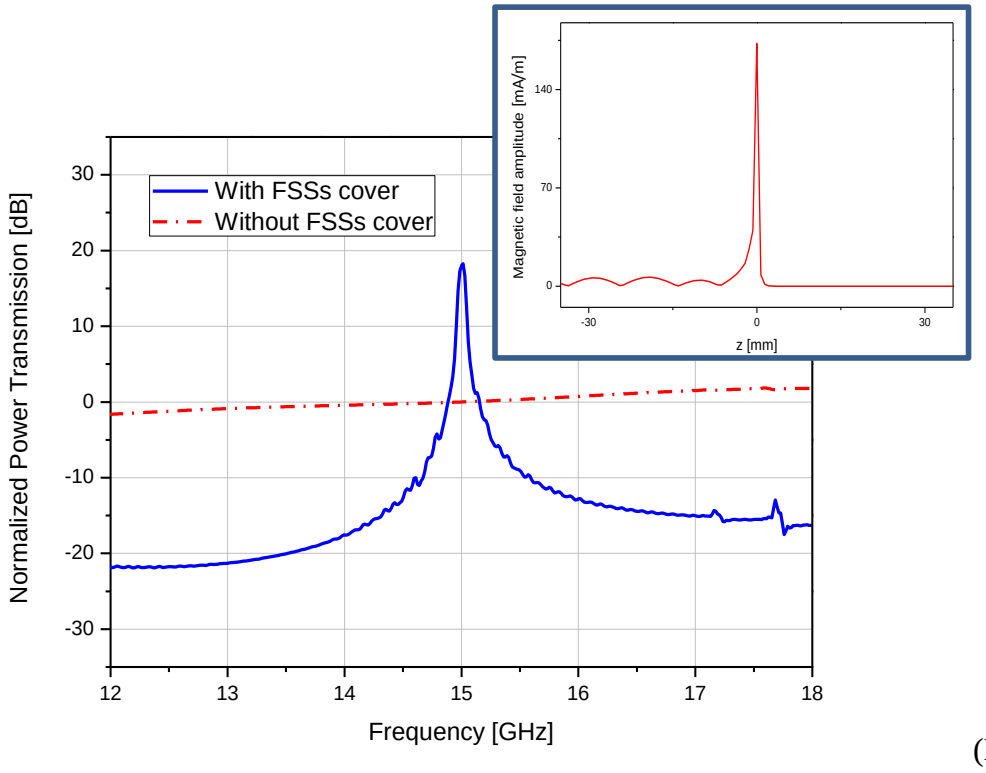

Figure 48 (A) FSS-based layout. The squared-unit-cell FSS sheet has transverse dimensions *17 mm x 17 mm*. The thickness of the copper metallization is $t = 0.07$ *mm*. The distance FSS-screen is $d = 0.25$ *mm*. The center-center distance between two inner elements for both x and y directions is $p = 4$ *mm*. The radius of the hole is $r = 0.4$ *mm*. The inner gap $g = 0.4$ *mm*. The element side $l = 2.9$ *mm*. (B) Power transmission enhancement for the structure depicted in (A) normalized to the case of absence of the FSS structure at the design frequency. (B, up inset) Amplitude of the tangential magnetic field along the normal axis to the hole at *15 GHz* in the case of a TEM(z) impinging wave. The hole plane is placed at $z = 0$ *mm*. The magnetic field amplitude in $z = 0$ *mm* without the FSS cover is *5 mA/m*. (Pictures from ref. 76)

As it has previously mentioned, the use of a second inductive FSS on the exit face of the PEC screen would result in a significant increase of the power transmission [56]. In this case a split in the resonance peak is also expected, due to the coupling of the two equivalent identical circuits.

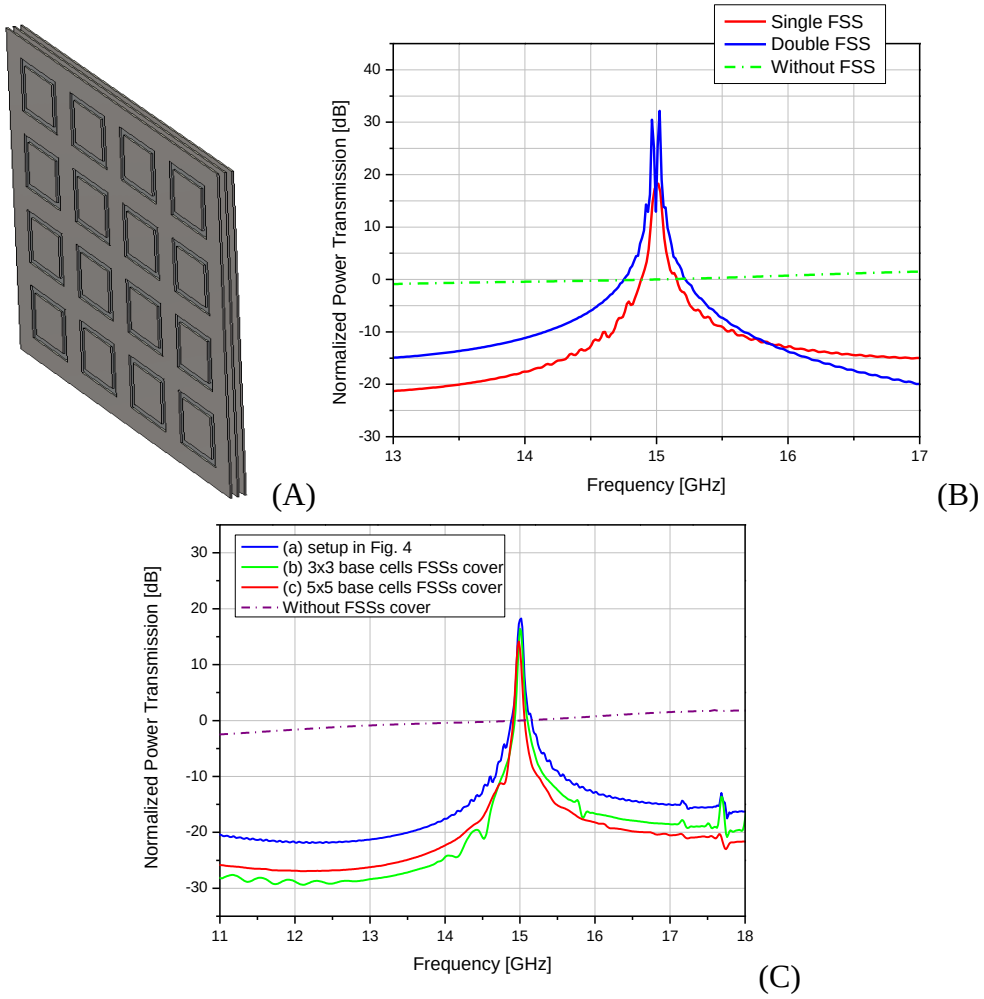

Figure 49 Geometrical sketch of the symmetrical structure consisting of two identical FSS sheets placed at both sides of the perforated metallic screen. (B) Comparison between the power transmission enhancement of the structure depicted in Figure 48 (A) and the one in (A). (C) Power transmission enhancement for the structure depicted in Figure 48 (A) and for similar structures with the same base element, periodicity, hole dimensions but different transverse extensions of the metallic screen that are nine times (b) and twenty-five times (c) bigger than the reference case (A) of Figure 48 (B), respectively. (Pictures from ref. 76)

Finally, the effect of using multiple FSS sheets, placed on one side of the screen only, is shown. We consider, for instance, the case of two FSS sheets, placed at a distance d_1 and d_1+d_2 from the metallic plate where the hole is placed. The equivalent TL model for this structure is depicted in Figure 50.

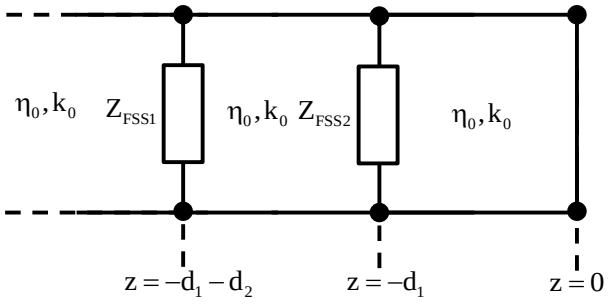

Figure 50 TL circuit representation of a setup based on a pair of FSSs placed on the left side of the screen. Each FSS sheet is modeled through its surface impedance and the contribution of the hole is again neglected, due to its sub-wavelength dimensions.

Assuming a TE(z) polarized electromagnetic field propagating through the structure (the TM case can be obtained again by duality) and both d_1 and d_2 electrically small, by imposing the denominator of the magnetic field amplitude to vanish at $z = 0$, a solution for Z_{FSS1} is found as:

$$Z_{FSS1}^{TE} = -jk_0 Z_0 \, Z_{FSS2}^{TE} \frac{(d_1 + d_2)(j + 2k_z d_2)}{Z_{FSS2}^{TE}(2k_z d_1 - j) + Z_0 k_0 d_1}, \qquad \begin{cases} k_z d_1 \ll 1 \\ k_z d_2 \ll 1 \end{cases} \tag{3.33}$$

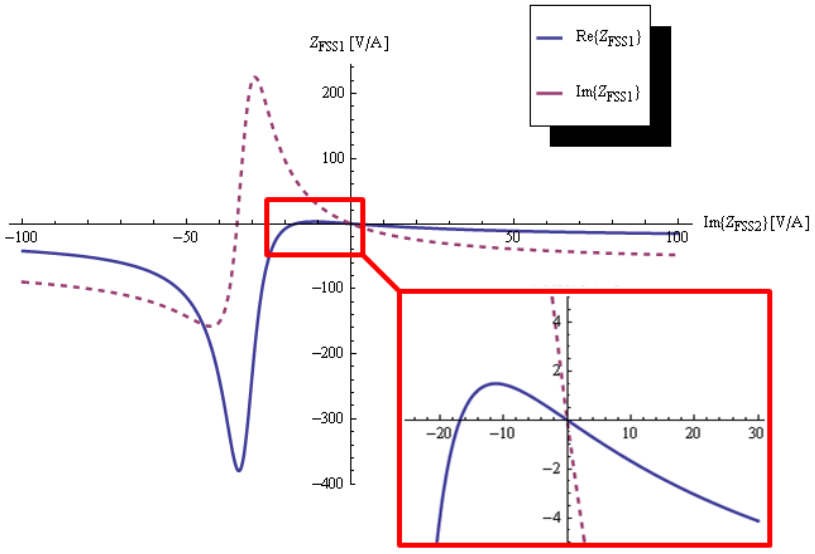

Figure 51 Real and imaginary parts of Z_{FSS1}^{TE} t as a function of the imaginary part of Z_{FSS2}^{TE} under the assumptions (3.33). The distances are $d_1 = d_2 = 0.25$ mm and the design frequency is 15 GHz. (Pictures from ref. 76)

If the following two additional conditions are introduced:

$$\mathrm{Re}\{Z_{FSS2}^{TE}\} = 0 \quad , \quad d_1 = d_2 \qquad (3.34)$$

without any loss in generality, the imaginary and real parts of Z_{FSS1} can be, then, evaluated as a function of the imaginary part of Z_{FSS2}. The final result is that, if the distances of the FSS sheets from the metallic plate are electrically small, it is possible to obtain two simple solutions, one purely capacitive, the other purely inductive:

$$Z_{FSS2}^{TE} = -\frac{1}{2}\, j\, k_0 d\, Z_0 \quad , \quad Z_{FSS1}^{TE} = 2\, j\, k_0 d\, Z_0 \qquad (3.35)$$

This configuration exhibits, in principle, better angular performance and tolerance to a mismatch of the real part of the surface impedance compared to the one in which a single capacitive FSS is used (k_z does not appear in the solution, after a first order expansion of the exact solutions, and both $Re\{Z_{FSS2}\}$ and $Re\{Z_{FSS1}\}$ vanish identically). These simple considerations open the door to more complex layouts, which can even improve the performance of the setups previously proposed. The design and the numerical characterization of such structures will be the subject of a future publication.

3.7 MAGNETISM AT THZ SCALE AND APPLICATIONS

Unfortunately, the approach illustrated in Sections 3.4-3.6 cannot be straightforwardly extended at the near-infrared (NIR) and visible frequencies, where the PTE finds a lot of interesting applications. If Maxwell's equations scale with the frequency, in fact, material properties do not and, thus, a saturation of the operation frequency of metallic resonating inclusions is expected, due to the electron kinetic inductance [77-80].

3.7.1 Plasmonic nano-pillar couples

A different magnetic inclusion, which can be successfully used to the purpose of exciting a magnetic resonance, has been recently proposed in [81] and consists of a gold pillar pair. The anti-symmetric resonance of this inclusion is able to generate a strong magnetic dipole moment when illuminated by a TM (with respect to the pillar axis) polarized field. The idea is, then, to design a pair of plasmonic pillars exhibiting an anti-symmetric resonance at a fixed frequency and place this magnetic inclusion across or close to the Electrically Small Aperture (ESA) drilled in a screen. This way, the amplitude of the equivalent magnetic dipole moment tangential to the screen would be enhanced, in the same manner as in the SRR case demonstrated in [65].

In order to reduce the effect of the material absorption inside the circular aperture, the screen has to be as thin as possible, though compatible with actual fabrication techniques. For this purpose, a silver layer with $h_d = 50\ \text{nm}$ thickness is considered. Also the pillar pair is made of silver, which is modeled through the experiment-based Drude model adopted in [82,19]:

$$\varepsilon_{Au} = \varepsilon_\infty - \frac{\omega_p^2}{[\omega^2 - i\nu_c\omega]} \qquad (3.36)$$

where $\nu_c = 9\ 10^{12}$ Hz, $\omega_p = 2\,\pi\,2\ 10^{15}$ rad/sec and $\varepsilon_\infty = 1$. The geometrical sketch of the proposed setup to obtain the Power Transmission Enhancement (PTE) is reported in Figure 52. The perforated silver screen is supposed to be deposited on a glass substrate, with

thickness $h_g = 10$ nm. On the other side of the glass substrate, which is the entrance face for the radiation, we put a pillar pair with the following dimensions $h = 90$ nm, $r_b = 90$ nm, $d = 225$ nm. At the expected resonance frequency $f_0 \simeq 300$ THz of the pillar pair in the anti-symmetric mode, the operating wavelength is $\lambda_0 \simeq 1\,\mu$m, and, thus, the hole radius $r_h = 25$ nm is reasonably sub-wavelength ($\simeq \lambda_0 / 40$).

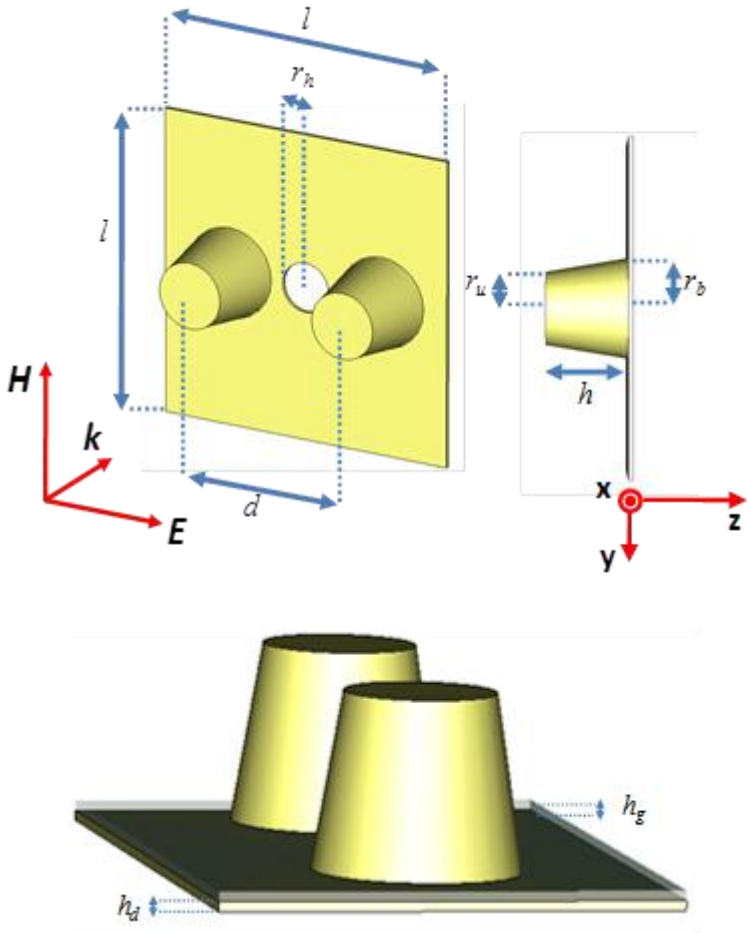

Figure 52 Geometrical sketch of the proposed setup. (Pictures from ref. 83)

The electromagnetic behavior of the structure proposed in has been simulated through full-wave simulations. The excitation is represented by a TM plane-wave having the magnetic field vector normal to the axes of the pillars and impinging on the screen from the pillar

side. The strong resonance due to the excitation of the anti-symmetric mode of the pillars at the ESA plane leads to a significant enhancement of the tangential magnetic field on the aperture.

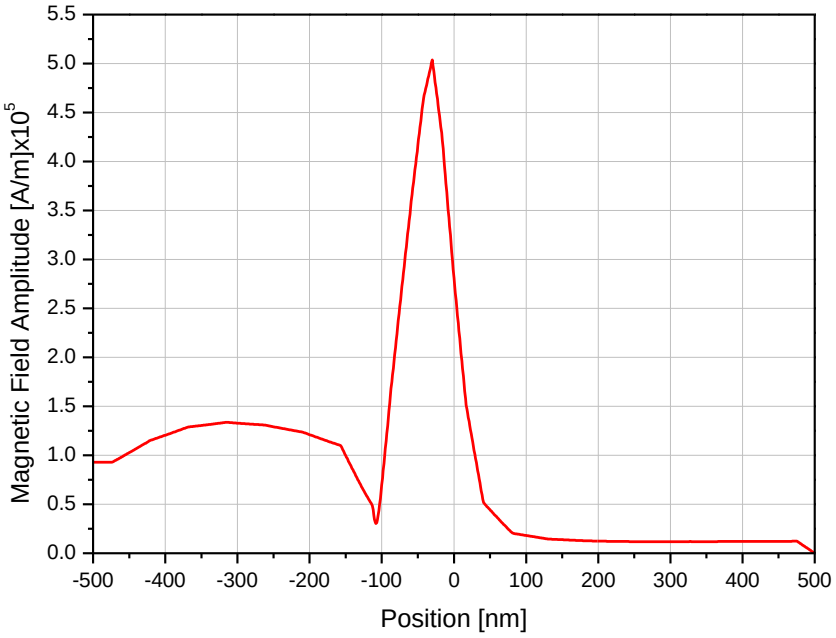

Figure 53 Magnetic field amplitude along the axis of the circular aperture (placed at z = 0). The pillar pair is in the negative region. (Pictures from ref. 83)

The power transmission curve reported in Figure 54 shows that the PTE is obtained exactly at the resonance frequency of the pillar pair ($f_0 = 300\ THz$) and it is 2.5 times larger than in the case of absence of the pillar pair for a screen transverse size of *700 nm* x *700 nm*. The transmission peak can be tuned by a proper choice of the pillar dimensions or introducing a dielectric layer between the screen and the pillars. A dynamic tunability may be predicted by using thin layers of liquid crystals, as already shown for other metamaterial setups [99].

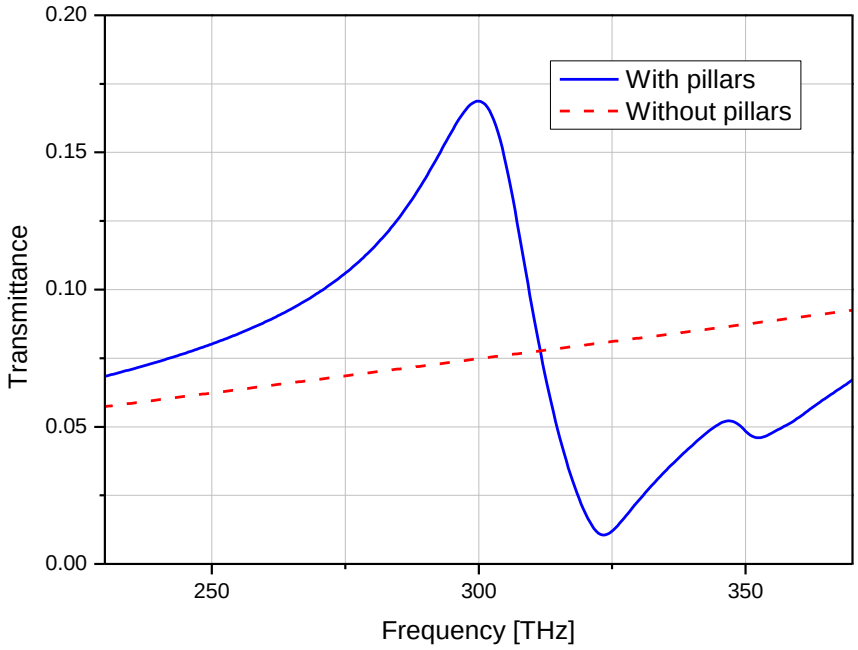

Figure 54 Transmittance for TM illumination of a 700 nm x 700 nm screen. The residual transmittance in the case without the pillars is due to the low conductivity of silver at the considered frequencies. (Pictures from ref. 83)

In order to ensure that the transmission peak is only due to the excitation of the pillar pair, the simulation method has been carefully tested. The numerical simulations, in fact, have been conducted inside an ideal waveguide made of two opposite perfect electric and two opposite perfect magnetic walls. In this way, the TEM mode propagating in the waveguide resembles a normal impinging plane wave on the structure and reflection and transmission can be easily evaluated through the scattering parameters. However, when ideal boundaries are forced in the simulation system, one should test that the expected results in terms of PTE are not due to the artificially introduced periodicity. Therefore, the same structure has been simulated varying its transverse dimensions to check that the numerical results are consistent with the model and with the expectations. The corresponding results are shown in Figure 55.

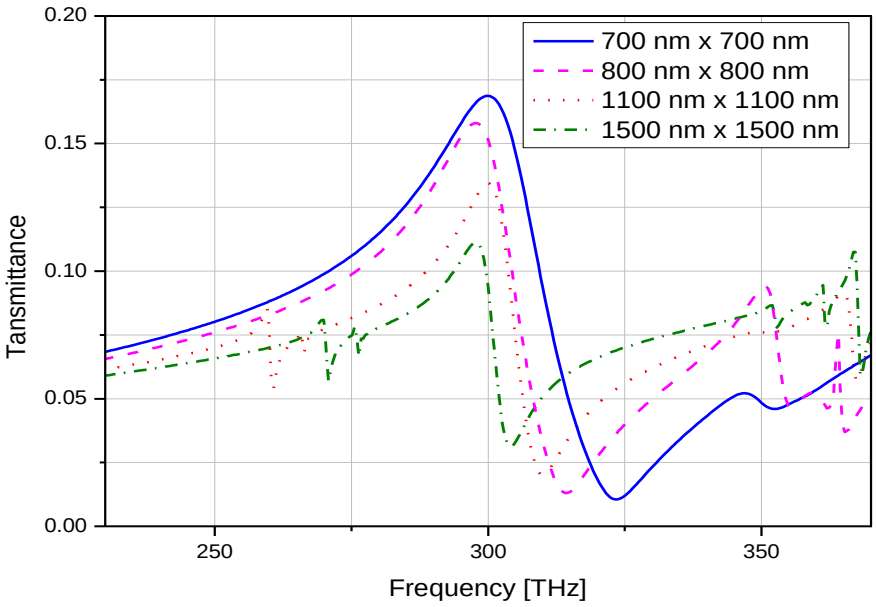

Figure 55 Transmittance for TM illumination varying the transverse screen dimensions. The transmission peak alignment confirms the independence of the resonance from the artificial periodicity due to the perfect electric and magnetic boundaries introduced in the simulation. (Pictures from ref. 83)

When varying the transverse dimensions of the structure, all the transmission peaks stick around the resonant frequency of the pillar pair ($f_0 = 300$ THz), confirming that the PTE is not due to the property of the fictitious array of apertures but only to the single aperture surrounded by the pillar pair.

Finally, it is also expected that, by reciprocity, when placing another resonant pair of pillars on the exit face of the screen, the transmittance increases approximately by a factor of four [56]. This hypothesis has also been verified through our numerical simulations and the results are presented in Figure 56 (solid line), where the transmittance is around 10 times higher than in the case without the two pillar pairs. In addition, the second pillar pair introduce a new resonance which couples with the one of the first pair. In the proposed design the two resonances have been brought together in order to obtain a broader bandwidth. In order to test the sensitivity of the design versus possible variations of the dimensions due to fabrication tolerances, in Figure 56 we report the transmittance for different values of the upper base radius of the silver pillars. These results confirm the

robustness of the proposed design.

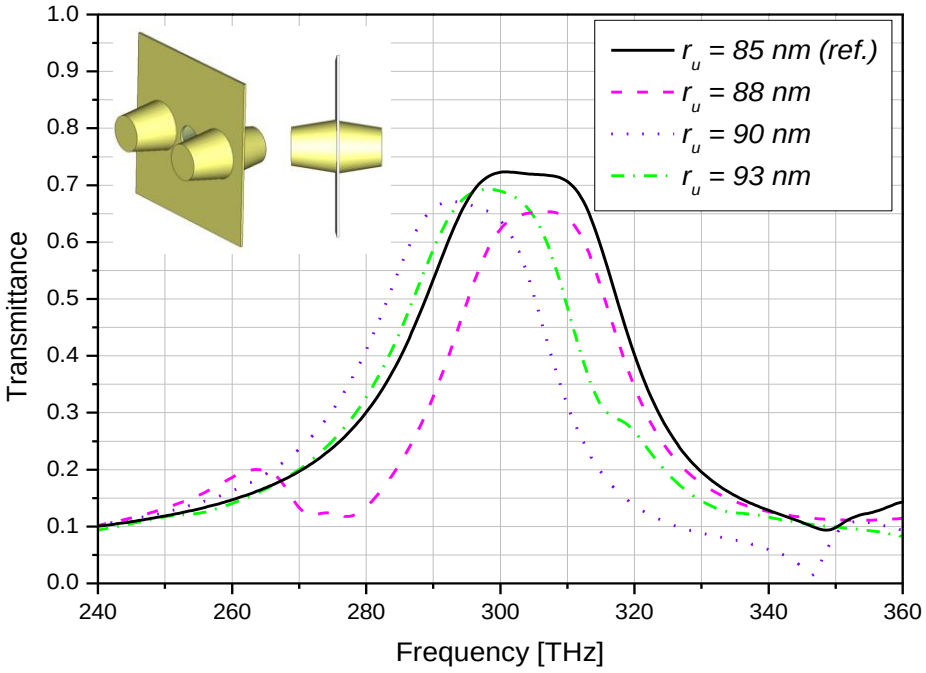

Figure 56 Transmittance for TM illumination of a 700 nm x 700 nm silver screen with two pillar pairs placed symmetrically on both entrance and exit faces. The solid line refers to the case with the same geometrical dimensions of the pillars as in the previous setups. The dashed and dotted lines, instead, present the variation of the transmittance by changing the radius of the upper base of the pillars (the case $r_u = 90\ nm$ corresponds to cylindrical pillars). (Pictures from ref. 4)

3.7.2 Silver nano-spheres rings

One of the major drawback of the setup presented in Section 3.7.1 is that its size is limited by the pillar pair dimensions, whose resonant frequency is achieved when the pair overall size is about λ/2. In order to further reduce the size of the resonator, we suggest, here, the use of a different structure, recently proposed to achieve optical magnetism at Near InfraRed (NIR) and visible frequencies, consisting of a ring of silver nano-particles [86].

The nano-ring magnetic resonator has the fundamental advantage that the magnetic resonance frequency is mainly related to the properties of the single plasmonic nano-

particle, rather than to the ring size, implying that the inclusion can be made, in principle, extremely small through a proper choice of the materials. In addition, as clearly shown in [86], the electromagnetic response of a plasmonic nano-ring can be assumed as due to a purely magnetic dipole, under the assumption that the ring is small compared to the operating wavelength and the number of nano-particles (e.g. spheres) is sufficiently large. Following the formulation in [86], the magnetic polarizability of a nano-ring made of six silver spheres (Figure 57 A) can be evaluated as:

$$\begin{cases} \alpha_{mm} = A / B \\ A = 432\, a^3 k_b^2\, \pi R^5 \left(\varepsilon_{sph} - \varepsilon_b\right) \\ B = a^3 \left(261 + 20\sqrt{3} + j72 k_b^5 R^5\right)\left(\varepsilon_{sph} - \varepsilon_b\right) - 72 R^3 \left(\varepsilon_{sph} + 2\varepsilon_b\right) \end{cases} \qquad (3.37)$$

Let's consider now a circular sub-wavelength aperture with radius $r_{ap} \ll \lambda$. The equivalent magnetic dipole moment describing the response of the aperture is given by [52]:

$$M_{eq} = -\frac{2}{3\pi} r_a^3 H_0 \qquad (3.38)$$

being H_0 the amplitude of the magnetic field at the aperture. In order to increase the transmission, we need to increase the amplitude of equivalent magnetic dipole of the aperture. If the nano-ring is placed across the aperture as shown in Figure 57 B, being $M_{eq} \ll M_{ring} = \alpha_{mm} H_0$, a quick estimation of the power transmission enhancement (PTE) may be given by:

$$PTE \propto \left|\frac{M_{ring}}{M_{ap}}\right|^2 = 419904\, \pi^4 R^{10} \left(a / r_h\right)^6 \left| k_b^2 \left(\varepsilon_{sph} - \varepsilon_b\right)\right|^2 / \left|B\right|^2 \qquad (3.39)$$

This formula can be used, thus, to implement the initial design of the nano-ring, in order to get the enhanced transmission at a given frequency. Frequency dependence is hidden in the permittivity ε_{sph} of the plasmonic spheres, which, in our case, has been modeled through the experiment-based Drude model in [82,19] $\varepsilon_{sph} = \varepsilon_\infty - \omega_p^2 / (\omega^2 - j\nu_c \omega)$ where $\nu_c = 9$ *THz*, $\omega_p = 2\pi \cdot 2 \cdot 10^{15}$ *rad/sec* and $\varepsilon_\infty = 4.7$.

When going towards the practical implementation of the nano-ring, sphere dimensions and

ring radius should be compatible with the available fabrication techniques. Therefore, though the overall nano-ring can be still made electrically small, its dimensions are not dramatically sub-wavelength anymore and, thus, expressions (3.37) and (3.39) are less accurate. Nevertheless, they represent a good starting point for the design of the nano-ring, whose dimensions need to be eventually optimized through proper full-wave numerical simulations.

Just to give an example of the typical dimensions of the nano-ring using geometrical parameters compatible with current fabrication capabilities, a nano-ring characterized by *6* spheres with radius $a = 60\ nm$ and $R = 130\ nm$ resonates at around *425 THz*, being its overall dimension $0.18\,\lambda$.

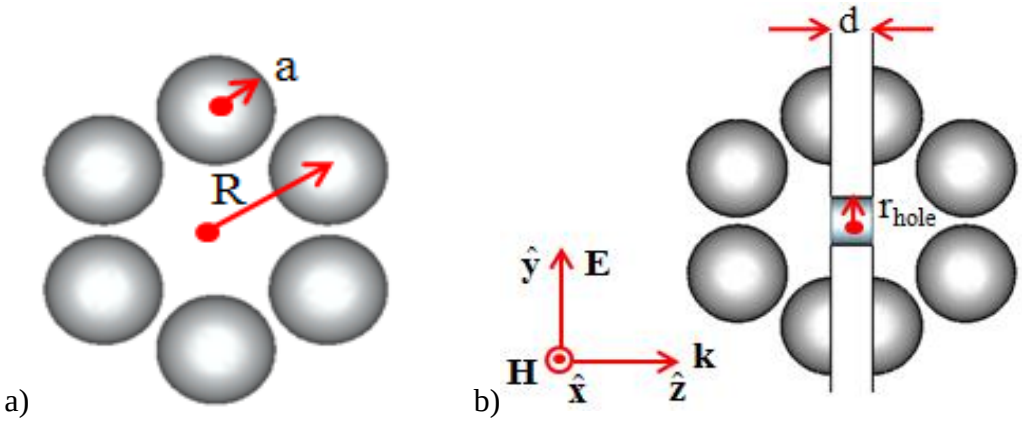

Figure 57 a) Nano-ring made of plasmonic spheres. b) Nano-ring placed across the aperture drilled in a metallic screen. (Pictures from ref. 87)

The nano-ring designed and optimized in the previous is now placed across the aperture ($r_{ap} = 30\ nm$) drilled in a silver screen ($d=50\ nm$). The electromagnetic response of the proposed structure has been tested through full-wave simulations. Transmission has been evaluated by placing the nano-ring in a bounded environment, characterized by two opposite perfect electric (PEC) and two opposite perfect magnetic (PMC) boundaries. Such a close waveguide supports a TEM mode with respect to the axis of propagation and the ring has been aligned with its axis directed along the magnetic field. The transmission enhancement has been evaluated through the scattering parameters of the waveguide,

whose dimensions are *0.7 μm* x *0.7 μm* x *1.4 μm*. The transmittance comparison between the cases of the circular aperture in the silver screen with and without the ring is reported in Figure 58.

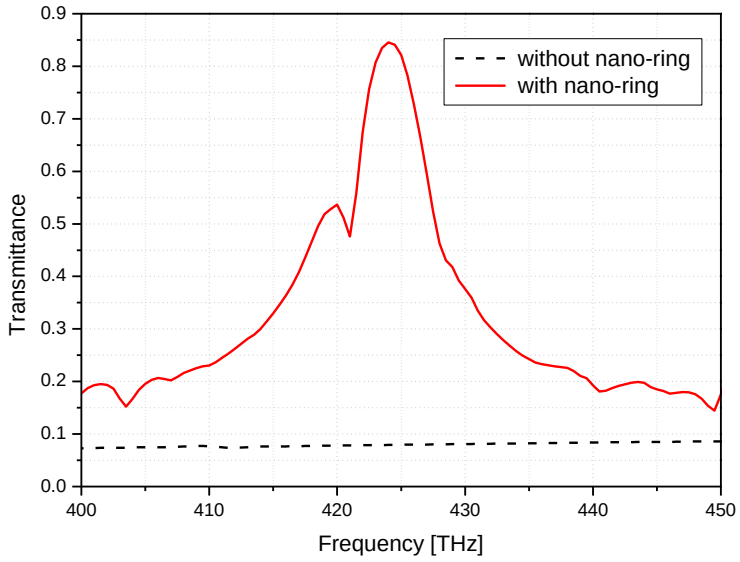

Figure 58 Transmittance of the setup reported in Fig. 1b. (Pictures from ref. 87)

As previously discussed, transmission enhancement is due to the strong magnetic resonance excited at the aperture by the nano-ring. In Figure 59, the current density distribution at the frequency of *425 THz* is shown, confirming the excitation of the magnetic resonance.

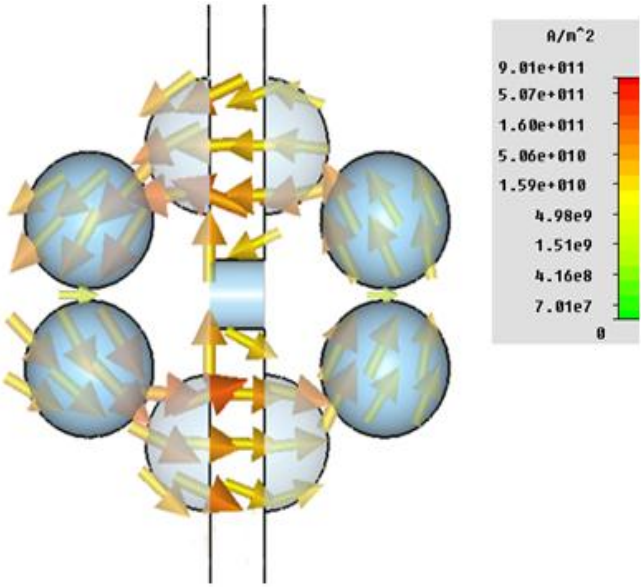

Figure 59 Current density distribution at the resonant frequency *f=425 THz*. (Pictures from ref. 87)

In Figure 60, the tangential magnetic field amplitude at the center of the aperture is shown, which is responsible for the transmission enhancement. Basically, the two half-rings work as receiving and transmitting resonant antennas, respectively, and the resonating nature of this system, allows transferring power from one side to the other of the aperture. We remark here that the simulation of the proposed setup is not a straightforward matter. In order to get a figure for the power transmission, in fact, the simulation is to be conducted in a bounded environment. On the other hand, we also have to ensure that the artificial boundary conditions adopted do not produce artifacts in the transmission response. For this reason, we have compared different simulation setups with different excitation sources (see Figure 60), confirming that the obtained resonance is effectively due to the nano-ring placed across the aperture.

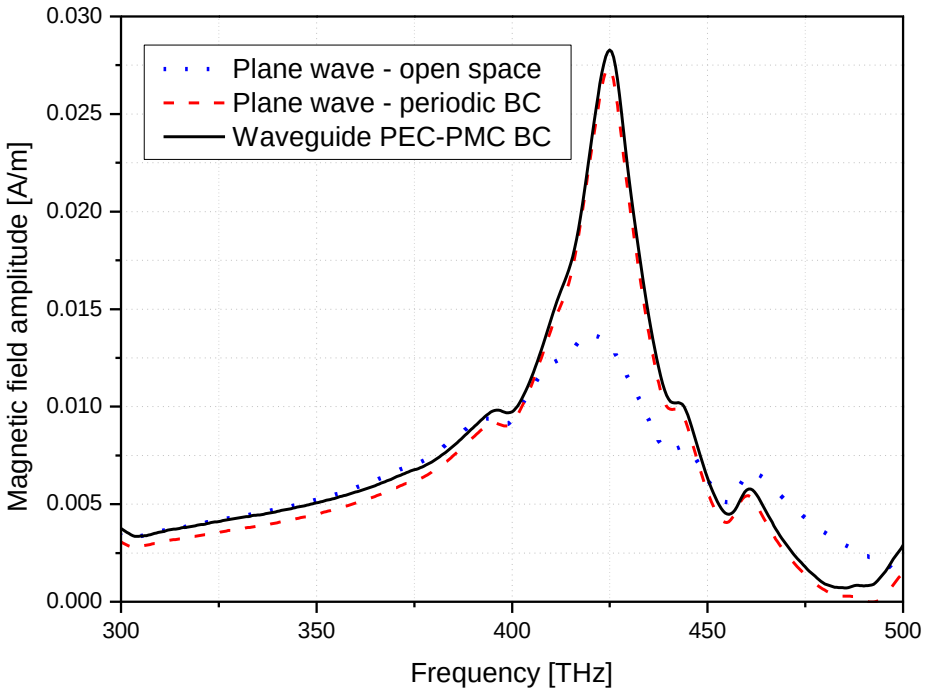

Figure 60 Tangential magnetic field amplitude at the circular aperture centre for different simulation setups with different boundary conditions (BC). (Pictures from ref. 87)

Waveguide port with PEC-PMC boundary conditions gives the same result as plane-wave excitation with periodic boundary conditions. The simulation of the $0.7\ \mu m$ x $0.7\ \mu m$ silver screen with a plane-wave excitation in an open space returns the same magnetic resonance frequency, confirming that the enhanced transmission is not due to the artificial boundary conditions introduced, but only to the resonating nano-ring.

The robustness of the proposed setup with respect to the variation of the incidence angle is reported in Figure 61, where the structure has been simulated in an open space rather than in a waveguide.

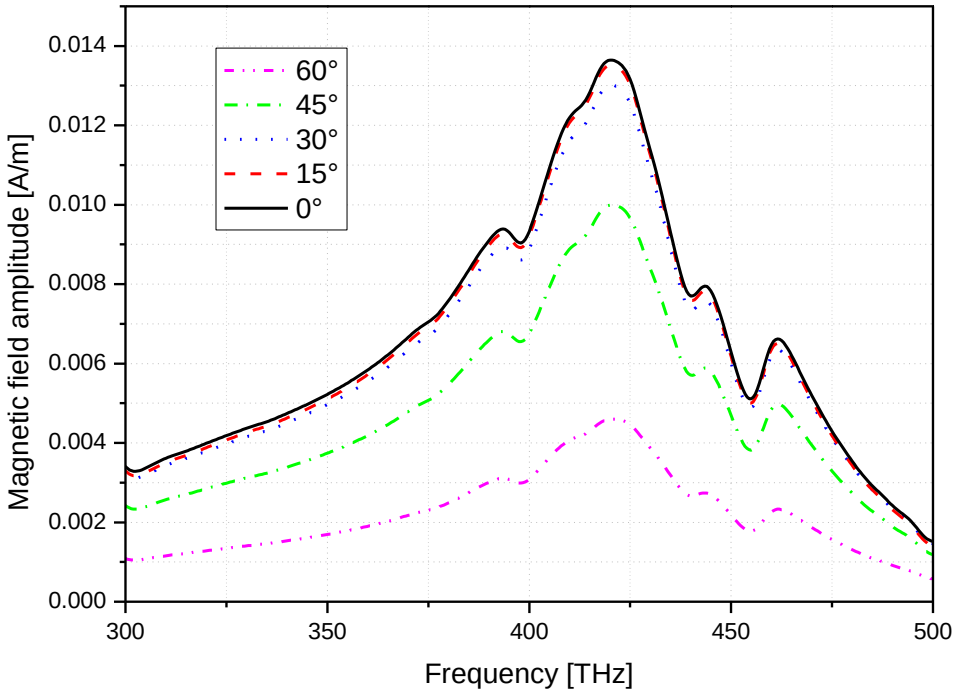

Figure 61 Magnetic field amplitude for different angles of incidence (TE polarization, with the magnetic field parallel to the screen). (Pictures from ref. 87)

Finally, the tunability of this structure has been investigated by considering the nano-ring embedded in a glass slab containing liquid crystals (relative permittivity ranging from 1.1 to 1.3). The corresponding transmission performances, are reported in Figure 62.

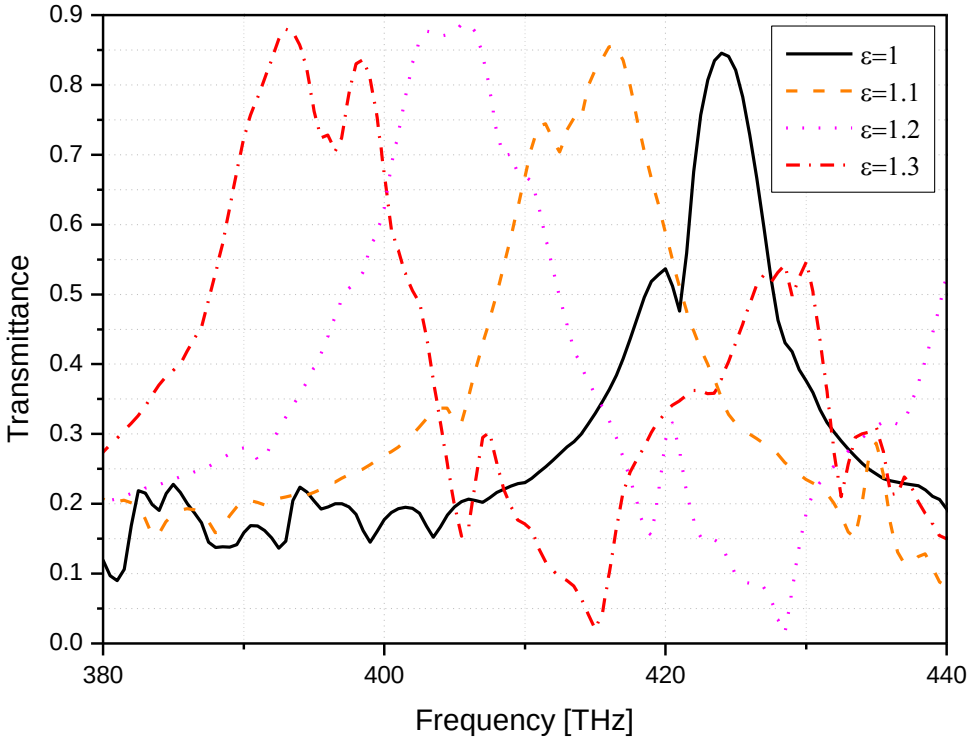

Figure 62 Transmittance spectra for different values of the permittivity of the slab where the nano-ring is embedded. (Pictures from ref. 87)

4. CONCLUSIONS

Despite of the promising initial results that the research in the field of metamaterials has already produced, from a technological point of view we are still a long way from successfully applying such theories to real-life devices able to compete, in terms of costs and efforts, with industrial standard devices.

Two special fields of interest that seem to be particularly promising in that sense are those of transmission line metamaterials at microwaves and of plasmonic epsilon-near zero metamaterials at THz scale. The first exhibits the advantage of very low fabrication costs and relatively large operating bandwidth. The latter simplifies the design of volumetric metamaterials taking advantage of the intrinsic dispersive properties of noble metals at THz frequencies.

The devices that have been here proposed are coherent with the aforementioned considerations. The details of the design of real-life structures have been presented. In the visible regime, gold and silver have been successfully applied to define the layout of resonant particles whose smallest details are compliant with the actual fabrication processes. At microwaves, alignments of inclusions of the same type and single isolated inclusions have been used to reduce the issues related to both interface phenomena and homogenization procedures. A theoretical background has been given for all the aforementioned structures in order to provide a better understanding of the physics behind the working principles of the proposed devices.

BIBLIOGRAPHY

1. V.G. Veselago, "The electrodynamics of substances with simultaneously negative values of epsilon and mu," Sov. Phys. Uspekhi, Vol. 10, No. 4, pp. 509-514, 1968

2. J.B. Pendry, A.J. Holden, W.J. Stewart, I. Youngs, "Extremely Low Frequency Plasmons in Metallic Meso Structures," Phys. Rev. Lett., Vol. 76, pp 4773-4776, 1996

3. J.B. Pendry, A.J. Holden, D.J. Robbins, and W.J. Stewart, "Low Frequency Plasmons in Thin Wire Structures," J. Phys. [Condensed Matter], Vol. 10, pp 4785-4809, 1998

4. J.B. Pendry, A.J. Holden, D.J. Robbins, and W.J. Stewart, "Magnetism from conductors and enhanced nonlinear phenomena," IEEE Trans. Microwave Theory Tech., Vol. 47, pp. 2075-2084, 1999

5. D.R. Smith, W.J. Padilla, D.C. Vier, S.C. Nemat-Nasser, S.Schultz, "Composite medium with simultaneously negative permeability and permittivity," Phys. Rev. Lett. 84, pp. 4184-4187, 2000

6. R.A. Shelby, D.R. Smith, S. Schultz, "Experimental verification of a negative index of refraction," Science 292, pp.77-79, 2001

7. J.B. Pendry, "Negative refraction makes a perfect lens," Phys. Rev, Lett. 85, pp. 3966 - 3969, 2000

8. J. D. Jackson Classical Electrodynamics, J. Wiley & Sons, 1975

9. J. Brown, "Artificial dielectrics having refractive indices less than unity," Proc. IEE 100, pt. 4: Monograph No. 62R, 51–62, 1953

10. R.E. Collin, Field Theory of Guided Waves, Oxford University Press, Oxford, 1991

11. W. Rotman, "Plasma simulation by artificial dielectrics and parallel plate media," Trans. IRE AP 10 82–95, 1962

12. G.H.B. Thompson, "Unusual waveguide characteristics associated with the apparent negative permeability obtainable in ferrites," Nature 175 1165–1166, 1955

13. G.H.B. Thompson, “Backward waves in longitudinally magnetized ferrite filled guides,” in: A.L. Cullen, V.A. Fock, J.R. Wait (Eds.),International Series of Monographs on Electromagnetic Waves, vol. 6, in: E.C. Jordan (Ed.), Electromagnetic Theory and Antennas, Pergamon Press, 1963, Proc. Symp. Copenhagen Denmark,1962

14. R. Marques, J. Martel, F. Mesa, F. Medina, “Left-handed-media simulation and transmission of EM waves in sub-wavelength splitring resonator loaded metallic waveguides,” Phys. Rev. Lett. 89 183901, pp.1-4, 2002

15. Filiberto Bilotti, Alessandro Toscano, and Lucio Vegni, “Design of Spiral and Multiple Split-Ring Resonators for the Realization of Miniaturized Metamaterial Samples,” IEEE Transactions on Antennas and Propagation, Vol. 55, pp. 2258-2267, 2006

16. A. Sihvola, “Self-consistency aspects of dielectric mixing theories, IEEE Transactions on Geoscience and Remote Sensing,” Vol. 27, pp. 403-415, 1989

17. C.R. Simovski, P.A. Belov “On homogenization of electromagnetic crystals formed by uniaxial resonant scatterers”, Phys. Rev. E 72 026615-1-15, 2005

18. C.R. Simovski and S.A. Tretyakov, “Local constitutive parameters of metamaterials”, Phys. Rev. B 75, 195111, 2007

19. Edward D. Palik, Handbook of Optical Constants of Solids, Academic Press, 1998

20. L. Lewin, “The electrical constants of a material loaded with spherical particles,” Proc. IEE 94 (1947) 65–68.

21. C.L. Holloway, E.F. Kuester, J. Baker-Jarvis, P. Kabos, “A double negative (DNG) composite medium composed of magnetodielectric spherical particles embedded in a matrix,” IEEE Trans. AP 51 (2003) 2596–2603.

22. Andrea Alù, Nader Engheta, “Polarizabilities and effective parameters for collections of spherical nanoparticles formed by pairs of concentric double-negative, single-negative, and/or double-positive metamaterial layers,” J. Appl. Phys. 97, 094310, 2005

23. G.V. Eleftheriades, A.K. Iyer, P.C. Kremer, “Planar negative refractive index media using periodically L-C loaded transmission lines, IEEE Trans. MTT 50, pp. 2702–2712, 2002

24. A. Grbic, G.V. Eleftheriades, “Dispersion analysis of a micro-stripbased negative refractive index periodic structure,” IEEE Microw. Wireless Comp. Lett. 13, pp. 155–157, 2003

25. C. Caloz, T. Itoh, “Transmission line approach of left-handed (LH) materials and microstrip implementation of an artificial LH transmission line,” IEEE Trans. AP 52, pp. 1159–1166, 2004

26. A. Lai, C. Caloz, T. Itoh, “Composite right/left-handed transmission line metamaterials,” IEEE Microw. Mag. 5, pp. 34–50, 2004

27. E. Engheta, A. Salandrino, A. Alu, “Circuit elements at optical frequencies: nanoinductors, nanocapacitors, and nanoresistors,” Phys. Rev. Lett. 95, 095504-1-3, 2005

28. C. Caloz and T. Itoh, Electromagnetic Metamaterials: Transmission Line Theory and Microwave Applications. New York: Wiley, 2004

29. C. Caloz, A. Sanada and T. Itoh, “A novel composite right/left-handed coupled-line directional coupler with arbitrary couple level and broad bandwidth,” IEEE Trans. Microwave Tech., Vol. 52, pp. 1142-1149, 2004

30. A. Sanada, C. Caloz and T. Itoh, “Zeroth order resonance in composite right/left handed transmission line resonators,” in Proc. Asia-Pacific Microwave Conf., Seoul, Korea, Vol. 3, pp 1588-1592, 2003

31. A. Sanada, M. Kimura, I. Awai, H. Kubo, C. Caloz and T. Itoh, “A planar zeroth order resonator antenna using left handed transmission line,” in Proc. European Microwave Conf., Amsterdam, Netherlands, 2004

32. T. Itoh et al., “Zeroth-order Resonator,” United States Patent No. US 7,330,090 B2, February 12, 2008

33. J. Bonache, M. Gil, I. Gil, J. Garcia-Garcia and F. Martin, “Limitations and Solutions of Resonant-Type Metamaterial Transmission Lines for Filter Applications: the Hybrid Approach,” IEEE MTT-S Int. Microwave Symp. Digest, pp. 939 - 942, 11-16, 2006

34. M. Gil, J. Bonache, J. García-García, J. Martel, and F. Martín, “Composite Right/Left-Handed Metamaterial Transmission Lines Based on Complementary Split-Rings Resonators and Their Applications to Very Wideband and Compact Filter Design,” IEEE Trans. Microwave Theory Tech., Vol. 55, No. 6, 2007

35. A. Lai, Kevin M.K.H. Leong, and Tatsuo Itoh, “Leaky-Wave Steering in a Two-Dimensional Metamaterial Structure Using Wave Interaction Excitation,” IEEE MTT-S Int. Microwave Symp. Digest, pp 1643-1646, 2006

36. A. Alu, M. G. Silveirinha, A. Salandrino, and N. Engheta, “Epsilon-Near-Zero Metamaterials and Electromagnetic Sources: Tailoring the Radiation Phase Pattern,” Physical Review B, Vol. 75, 155410, 2007

37. D.F. Sievenpiper, “High-Impedance Electromagnetic Surfaces,” Ph.D. Dissertation, University of California at Los Angeles, 1999

38. P.J. Ferrer, J.M. González-Arbesú, J. Romeu, A. Cardama, “Bidirectional artificial magnetic reflectors at microwave frequencies,” Microwave and Optical Technology Letters, Volume 49 Issue 8, pp. 1949-1953, 2007.

39. F. Bilotti, L. Nucci, L. Vegni, “An SRR based microwave absorber,” Microwave and Optical Technology Letters, Vol. 48 Issue 11, pp. 2171-2175.

40. R. L. Fante e M. T. McCormack – “Reflection properties of the Salisbury Screen”, IEEE Transactions on Antennas e Propagation, Vol. 36, No. 10, 1443-1454, 1988

41. L. Scorrano, S. Tricarico, F. Bilotti, L. Vegni, "Design of Optical Nano-Antenna Reflectors through Dielectric Structures with Extreme-valued Constitutive Parameters," on Proc. 3rd EOS Topical Meeting on Optical Microsystems (OMS09), September 27-30, 2009, Capri, Italy

42. A. Alù and N. Engheta, “Input Impedance, Nanocircuit Loading, and Radiation Tuning of Optical Nanoantennas,” Phys. Rev. Lett. 1001, 043901, 2008.

43. A. Alù and N. Engheta, “Hertzian plasmonic nanodimer as an efficient optical nanoantenna,” Phys. Rev. B 78, 195111, 2008.

44. S.M. Rytov, “Electromagnetic properties of a finely stratified medium,” Sov. Phys. JETP, Vol 2., pp. 466–475, 1955.

45. D. Bergman, “The dielectric constant of a composite material - a problem in classical physics,” Phys. Rep., Phys. Lett. 43, 377, 1978.

46. L. Scorrano, F. Bilotti, L. Vegni, “Near Field Pattern Synthesis at Optical Frequencies,” on Proc. National workshop on Metamaterials and Special Materials for Electromagnetic Applications and TLC (MMSM'08) , Naples, Italy, 2008

47. L. Scorrano, F. Bilotti, and L. Vegni, “Design of a Meta-Screen for Near-Zone Field Focalization at Optical Frequencies,” Microwave and Optical Technology Letters, Vol. 51, No. 11, pp. 2718-2721, 2009

48. R. Merlin, “Radiationless electromagnetic interference: evanescent-field lenses and perfect focusing,” Science No. 317, pp. 927-929, 2007

49. W.-K. A. Grbic, L. Jiang, and R. Merlin, “Near field plates: Subdiffrac- tion focusing with patterned surfaces,” Science No. 320, pp. 511-513, 2008

50. R. G. Mote, S. F. Yu, B. K. Ng, W. Zhou, and S. P. Lau, Near-field focusing properties of zone plates in visible regime - New insights, Opt. Expr. 16 (2008), 9554-9564.

51. A. Salandrino, A. Alù, and N. Engheta, Parallel, series, and intermediate interconnections of optical nanocircuit elements. 1. Analytical solution, J. Opt. Soc. Am. B 24, 3007-3013,2007

52. H. A. Bethe, “Theory of diffraction by small holes,” Physical Review, vol. 66, No. 7 and 8, pp. 163-182, 1944

53. A.A. Oliner and D.R. Jackson, “Leaky surface-plasmon theory for dramatically enhanced transmission through a subwavelength aperture, part I: basic features,” in Proc. IEEE AP-S Symp. & URSI Meeting, Columbus, OH, 2003

54. T. Zhao, D.R. Jackson, J.T. Williams, and A.A. Oliner, “Leaky-wave theory for enhanced transmission through subwavelength apertures, part II: leaky-wave antenna model,” in Proc. IEEE AP-S Symp. & URSI Meeting, Columbus, OH, 2003

55. D.E. Grupp, H.J. Lezec, T. Thio, and T.W. Ebbsen, “Beyond the Bethe limit: tunable enhanced light transmission through a single sub-wavelength aperture,” Advanced Materials, vol. 11, no. 10, pp. 860–862, 1999

56. A. Alù, F. Bilotti, N. Engheta, and L. Vegni, “Metamaterial Covers Over a Small Aperture,” IEEE Trans. Antennas Propagat., Vol. AP-54, No. 6, pp.1632-1643, 2006

57. A. Alù, F. Bilotti, N. Engheta, L. Vegni, “Sub-Wavelength Planar Leaky-Wave Components with Metamaterial Bilayers,” IEEE Trans. Antennas Propagat., Vol. AP-55, No. 3, pp. 882-891, 2007

58. A. Alù, F. Bilotti, N. Engheta, L. Vegni, “A review on the potential use of metamaterial layers for increasing the transmission through a single sub-wavelength aperture in a flat opaque

screen," Chapter 10 (pp. 271-291) in Periodic Structures, edited by M. Bozzi and L. Perregrini, Kerala, India, 2006

59. A. Alù, and N. Engheta, "Pairing an epsilon-negative slab with a mu-negative slab: anomalous tunneling and transparency," IEEE Trans. Antennas Propagat., Vol. AP-51, No. 10, pp. 2558-2570, 2003

60. F. Bilotti, "Application of metamaterials for miniaturized components," Metamaterials for Industry, Short Course for Industries and SMEs, Jouy-en-Josas, France, 28-30, 2005

61. N. Engheta, "An idea for thin, subwavelength cavity resonators using metamaterials with negative permittivity and permeability," IEEE Antennas Wireless Propagat. Lett., Vol. AWPL-1, pp. 10-13, 2002.

62. A. Alù, F. Bilotti, N. Engheta, and L. Vegni, "Sub-wavelength, compact, resonant patch antennas loaded with metamaterials," IEEE Trans. Antennas Propagat., Vol. AP-55, pp. 13-25, Jan. 2007.

63. R.W. Ziolkowski, and A.D. Kipple, "Application of double negative materials to increase the power radiated by electrically small antennas", IEEE Trans. Antennas Propagat., Vol. AP-51, No. 10, pp. 2626- 2640, Oct. 2003.

64. K. Aydin et al., A. O. Cakmak, L. Sahin, Z. Li, f. Bilotti, L. Vegni, and e. Ozbay, "Split-Ring-Resonator-Coupled Enahanced Transmission through a Single Subwavelegth Aperture"Phys. Rev. Lett. Vol. 102, 013904, 2009

65. F. Bilotti, L. Scorrano, E. Ozbay, L. Vegni, "Enhanced Transmission Through a Sub-Wavelength Aperture: Resonant Approaches Employing Metamaterials," Journal of Optics A: Pure and Applied Optics, vol. 11, pp. 114029-1-8, 2009

66. D. Ates, A. O. Cakmak, e. Colak, R. Zhao, C. M. Soukoulis, and E. Ozbay, "Transmisssion Enhancement through deep Subwavelength apertures using connected splitring resonators," Opt. Expr. Vol. 18, No. 4, 3952, 2010

67. Simovski C.R., Belov P.A., Kondratiev M.S., Tretyakov S.A., "Diffraction by a planar array of omega particles," Proceedings of Bianisotropics'97, University of Glasgow, UK, pp. 293-296, 1997.

68. Simovski C.R., Tretyakov S.A., Sochava A.A., Sauviac B., Mariotte F., Kharina T.G., "Antenna model for conductive omega particles," J. Electromagnetic Waves Applic., vol. 11, no. 11, pp. 1509-1530, 1997.

69. B. Munk, Frequency Selective Surfaces: Theory and Design. New York: Wiley, 2000

70. A. Alù, N. Engheta, "Evanescent Growth and Tunneling Through Stacks of Frequency-Selective Surfaces," IEEE Antennas and Wireless Propagation Letters, vol. 4, pp. 417-420, 2005

71. L. Scorrano, F. Bilotti, E. Ozbay e L. Vegni, "Strutture risonanti per la trasmissione straordinaria da aperture elettricamente piccole", RinEM 2010, Benevento, Italia, 2010

72. A.A. Oliner, "Equivalent Circuits for Small Symmetrical Longitudinal Apertures and Obstacles," IRE Trans. on Microwave Theory and Techniques, Vol. 8, pp. 72-80, 1960

73. W.H. Eggimann, "Higher-Order Evaluation of Dipole Moments of a Small Circular Disk," IRE Trans. Microwave Theory and Techniques, Vol. 8, Issue 5, pp. 573 – 573, 1960

74. R. E. Collin and W. H. Eggimann, "Evaluation of dynamic interaction fields in a two dimensional lattice," IEEE Trans. on Microwave theory and Techniques, Vol. 9, pp. 110-115, 1961

75. W. H. Eggimann and R. E. Collin,"Electromagnetic Diffraction by a Planar Array of Circular Disks," IRE Trans. Microwave Theory and Techniques, Vol. 8, Issue 5, pp. 528 – 535, 1962

76. L. Scorrano, F. Bilotti, E. Ozbay, and L. Vegni, FSS Covers for Power Transmission Enhancement through Electrically Small Apertures, Journal of Applied Physics A, (in press), 2010

77. S. Tretyakov, "On geometrical scaling of split-ring and double-bar resonators at optical frequencies," Metamaterials, 1, pp. 40-43, 2007

78. J. Zhou, Th. Koschny, M. Kafesaki, E. N. Economou, J. B. Pendry, C.M. Soukoulis, Saturation of magnetic response of split-ring resonators at optical frequencies, Phys. Rev. Lett. 95, 223902, 2005

79. G. Dolling et al., "Cut-wire pairs and plate pairs as magnetic atoms for optical metamaterials," Opt. Lett. 30, 3198-3200, 2005

80. M. Kafesaki et al., "Left-handed metamaterials: the fishnet structure and its variations," Phys. Rev. B 75, 235114, 2007

81. A.N. Grigorenko et al., “Nanofabricated media with negative permeability at visible frequencies,” Nature 438, 335-338, 2005

82. D.R. Lide, Handbook of Chemistry and Physics, CRC Press 2003

83. L. Scorrano, S. Tricarico, F. Bilotti, "Resonating plasmonic particles to achieve power transmission enhancement," IEEE Photonics Technology Letters, Vol. 22, 12, pp. 938-940, 2010

84. Q. Zhao et al., “Electrically tunable negative permeability metamaterials based on nematic liquid crystals,” Appl. Phys. Lett. 90, 011112, 2007

85. A.N. Grigorenko, A.K. Geim, H.F. Gleeson, Y. Zhang, A.A. Firsov, I. Y. Khrushchev, J. Petrovic, “Nanofabricated media with negative permeability at visible frequencies,” Nature 438, pp. 335-338, 2005.

86. A. Alù and N. Engheta, “Dynamical theory of artificial optical magnetism produced by rings of plasmonic nanoparticles,” Phys. Rev. B 78, 085112, 2008.

87. L. Scorrano, F. Bilotti, L. Vegni, "Achieving Power Transmission Enhancement by Using Nano-Rings Made of Silver Spheres," IEEE Photonics Technology Letters, Vol. 22, 21, pp. 1595-1597, 2010

PUBLICATIONS

On International Conference Proceedings

1. F. Bilotti, L. Scorrano, L. Vegni, "Enhanced Power Transmission through a Sub-Wavelength Aperture by Employing Single Negative Metamaterial Covers," on Proc. ISMOT 2007 Villa Mondragone Monte Porzio Catone, Italy, 2007

2. F. Bilotti, L. Scorrano, L. Vegni, "The Role of Ideal and Inclusion-made Single Negative Metamaterials to Achieve the Extraordinary Transmission Through a Sub-wavelength Hole," on Proc. ICECom 2007 19th International Conference on Applied Electromagnetics and Communications, Dubrovnik, Croatia, 2007

3. F. Bilotti, L. Scorrano, L. Vegni, "Transmission enhancement from a sub-wavelength hole in a perfect electric screen through the employment of new setups based on SNG metamaterials," on Proc. IEEE Antennas and Propagation International Symposium, Honolulu, HI, 2007

4. F. Bilotti, L. Scorrano, L. Vegni, "Enhanced transmission from a sub-wavelength aperture through the employment of SNG metamaterials," on Proc. 2nd Young Scientist Meeting on Metamaterials (YSMM'08), Barcelona Spain, 2008

5. L. Scorrano, F. Bilotti, L. Vegni, "Near Field Pattern Synthesis at Optical Frequencies," on Proc. National workshop on Metamaterials and Special Materials for Electromagnetic Applications and TLC (MMSM'08) , Naples, Italy, 2008

6. F. Bilotti, L. Scorrano, L. Vegni, "Enhanced transmission through a sub-wavelength aperture using single negative metamaterials," on Proc. Nanometa 2009, Seefeld Tirol, Austria, 2009

7. L. Scorrano, F. Bilotti, L. Vegni, "Design of a TLM phase-compensated printed monopole antenna," on Proc. SPIE Europe Optics and Optoelectronics, Prague, Czech Republic, 2009

8. L. Scorrano, F. Bilotti, L. Vegni, "Design of complex surfaces for power transmission enhancement through electrically small apertures," on Proc. International Conference on Electromagnetics in Advanced Applications - ICEAA 2009, Torino, Italy, 2009

9. L. Scorrano, F. Bilotti, L. Vegni, “On the role of conjugate pairs of FSS in overcoming the diffraction limit at microwaves, on Proc. 4th EOS Topical Meeting on Advanced Imaging Techniques - EOS 2009, Jena, Germany, 2009

10. L. Scorrano, F. Bilotti, L. Vegni, “FSS Approach for Power Transmission Enhancement through Electrically Small Apertures,” on Proc. 8th International Symposium on Electric and Magnetic Fields - EMF 2009, Mondovì, Italy, 2009

11. L. Scorrano, F. Bilotti, L. Vegni, “Engineered-Response Surfaces for Power Transmission Enhancement through Electrically Small Apertures,” on Proc. Metamaterials 2009, London, UK, 2009

12. F. Bilotti, L. Scorrano, E. Ozbay, L. Vegni, “Enhanced transmission through sub-wavelength apertures: metamaterial-based approaches at microwave and optical frequencies,” on Proc. 2nd Mediterranean Conference on Nanophotonics, Athens, Greece, 2009

13. L. Scorrano, S. Tricarico, F. Bilotti, L. Vegni, “Design of Optical Nano-Antenna Reflectors through Dielectric Structures with Extreme-valued Constitutive Parameters,” on Proc. 3rd EOS Topical Meeting on Optical Microsystems (OMS09), September 27-30, 2009, Capri, Italy

14. F. Bilotti, L. Scorrano, E. Ozbay, and L. Vegni, “Extraordinary microwave transmission through sub-wavelength apertures by employing metamaterials and metasurfaces”, 2nd International Conference on Metamaterials, Photonic crystals and Plasmonics (META'10), Cairo, Egitto, 2010

15. L. Scorrano, F. Bilotti, E. Ozbay e L. Vegni, “Strutture risonanti per la trasmissione straordinaria da aperture elettricamente piccole”, RinEM 2010, Benevento, Italia, 2010

16. F. Bilotti, L. Scorrano, E. Ozbay, and L. Vegni, “Resonant Artificial Structures to Achieve Extraordinary Transmission at Microwaves”, European Microwave Conference, Paris, France, 2010

17. L. Scorrano, F. Bilotti, E. Ozbay, and L. Vegni, “Design of a Transmission-Line-Metamaterials-Inspired Miniaturized Printed Monopole”, The 14th WSEAS International Conference on COMMUNICATIONS (part of the 14th WSEAS CSCC Multiconference), Corfu Island, Greece, July 23-25, 2010

18. L. Scorrano, F. Bilotti, E. Ozbay, and L. Vegni, “Tunnelling, impedance matching and power transmission enhancement trough electrically small apertures via omega inclusions,”

Proceedings of the Fourth International Congress on Advanced Electromagnetic Materials in Microwaves and Optics – Metamaterials 2010, Karlsruhe, Germany, 2010

19. F. Bilotti, S. Tricarico, L. Scorrano, and L. Vegni, "Enhancement of NSOM tip performances through the employment of metamaterials," Proceedings of the Fourth International Congress on Advanced Electromagnetic Materials in Microwaves and Optics – Metamaterials 2010, Karlsruhe, Germany, 2010

20. L. Scorrano, F. Bilotti, L. Vegni, "Resonant Sub-Wavelength Devices to Achieve Enhanced Transmission through Electrically Small Apertures", 20th International Conference on Applied Electromagnetics and Communications (Icecom 2010), Dubrovnik, Croatia, 2010

21. L. Scorrano, S. Tricarico, F. Bilotti, and L. Vegni, "Tunneling and radiating phenomena related to coupled omega particles", European Conference on Antennas and Propagation 2011, 11-15, 2011

On International Journals

1. L. Scorrano, F. Bilotti, and L. Vegni, "Design of a Meta-Screen for Near-Zone Field Focalization at Optical Frequencies," Microwave and Optical Technology Letters, Vol. 51, No. 11, pp. 2718-2721, 2009

2. F. Bilotti, L. Scorrano, E. Ozbay, L. Vegni, "Enhanced Transmission Through a Sub-Wavelength Aperture: Resonant Approaches Employing Metamaterials," Journal of Optics A: Pure and Applied Optics, vol. 11, pp. 114029-1--8, 2009

3. L. Scorrano, F. Bilotti, E. Ozbay, and L. Vegni, FSS Covers for Power Transmission Enhancement through Electrically Small Apertures, Journal of Applied Physics A, (*in press*), 2010

4. L. Scorrano, S. Tricarico, F. Bilotti, "Resonating plasmonic particles to achieve power transmission enhancement," IEEE Photonics Technology Letters, Vol. 22, 12, pp. 938-940, 2010

5. L. Scorrano, F. Bilotti, L. Vegni, "Achieving Power Transmission Enhancement by Using Nano-Rings Made of Silver Spheres," IEEE Photonics Technology Letters, Vol. 22, 21, pp. 1595-1597, 2010

NOTES

The commercial software CST Microwave Studio 2009 has been used to perform numeral full-wave simulations, while the commercial software Wolfram Mathematica 6.0 has been used to manipulate analytical expressions.